Inertial Confinement Fusion Reactor Cavity Analysis: Progress Report for the Period 1 July 1987 to 30 June 1988

R.R. Peterson, J.J. MacFarlane, J.J. Barry, F. Gonzalez, M. El-Afify, G.A. Moses, M.L. Corradini

July 1988

UWFDM-765

FUSION TECHNOLOGY INSTITUTE

UNIVERSITY OF WISCONSIN

MADISON WISCONSIN

Inertial Confinement Fusion Reactor Cavity Analysis: Progress Report for the Period 1 July 1987 to 30 June 1988

R.R. Peterson, J.J. MacFarlane, J.J. Barry, F. Gonzalez, M. El-Afify, G.A. Moses, M.L. Corradini

Fusion Technology Institute
University of Wisconsin
1500 Engineering Drive
Madison, WI 53706

http://fti.neep.wisc.edu

July 1988

UWFDM-765

INERTIAL CONFINEMENT FUSION REACTOR CAVITY ANALYSIS

Progress Report for the Period 1 July 1987 to 30 June 1988

R.R. Peterson, J.J. MacFarlane, J.J. Barry,
F. Gonzalez, M. El-Afify, G.A. Moses and M.L. Corradini

July 1988

Fusion Technology Institute
University of Wisconsin
1500 Johnson Drive
Madison, WI 53706-1687

UWFDM-765

TABLE OF CONTENTS

TABLE OF CONTENTS

1. INTRODUCTION

We have studied target chamber issues for the past year as part of a long term effort in conjuction with personnel at the Lawrence Livermore National Laboratory (LLNL). We have built upon our previous work with LLNL [1] which 1) studied the accuracy of the CONRAD and MIXERG computer codes by comparison with experimental and computational results and 2) designed an experiment to study condensation physics in ICF target chambers. The logical extension of that effort was to modify our computer codes to improve their accuracy and to proceed with construction of a condensation experiment. Additionally, with the increased interest in a Laboratory Microfusion Facility (LMF), we have used our improved codes to study target chamber issues in LLNL concepts for an LMF. In addition to the code modifications we have revised the documentation for these codes, CONRAD and MIXERG (now called IONMIX) and have transported these codes to LLNL. Our effort during the period July 1, 1987 to June 30, 1988 can be broken down into four parts: 1) experimental studies of the condensation of vaporized material, 2) development of computer models to simulate the behavior of target chamber gases and vapors, 3) modification of these computer codes to allow the use of equation-of-state and opacity data from a variety of sources, and 4) use of these computer codes to study the target chamber concepts under development at LLNL. The specific statement-of-work is shown in Table 1.1.

This report is broken up into four technical sections, for each of the four major areas of research. In Section 2, we discuss calculation of the equation-of-state and radiative properties in ICF target chamber gases. The issue of local thermodynamic equilibrium in the gases is discussed as is the improved computer code, IONMIX. In Section 3, we discuss improvements to the CONRAD computer code for simulating the behavior of the target chamber gases

Table 1.1. Statement of Work for the Period 7/1/87 - 6/30/88

1. CONRAD computer code development:
   a. Improve ion deposition in CONRAD.
   b. Expand the Lagrangian mesh in CONRAD to include the outer material and change the rezoning method to conform with new meshing scheme.
   c. Update CONRAD documentation.
2. Format SESAME and MIXERG data in a common way so a user has the choice of using either package in CONRAD.
3. Physics of Rapid Vaporization:
   a. Use the improved CONRAD to simulate details of wall ablation and the shocks and other reactions of the wall to the ablation.
4. Fabricate and test capacitive discharge system and experimental chamber of condensation experiment.
5. Write a final report.

Table 1.2. Publications

1. R.R. Peterson, "Target Chamber Gas Issues in Near Term ICF Facilities," to be published in the Proceedings of the Symposium on Laser Interaction and Related Plasma Phenomena, October 1987, Monterey, CA.

2. J.J. MacFarlane, "IONMIX - A Code for Computing the Equation-of-State and Radiative Properties of LTE and Non-LTE Plasmas," University of Wisconsin Fusion Technology Institute Report UWFDM-750 (December 1987), submitted to Computer Physics Communications.

3. J.J. MacFarlane, G.A. Moses, and R.R. Peterson, "Non-LTE Effects in Inertial Confinement Fusion Target Chambers," University of Wisconsin Fusion Technology Institute Report UWFDM-761 (April 1988), submitted to Nuclear Fusion.

4. J.J. MacFarlane, G.A. Moses, and R.R. Peterson, "Energy Deposition and Shock Wave Evolution from Laser-Generated Plasma Expansions," University of Wisconsin Fusion Technology Institute Report UWFDM-723 (revised September 1987), submitted to Physics of Fluids.

and vapors. Section 4 is devoted to a description of our work on the condensation experiment. Much of this work has been in construction of the experiment and the diagnostics. Finally, in Section 5 we present results of LMF relevant simulations with the improved computer code. We summarize our progress and discuss future directions in Section 6. During the last year we have published some of our results, as listed in Table 1.2.

In addition to the work described in this report, the PhD thesis work of Muhammed El-Afify has proceeded during this period. This work will be completed during the summer of 1988 and his thesis will be published at that time. His work is related to the simulation of condensation physics in the experiment at the University of Wisconsin and in Inertial Confinement Fusion (ICF) target chambers. He has used a Monte-Carlo particle transport method that is independent of the methods used in CONRAD, and thus gives us an additional comparison to test CONRAD's validity. He has proposed new formulas for the condensation rates for both pure vapors and vapors mixed with non-condensable gases that we plan to introduce into the CONRAD code.

Reference for Section 1

1. R.R. Peterson, J.J. MacFarlane, G.A. Moses, M. El-Afify and M.L. Corradini, "Inertial Confinement Fusion Reactor Cavity Analysis: Progress Report for the Period 1 July 1986 to 30 June 1987," University of Wisconsin Fusion Technology Report UWFDM-725 (July 1987).

2. EQUATION OF STATE DATA FOR CONRAD

CONRAD now has the option of using one of several equation of state packages: MIXERG, SESAME, and IONMIX. In the past, the MIXERG [1] code has been used to supply equation of state and multifrequency opacity data for CONRAD. We have found several deficiencies with some of the physics models in the code, especially those for low density, non-LTE plasmas (LTE ≡ local thermodynamic equilibrium). Because of this, we have given the CONRAD user the option of selecting different equation of state packages. The SESAME data files at Los Alamos [2] have been used for a number of years as a source of equation of state and opacity data for target implosion codes. These data tables are often applicable for dense plasmas where interparticle potentials are important. However, non-LTE processes are ignored, and the SESAME tables are inappropriate for many target chamber applications. Even so, some CONRAD users may prefer using the SESAME data, especially for problems involving high plasma densities. CONRAD now gives the user this option.

Target chamber plasmas often migrate between the LTE and non-LTE regimes. In the non-LTE regime, which is characterized by low densities and high temperatures, the 2-body (radiative and dielectronic) recombination rates exceed the 3-body (collisional) recombination rates. To provide CONRAD with reliable data over the large range of plasma conditions relevant to ICF target chamber studies, we have written a new computer code, IONMIX [3], which provides equation of state and multifrequency opacity data for both LTE and non-LTE plasmas. The results from this code compare favorably with SESAME data at high densities and non-LTE results from other codes at low densities (see Sec. 2.2.4). We feel that target chamber simulations that use the plasma properties supplied by IONMIX provide the most reliable results to date.

In this section, we first briefly describe how to access the SESAME equation of state data files with CONRAD. Then, we discuss in some detail the physical models in IONMIX and some applications.

2.1. Accessing the SESAME Data Files with CONRAD

The SESAME equation of state and opacity data files can be accessed directly by CONRAD. To use the SESAME data in a CONRAD simulation, the user must do the following:

1) Copy the SESAME data files from the MASS storage system into the user's local file area;
2) Set the variable ISW(27) = 2 in the namelist input file (CNRDIN);
3) Set the interpolation option switch ISW(28) to 0 (bi-linear; default), 1 (bi-quadratic), or 2 (bi-rational function).

During its initialization process, CONRAD stores the SESAME data into arrays of 10 densities by 20 temperatures for later use in the simulation. MIXERG and IONMIX results can also be written to data files using the SESAME formatting style. The above procedure should also be used for accessing data of this type.

2.2. Overview and Applications of the IONMIX Computer Code

2.2.1. Introduction

We have developed a new computer code, IONMIX, to calculate equations of state and multigroup opacities of LTE and non-LTE plasmas [3]. The need for doing this arose because of several deficiencies in the MIXERG code [4], and we knew of no other code that computes the physical properties of plasmas over the entire range of conditions needed for ICF target chamber studies. The SESAME package, for example, does not include models for non-LTE processes,

and its data is therefore unreliable at densities $\lesssim 10^{17}$ cm^{-3} when temperatures are $\gtrsim$ 1 eV.

IONMIX provides more accurate results than MIXERG for the following reasons:

1) IONMIX uses no artificial transition between the Saha (LTE) and "coronal" (non-LTE) regimes; all reactions for all ionization states are considered in computing the ionization populations.
2) IONMIX includes dielectronic recombination and radiative deexcitation in the rate equations as well as collisional ionization and recombination, radiative recombination, and collisional excitation and deexcitation.
3) Bound-bound transitions contribute to absorption and emission far from the line centers in IONMIX; this can be important if the photoionization and bremsstrahlung contributions are very small.
4) IONMIX includes contributions from transitions in which the principal quantum number does not change; this can sometimes dominate the radiative properties.
5) More ionization stages can contribute to absorption and emission in IONMIX.
6) Line widths include collisional broadening as well as natural and Doppler broadening effects in IONMIX.
7) In IONMIX, array sizes are easily adjusted to allow for a wider range of problems; e.g., higher Z elements, mixtures with many elements, etc.

The results from IONMIX compare well with other published results for equations of state and opacity over a wide range of plasma conditions.

2.2.2. Background for Target Chamber Plasmas

In previous calculations for ICF target chambers [5,6], the radiative properties of the background plasma were calculated under the assumption of local thermodynamic equilibrium (LTE). For the LTE assumption to be valid, the plasma density must be sufficiently high that all atomic processes -- ionization, recombination, excitation, and deexcitation -- are collisionally dominated [7]. However, this assumption is not always valid for conditions that occur in ICF chambers. In fact, it is rarely true when the background gas (room temperature) pressure is $\lesssim$ 1 torr because the radiative deexcitation and recombination rates exceed the collisional rates. At somewhat higher gas pressures, ~ 10 - 100 torr, the plasma can migrate between the collisionally dominated, LTE regime and the radiatively dominated, non-LTE regime as it heats up and later cools. Therefore, both collisional and radiative processes must be simultaneously considered in calculating the radiative properties of ICF target chamber plasmas.

Below, we discuss the conditions for which the assumption of local thermodynamic equilibrium breaks down, and illustrate how using the more appropriate non-LTE plasma radiative properties affects the radiative and hydrodynamic transport of energy away from the target. The plasma properties are computed by considering both radiative and collisional processes in calculating the ionization and excitation populations, as well as the absorption and emission coefficients. The details of calculating the plasma properties are discussed in Section 2.2.3. In Section 2.2.4, we compare our calculations using IONMIX with other published results.

In Section 2.2.5, we present results of radiation-hydrodynamic calculations for typical ICF high yield target chamber environments using the plasma properties calculated by IONMIX. Here, we will primarily examine the

radiative flux and shock-produced impulse at the chamber wall, and show how the more general non-LTE plasma results differ from those of LTE plasmas. And finally, we will review the conclusions concerning non-LTE effects in Section 2.2.6.

2.2.3. Plasma Properties Computed Using IONMIX

The steady-state ionization and excitation populations of the background plasma are calculated using detailed balancing arguments [8]. The fraction of ions in each ionization state is determined by equating the number of collisional ionizations with the sum of collisional, radiative, and dielectronic recombinations. Similarly, the excitation populations are calculated by balancing the number of collisional excitations with the total number of collisional and radiative deexcitations. Radiative contributions to excitation and ionization can be ignored because the radiation energy density in ICF target chambers is small.

The fraction of ions in the j^{th} ionization state, f_j, of a given species is determined from the coupled set of rate equations:

$$\left(\frac{df_j}{dt}\right) = n_e \{f_{j-1} C_{j-1}^{coll} - f_j(C_j^{coll} + \alpha_j^{tot}) + f_{j+1}\alpha_{j+1}^{tot}\} \quad j=1,Z \ , \quad (2.1)$$

where Z is the atomic number, n_e is the electron density, C_j^{coll} is the collisional ionization rate from state j to j+1, and α_{j+1}^{tot} is the sum of the collisional, radiative, and dielectronic recombination rates from state j+1 to j. In the steady-state approximation, $(df_j/dt) = 0$ and the ionization populations are determined by:

$$f_j = \left(\prod_{m=0}^{j-1} R_{m,m+1}\right) / \left(1 + \sum_{l=1}^{z} \prod_{m=0}^{l-1} R_{m,m+1}\right) \qquad (2.2)$$

where

$$R_{m,m+1} = \frac{C_m^{coll}}{\alpha_{m+1}^{coll} + \alpha_{m+1}^{rad} + \alpha_{m+1}^{diel}} .$$

The collisional ionization and recombination coefficients for the transition between ionization states j and j+1 can be written as [9]:

$$C_j^{coll} = (1.09\times10^{-6}\,cm^3s^{-1})T^{1/2} \cdot e^{-\chi_j}(1 - e^{-\chi_j})\Phi_j^{-2}\Gamma_j \qquad (2.3)$$

and

$$\alpha_{j+1}^{coll} = C_j^{coll} \cdot (1.66\times10^{-22})n_e T^{-3/2} \cdot e^{\chi_j}(U_{j+1}/U_j) \qquad (2.4)$$

where T is the electron temperature in eV, Φ_j is the ionization potential in eV, $\chi_j \equiv \Phi_j/T$, Γ_j is the Gaunt factor, and U_j and U_{j+1} are the electronic partition functions for the j^{th} and $(j+1)^{st}$ ionization stages.

For the radiative recombination coefficient, we use the formula derived by Seaton [10]:

$$\alpha_{j+1}^{rad} = (5.20\times10^{-14}\,cm^3s^{-1})(j+1)\chi_j^{3/2} \cdot e^{\chi_j}E_1(\chi_j) \qquad (2.5)$$

where $E_1(\chi_j)$ is the first exponential integral [13], and a Gaunt factor of unity is assumed.

At relatively high temperatures, dielectronic recombination is often the dominant recombination process. For this, we use the modifications of Post

et al. [9] to the formulae originally proposed by Burgess [11]:

$$\alpha_{j+1}^{diel} = (2.40\times10^{-9}\,cm^3s^{-1})T^{-3/2}B(j)D(j) \cdot \sum_n f_{ni}A(y)e^{-\bar{E}_{ni}(j)/T} \qquad (2.6)$$

where i is the initial electronic state of the ion, and the summation is over all bound states n. f_{ni} is the oscillator strength for the exciting transition. The expressions for B(j) and E(j) are

$$B(z \equiv j+1) = z^{1/2}(z+1)^{5/2}(z^2+13.4)^{-1/2}$$

$$\bar{E}_{ni}(z) = 13.6\ eV(z+1)^2(\nu_i^{-2} - \nu_n^{-2})/a$$

where

$$a = 1 + 0.015(j+1)^3/(j+2)^2\ ,$$

and ν_i and ν_n are the effective principal quantum numbers of state i and n, respectively. The formulae for A(y) and D(j) depend on whether a change in the principal quantum number occurs during the excitation. They are defined as

$$A(y) = \begin{cases} y^{1/2}/(1 + 0.105y + 0.015y^2), & \Delta n = 0 \\ y^{1/2}/(2 + 0.420y + 0.060y^2), & \Delta n \neq 0 \end{cases}$$

$$D(q \equiv j+2) = \begin{cases} N_t/(N_t + 200), & \Delta n = 0 \\ (qN_t)^2/[(qN_t)^2 + 667], & \Delta n \neq 0 \end{cases}$$

where

$$y = (j+2)/(\nu_i^{-2} - \nu_n^{-2})$$

and

$$N_t = [1.51 \times 10^{17} (j+1)^6 T^{1/2}/n_e]^{1/7} .$$

D(q) represents a reduction factor to account for increased collisional effects at high densities.

Both the radiative and dielectronic recombination rates ($n_e n_{j+1} \alpha_{j+1}$) increase linearly with the electron density, while the collisional recombination rate increases as the square of the electron density. This is because collisional recombination is a 3-body process involving two electrons and an ion, whereas radiative and dielectronic recombination are considered to be 2-body reactions with the excess energy being carried off by a photon rather than a second electron. Thus, in the high density limit, $\alpha_{coll} >> \alpha_{rad} + \alpha_{diel}$, and the plasma is in local thermodynamic equilibrium.

The conditions under which a plasma will be in LTE can be determined by comparing the 3-body and 2-body recombination rates. Results for a nitrogen plasma are presented in Fig. 2.1. Here, the ratio of the collisional recombination rate to the sum of the radiative and dielectronic rates is plotted as a function of the ion density for three different electron temperatures: 1, 10, and 100 eV. For each temperature, the recombination rates were computed for the most abundant ionization state: $N^{1+} \rightarrow N^{0+}$ at 1 eV, $N^{4+} \rightarrow N^{3+}$ at 10 eV, and $N^{6+} \rightarrow N^{5+}$ at 100 eV. When $\alpha_{coll} >> \alpha_{rad} + \alpha_{diel}$ (above the dashed line) the plasma is in collisional equilibrium, and the ionization and excitation populations can be accurately computed using the well-known Saha equation and Boltzmann statistics [12]. However, this does not occur until the nitrogen

ion density is $\gtrsim 10^{18}$, 10^{19}, and 10^{21} cm^{-3} for temperatures of 1, 10, and 100 eV, respectively.

The densities in ICF target chambers are expected to range between 10^{12} and 10^{19} cm^{-3}, and temperatures from ~ 1 eV to 1 keV. In Fig. 2.1, this range of densities and temperatures is indicated by the shaded region. Hence, it is seen that the background plasma in ICF target chambers cannot be assumed to be in local thermodyanamic equilibrium, as 2-body recombination processes often dominate. On the other hand, it is seen that collisional recombination cannot always be neglected. Thus, both 2-body and 3-body processes must be considered simultaneously to adequately determine the populations and radiative properties of target chamber ICF plasmas.

The more general non-LTE plasma can have a significantly lower specific energy, pressure, and average charge state than one assumed to be in LTE. This is because the inclusion of 2-body processes will cause depopulation of the upper ionization and excitation levels. This is shown in Figs. 2.2 and 2.3 where the average charge state and specific energy for neon are plotted for three different temperatures as a function of density. The dashed curves in each figure are the results for a plasma assumed to be in LTE. The solid curves represent the more general case where both 2-body and 3-body processes are considered. Again, the transition from the collisionally dominated regime to the radiatively dominated regime shows a strong dependence on the plasma temperature. In Fig. 2.3, it is seen that the assumption of local thermodynamic equilibrium can lead to specific energies that are too large by as much as a factor of two.

It is interesting to consider the evolution of a fluid element as it is heated isochorically from ~ 1 eV to several hundred eV. For a nitrogen plasma with a density of ~ 10^{19} cm^{-3} (see Fig. 2.1), electronic recombination will

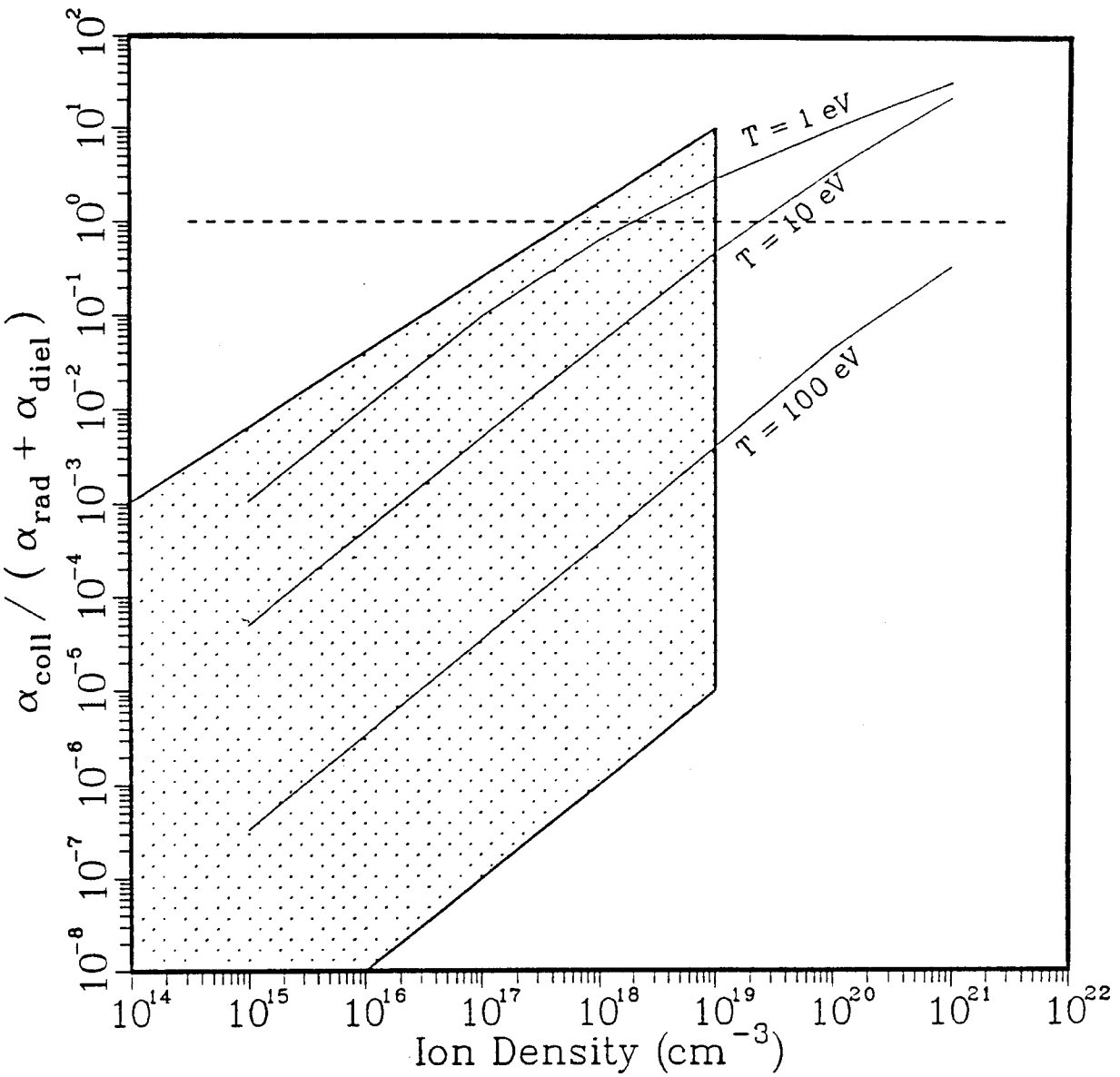

Figure 2.1. Ratio of collisional recombination rate to the sum of radiative and dielectronic recombination rates for a nitrogen plasma as a function of density. Results are for the $N^{1+} \rightarrow N^{0}$, $N^{4+} \rightarrow N^{3+}$, and $N^{6+} \rightarrow N^{5+}$ transitions for the 1, 10, and 100 eV curves, respectively. The shaded region represents the regime of densities and temperatures relevant to ICF target chambers.

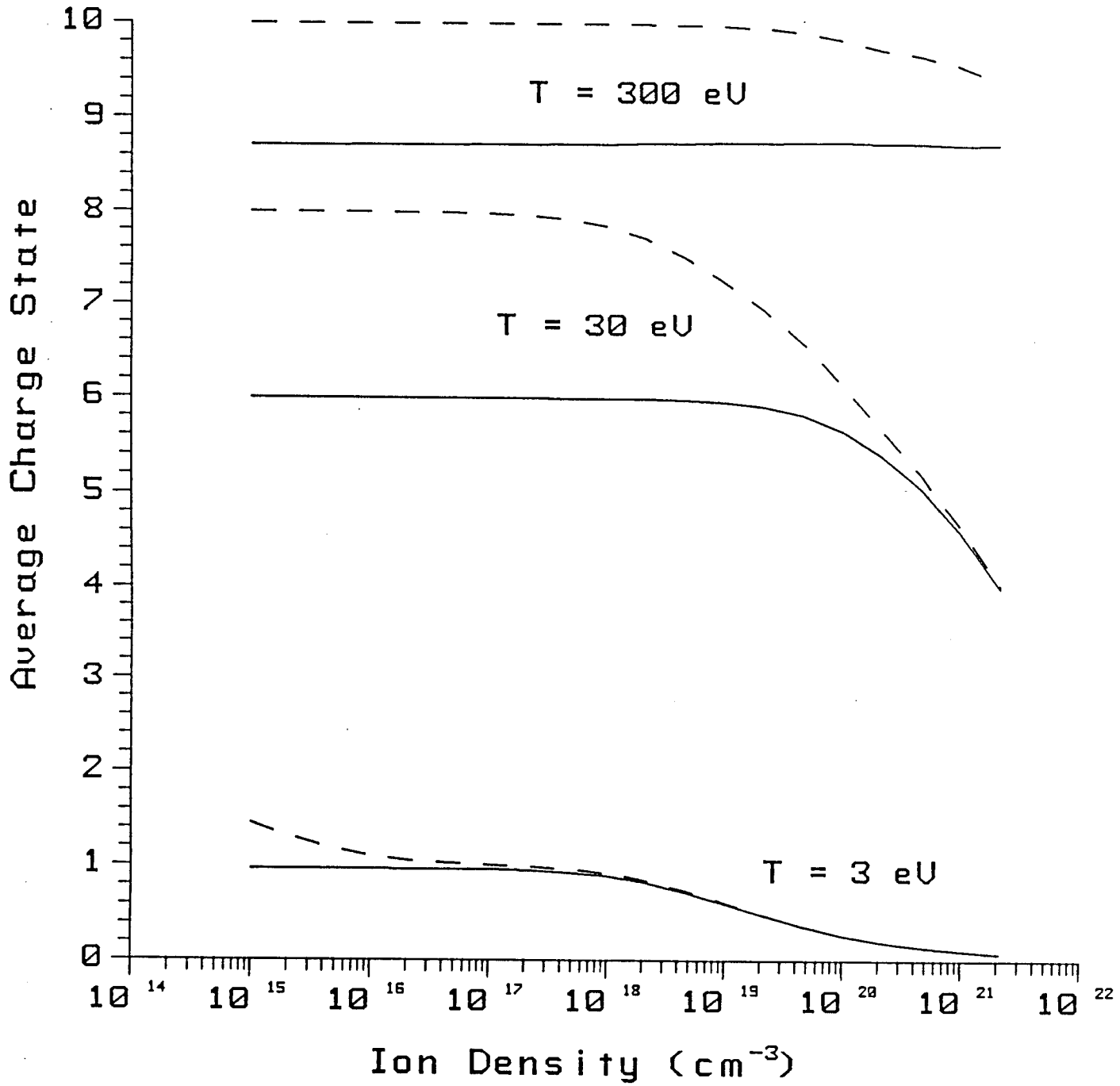

Figure 2.2. Average charge state vs. density for neon at temperatures of 3, 30, and 300 eV. Non-LTE processes were included in the calculation of the solid curve. The dashed curve represents results of an LTE plasma.

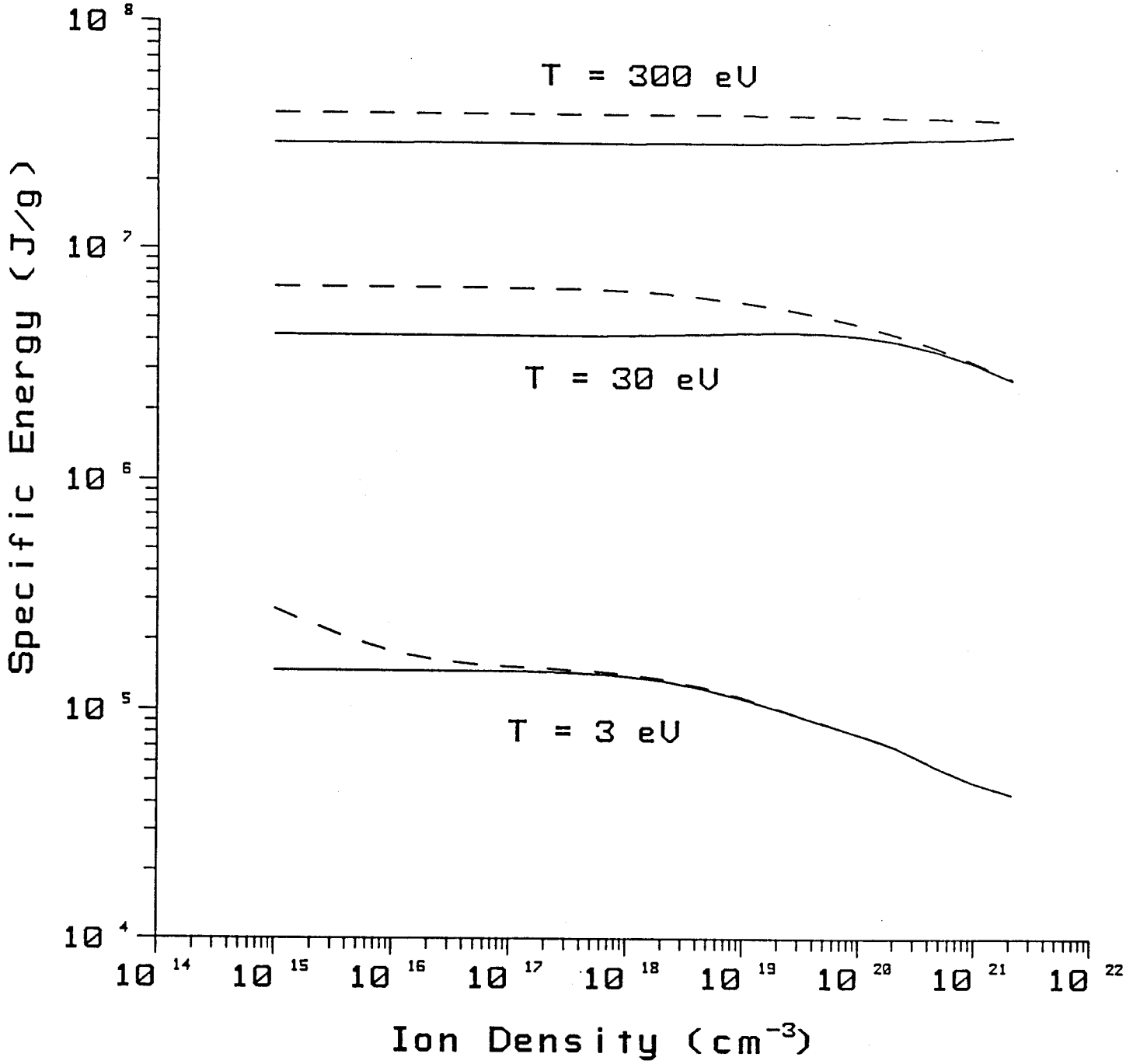

Figure 2.3. Specific energy vs. density for neon at temperatures of 3, 30, and 300 eV. Non-LTE processes were included in the calculation of the solid curve. The dashed curve represents results of an LTE plasma.

be collisionally dominated at temperatures ~ 1 eV. As the temperature of the fluid element increases, 2-body recombination becomes more important, and eventually dominates at temperatures $\gtrsim$ 10 eV. At these relatively high temperatures, the plasma is in the so-called "coronal equilibrium" state [7].

The influence of non-LTE processes becomes even more pronounced when calculating the plasma radiative properties. This can be seen by comparing the rates of emission and absorption of photons from a plasma. The general form for the absorption coefficient and emissivity for an ion can be written, respectively, as [7]:

$$\kappa_\nu = \sum_n \sum_{m>n} [N_n - (\frac{g_n}{g_m})N_m]\alpha_{nm}^{bb}(\nu)$$

$$+ \sum_{n>n'} [N_n - N_n^* e^{-h\nu/k_B T}]\alpha_n^{bf}(\nu) + n_e N_+ \alpha^{ff}(\nu)[1 - e^{-h\nu/k_B T}] \qquad (2.7)$$

and

$$\eta_\nu = (\frac{2h\nu^3}{c^2})\{\sum_n \sum_{m>n} (\frac{g_n}{g_m})N_m \alpha_{nm}^{bb}(\nu)$$

$$+ \sum_{n>n'} N_n^* e^{-h\nu/k_B T} \alpha_n^{bf}(\nu) + n_e N_+ \alpha^{ff}(\nu) e^{-h\nu/k_B T}\} \qquad (2.8)$$

where n' is determined by the photoionization cutoff energy, n_e is the electron density, and N_n^* is the equilibrium population of state n calculated using the actual number of ions in the next highest ionization state, N_+. The terms h, c, k_B, and ν as usual represent Planck's constant, the speed of light, Boltzmann's constant, and the photon frequency. The α's and g's represent the cross sections of the various transitions and the degeneracy factors, respectively.

The terms from left to right in Eqs. (2.7) and (2.8) represent the contributions from bound-bound, bound-free, and free-free transitions. The second term inside each of the square brackets in Eq. (2.7) is the contribution from stimulated emission to the absorption coefficient. Note that for high densities (i.e., LTE), $N_m = N_n(g_m/g_n)\, e^{-h\nu_{mn}/k_BT}$ and $N_n = N_n^*$. Thus, the correction for stimulated emission for all three transitions reduces to the LTE form $1 - \exp(-h\nu/k_BT)$, and the relation between the absorption coefficient and emissivity is given by the well-known Kirchoff-Planck relation, $\eta_\nu = \kappa_\nu B_\nu$ (where B_ν is the Planck function).

The cross section for free-free transitions in the hydrogenic approximation is [7]

$$\alpha^{ff}(\nu) = \frac{(2.40 \times 10^{-37}\,\mathrm{cm}^5) \cdot j^2\, \overline{g_{ff}}}{(h\nu)^3 T^{1/2}} \qquad (2.9)$$

where $h\nu$ is the photon energy in eV. For the free-free Gaunt factor, we use a simple fit to the results of Karzas and Latter [13]

$$\overline{g_{ff}} = 1 + 0.44 \exp\{-\tfrac{1}{4}(\gamma^2 + \tfrac{1}{4})^2\}$$

where

$$\gamma^2 \equiv \log_{10}(13.6 \cdot \overline{Z_k^2}/T)$$

and

$$\overline{Z_k^2} \equiv \sum_{j=1}^{Z_k} j^2 f_{jk}$$

is the mean of the square of the ion charge state. The bound-free cross section is [7]

$$\alpha_n^{bf} = \frac{(1.99 \times 10^{-14} cm^2) \cdot F_u (j+1)^4}{n^5 (h\nu)^3} \qquad (2.10)$$

where F_u is the unoccupied fraction of the shell with principal quantum number n.

The bound-bound cross-section is a function of the oscillator strength, f_{nm}, and the line shape function $L(\Gamma,\nu)$ [7]:

$$\alpha_{nm}^{bb} = (2.65 \times 10^{-2} cm^2 s) \cdot f_{nm} L(\Gamma,\Delta\nu) \; . \qquad (2.11)$$

IONMIX will compute the line shapes using either a Lorentzian profile or a Voight profile (default). The expression for the Lorentzian profile is

$$L_L(\Gamma,\Delta\nu) = \frac{\Gamma/4\pi^2}{(\Delta\nu)^2 + (\Gamma/4\pi)^2}$$

where $\Delta\nu$ is the photon frequency shift from the line center, and Γ is the damping factor due to natural, Doppler (thermal), and collisional broadening:

$$\begin{aligned} \Gamma &= \Gamma_{nat} + \Gamma_{Dop} + \Gamma_{coll} \\ &= (2.29 \times 10^6)(\Delta E_{nm})^2 \\ &\quad + (1.41 \times 10^{11}) \Delta E_{nm} \langle v \rangle + (4.58 \times 10^6) \langle v \rangle \, n_{tot}^{1/3} \; . \end{aligned}$$

$\langle v \rangle \equiv (T/A)^{1/2}$ is proportional to the mean thermal velocity, A is the atomic weight of the ion in amu, and ΔE_{nm} is the energy of the transition. The Voigt line profile is

$$L_V(\Gamma,\Delta\nu) = H(\Gamma,\Delta\nu,\Delta\nu_D)/(\pi^{1/2}\Delta\nu_D)$$

where $\Delta\nu_D$ is the Doppler shift, and $H(\Gamma,\Delta\nu/\Delta\nu_D)$ is the Voigt function, which depends on the freqency shift and the ratio of the Doppler damping factor to the sum of the natural plus collisional damping factors. The reader is referred to ref. [7] for a discussion of the Voigt function properties.

The scattering coefficient is used in calculating the radiative transport properties of the plasma. IONMIX considers contributions from Thomson electron scattering and plasma waves. We use the classical form of the Thomson cross section, which is reliable for low to moderate x-ray energies ($\lesssim 10^4$ eV) [7]:

$$s_\nu^T = (6.66 \times 10^{-25} cm^{-1}) n_e^{\ddagger} \tag{2.12}$$

where $n_e^{\ddagger}$ is the effective electron density in cm^{-3}, which includes contributions from each bound electron for which the photon energy is greater than its binding energy. Thomson scattering becomes a dominant contributor to the Rosseland opacity at relatively high temperatures and low densities.

The scattering of photons by plasma oscillations can occur at low photon energies and high electron densities ($\gtrsim 10^{19}$ cm^{-3}). The plasma wave scattering coefficient can be written as [1]

$$s_\nu^P = \begin{cases} (\omega_p^2 - \omega^2)^{1/2}/c , & \text{if } h\nu \le h\omega_p \\ 0 & \text{if } h\nu > h\omega_p \end{cases} \tag{2.13}$$

where

$$\omega_p = (4\pi e^2 \, n_e \, / \, m_e)^{1/2}$$

is the plasma frequency, e is the electron charge, and m_e is the electron mass.

The absorption and emission coefficients for a plasma of 90% Ar and 10% Li are plotted as a function of photon energy in Figs. 2.4 and 2.5, respectively. The temperature in the calculation is 5 eV and the density is 3×10^{17} cm^{-3}. The bound-bound transitions and photoionization edges are clearly visible in both figures. The peaks in the emission coefficients become smaller relative to absorption coefficients as the photon energy increases. This is because the populations move farther from LTE as the energy of the transition increases.

The Rosseland and Planck mean opacities are obtained by integrating the absorption, emission, and scattering coefficients over the photon energy. The Rosseland mean opacities are generally used in determining the transport characteristics of radiation through a medium, while the Planck mean opacities are used to calculate the rates of energy exchange between the plasma and radiation. IONMIX computes Planck and Rosseland mean group opacities for up to 50 photon energy bins. Planck mean opacities for aborption and emission are computed separately because local thermodynamic equilibrium cannot be assumed.

The Planck mean group opacities for absorption and emission in the photon energy range from $x_g \equiv h\nu_g/kT$ to $x_{g+1} \equiv h\nu_{g+1}/kT$ are defined by [7]

$$\sigma^A_{p,g} = \frac{1}{\rho} \frac{\int_{x_g}^{x_{g+1}} dx\, B_\nu(T_R)\kappa_\nu}{\int_{x_g}^{x_{g+1}} dx\, B_\nu(T_R)} \qquad (2.14)$$

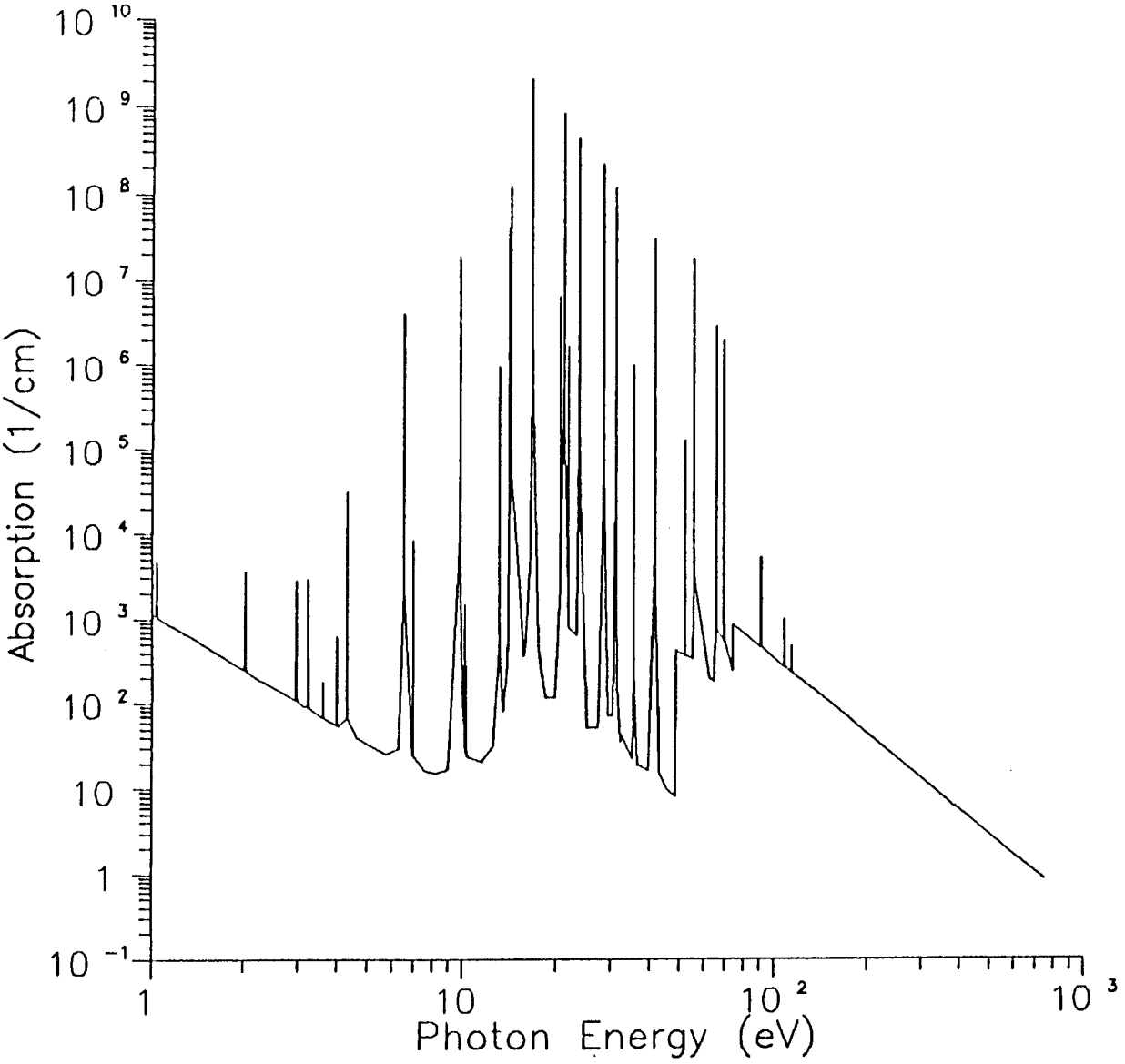

Figure 2.4. Absorption coefficient vs. photon energy for a plasma composed of 90% Ar and 10% Li at a temperature of 5 eV and a density of 3 x 10^{17} cm^{-3}.

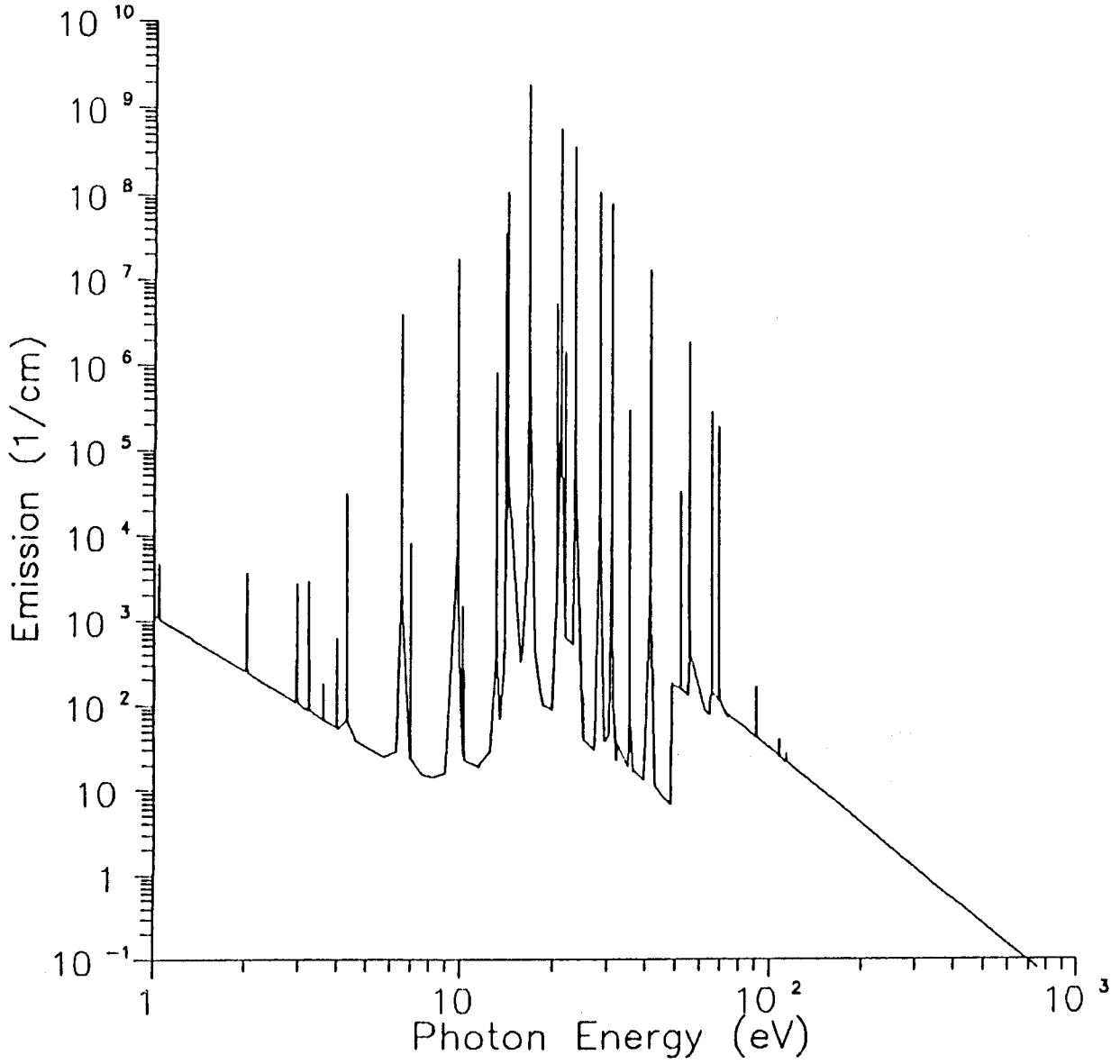

Figure 2.5. Emission coefficient vs. photon energy for a plasma composed of 90% Ar and 10% Li at a temperature of 5 eV and a density of 3 x 10^{17} cm^{-3}.

and

$$\sigma^{E}_{P,g} = \frac{1}{\rho} \frac{\int_{x_g}^{x_{g+1}} dx\ \eta_\nu}{\int_{x_g}^{x_{g+1}} dx\ B_\nu(T_R)} \tag{2.15}$$

where ρ is the mass density, and κ_ν and η_ν are defined in Eqs. (2.7) and (2.8). $B_\nu(T_R)$ is the Planck function characterized by the radiation temperature T_R. The Rosseland mean group opacity is determined from a weighted average of the inverse of the total extinction coeffient, $\kappa_\nu + s_\nu$. In this case, the radiative coefficients are weighted by the temperature derivative of the Planck function:

$$\sigma_{R,g} = \frac{1}{\rho} \frac{\int_{x_g}^{x_{g+1}} dx\ \left(\frac{\partial B_\nu}{\partial T_R}\right)}{\int_{x_g}^{x_{g+1}} dx \left(\frac{\partial B_\nu}{\partial T_R}\right) \frac{1}{\kappa_\nu + s_\nu}} . \tag{2.16}$$

As illustrated in Figs. 2.4 and 2.5, the absorption and emission coefficients are not smoothly varying functions of the photon energy. Thus, to evaluate the opacity integrals with the desired accuracy, κ_ν and η_ν must be evaluated at a number of strategically placed points. Examples of this include points on either side of each photoionization edge, and several points in the vicinity of each bound-bound transition energy.

The ratio of the average absorption to emission rate is determined by integrating Eqs. (2.7) and (2.8) over all frequencies to get the Planck means:

$$\sigma^{A}_{P} \,/\, \sigma^{E}_{P} = \left[\int_0^\infty d\nu\ \kappa_\nu B_\nu\right] \,/\, \left[\int_0^\infty d\nu\ \eta_\nu\right] . \tag{2.17}$$

This ratio is plotted in Fig. 2.6 for a neon plasma as a function of density for three temperatures. Again, at relatively low temperatures and high densities, the plasma is in LTE. But at temperatures $\gtrsim 10^2$ eV, plasmas at densities $\lesssim 10^{21}$ cm^{-3} are very far from LTE. Thus, at densities relevant to ICF target chambers, the non-LTE plasma emission rate can be several orders of magnitude lower than that calculated assuming LTE. And as we will show below, this lower emission rate for non-LTE plasmas can lead to a significantly lower radiation flux and stronger shock wave in the target chamber background plasma.

2.2.4. Comparison Between IONMIX Results and Other Calculations

Example 1

The first example illustrates results for a low density nitrogen plasma. The density is 10^{14} atoms/cm^3, and the temperature ranges from 1 eV to 100 keV. Under these conditions, the plasma is not in local thermodynamic equilibrium (LTE) as 2-body atomic processes are the dominant recombination mechanisms. Results for the specific energy, average charge state, and plasma cooling rate (per ion per free electron) are plotted in Figs. 2.7 through 2.9. These results are a very weak function of the density at ion densities $\lesssim 10^{16}$ cm^{-3}.

The dashed curves in Figs. 2.8 and 2.9 represent the results obtained by Post et al. [9].

Example 2

The second example shows the results for a high density SiO_2 plasma that is assumed to be in LTE. Results for the Rosseland mean group opacities between 10 and 1000 eV are shown in Fig. 2.10 for a temperature of 500 eV and mass density of 0.1 g/cm^3. The IONMIX results can be compared with those

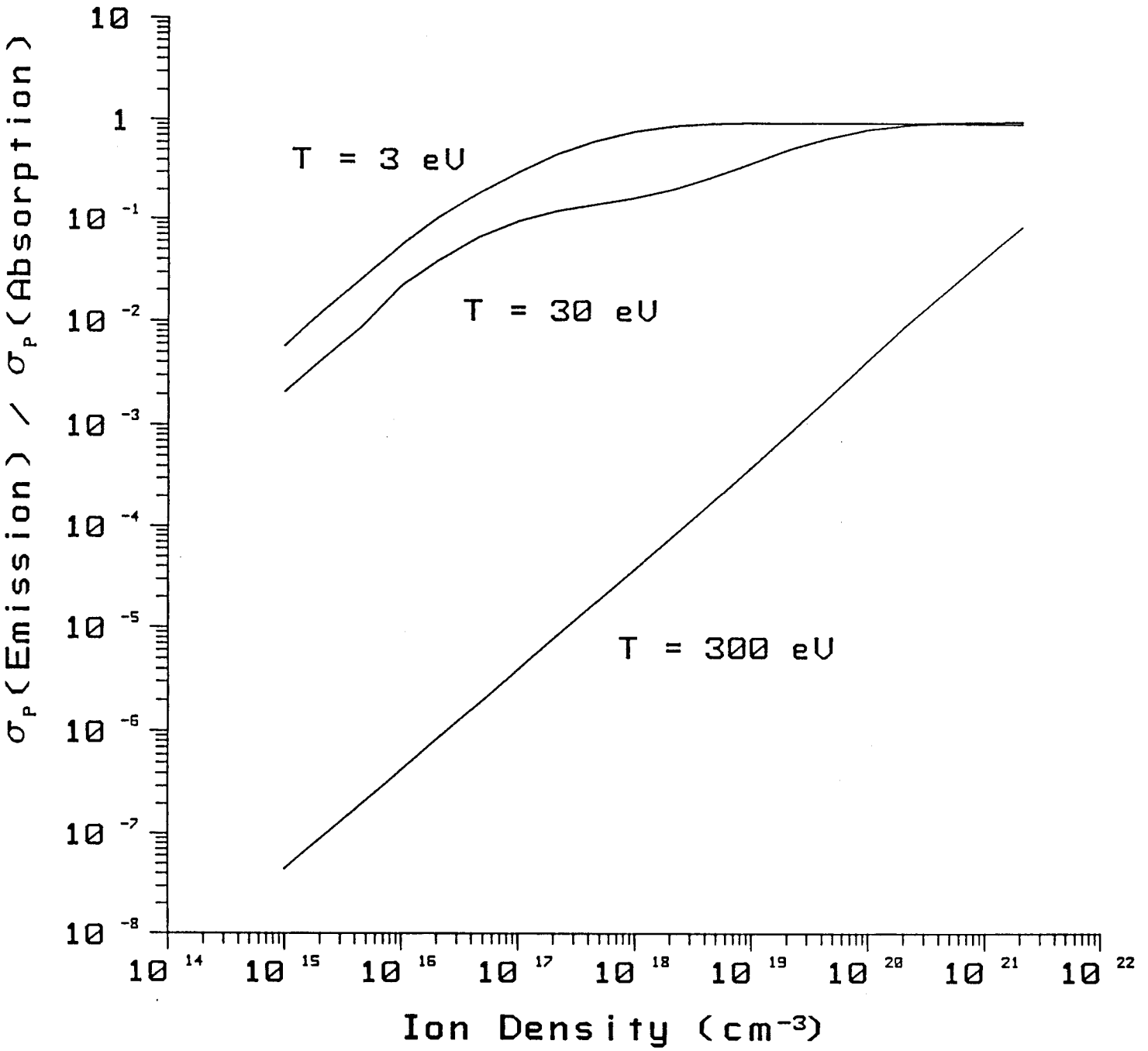

Figure 2.6. Ratio of the Planck mean absorption and emission rates for neon vs. density for temperatures of 3, 30, and 300 eV.

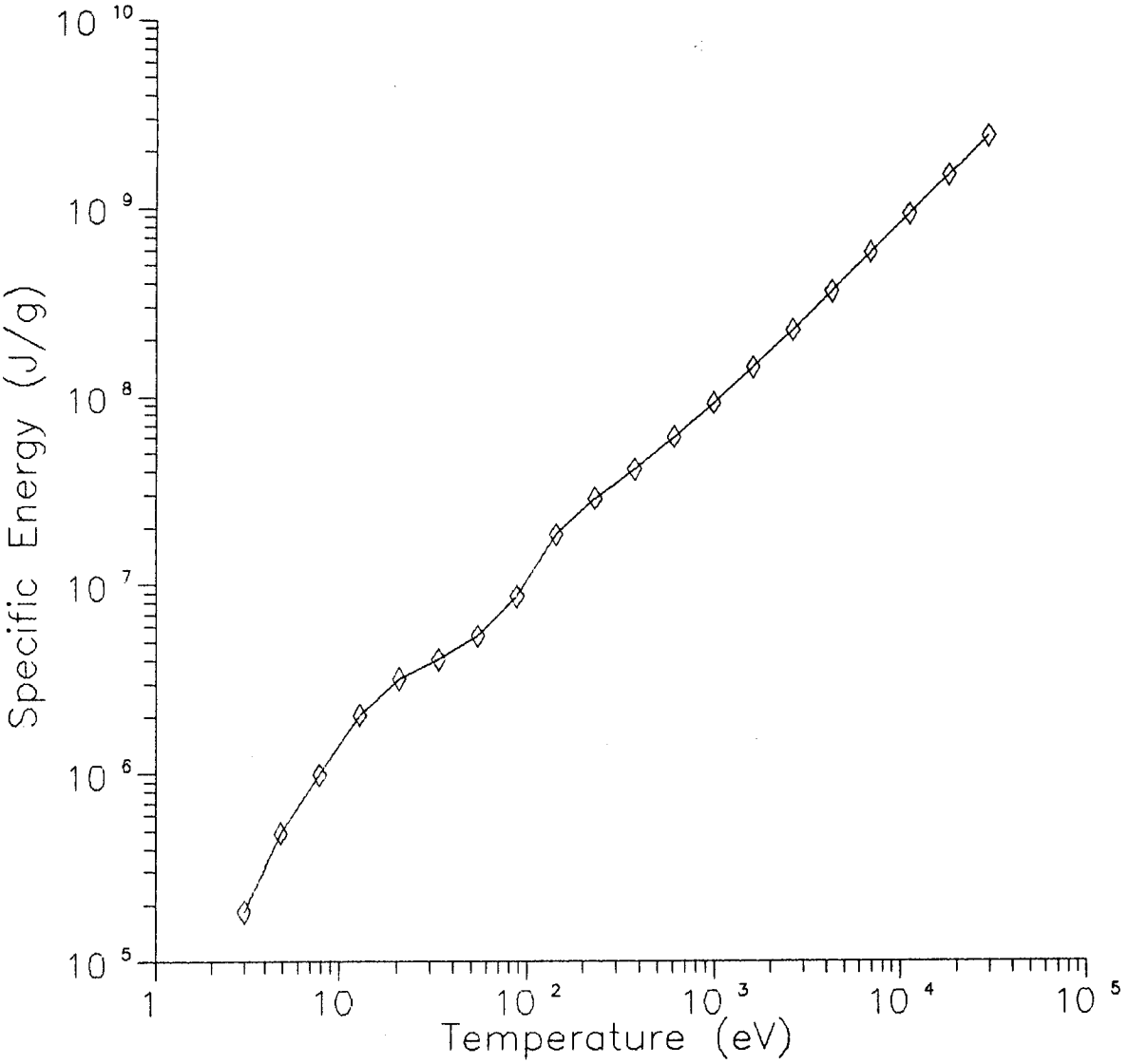

Figure 2.7. Specific energy vs. temperature for a low density nitrogen plasma.

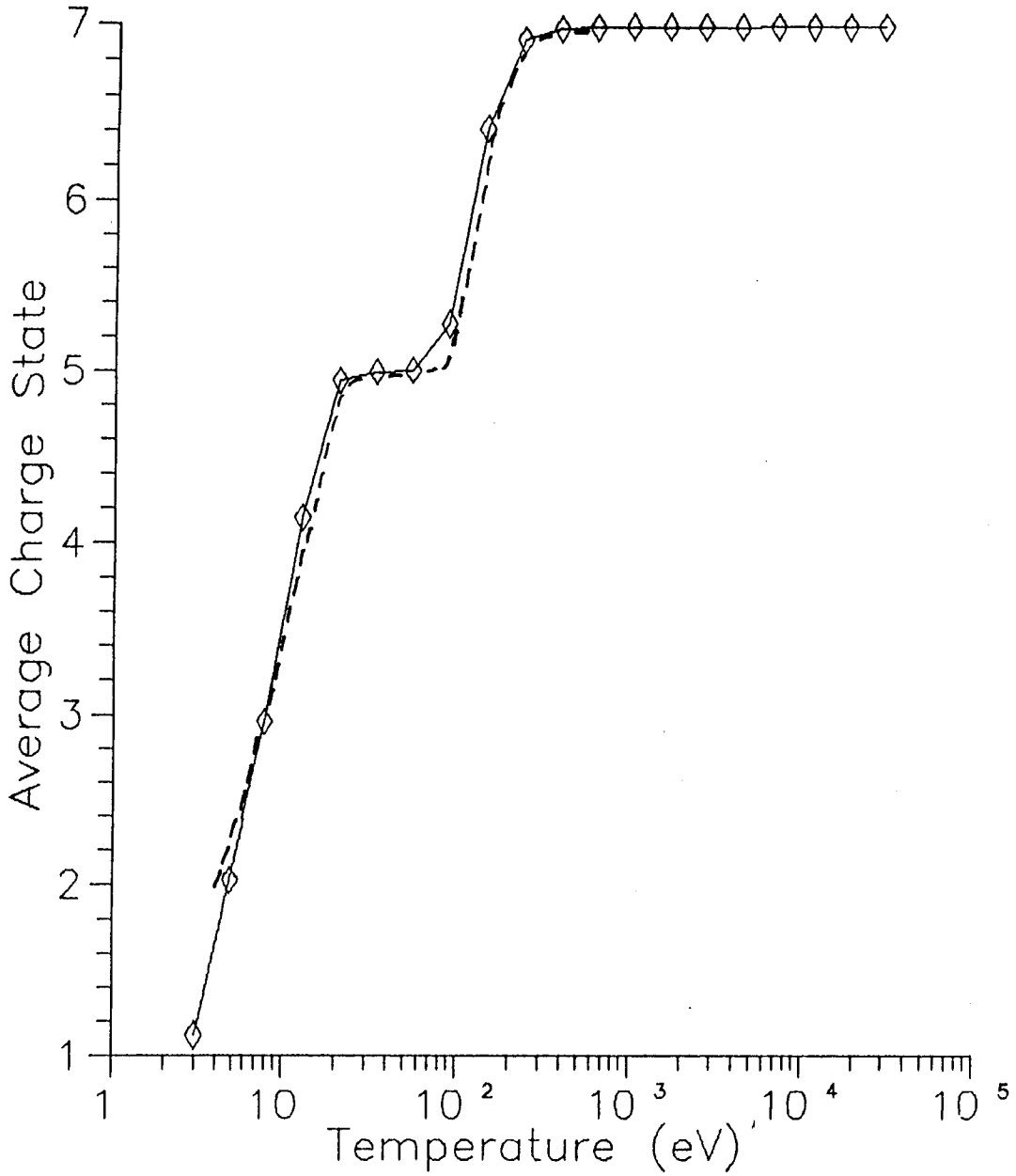

Figure 2.8. Average change state vs. temperature for a low density nitrogen plasma.

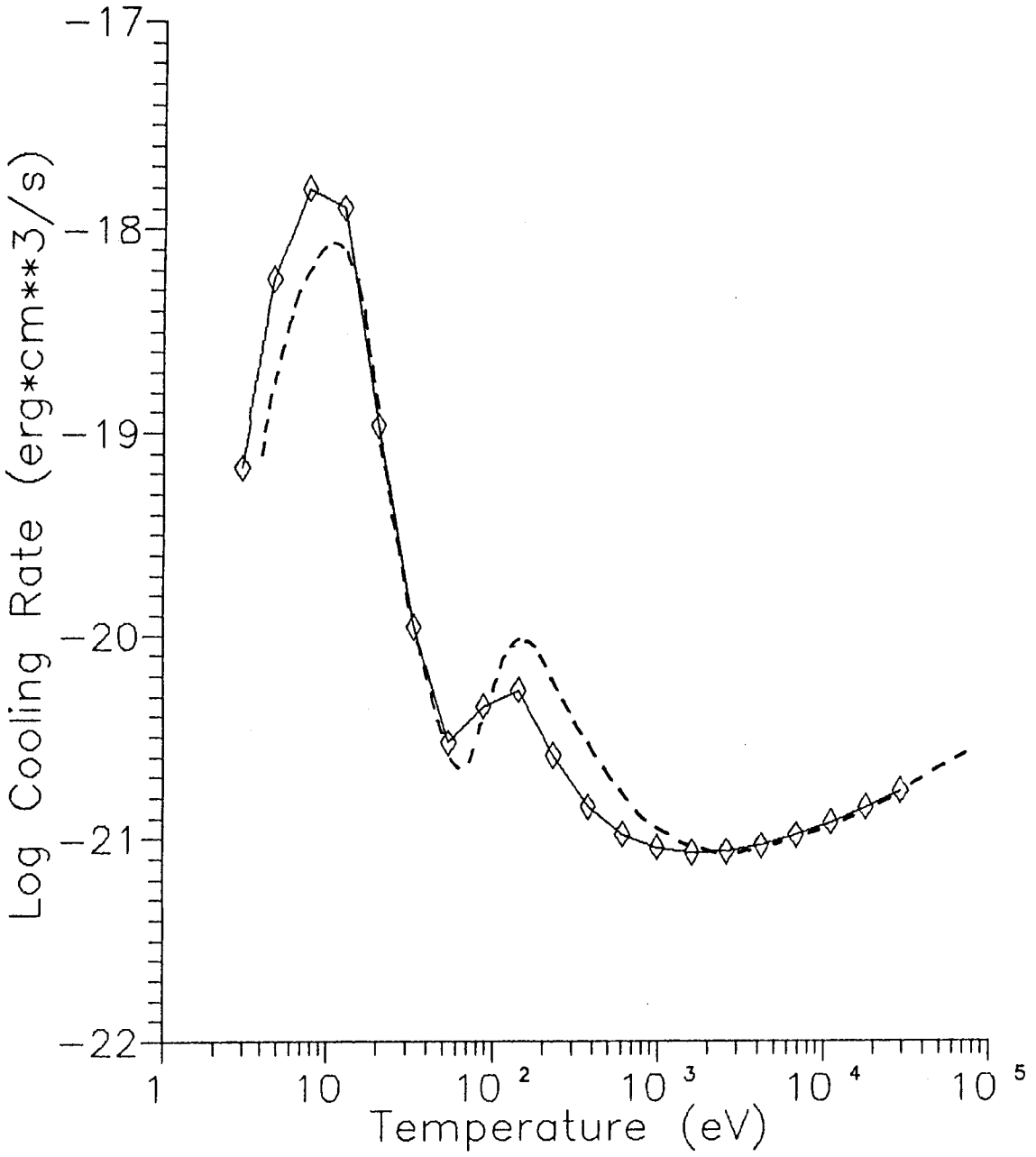

Figure 2.9. Plasma cooling rate vs. temperature for a low density nitrogen plasma.

obtained by Argo et al. [14], which are represented by the dashed lines in Fig. 2.10.

Example 3

In the final example, we present results for the cooling rates of a "solar composition" mixture of H, He, C, N, O, Ne, Mg, Si, S, and Fe. The relative number densities are: f_H=0.94, f_{He}=0.06, f_C=3.4x10^{-4}, f_N=0.8x10^{-4}, f_O=5.6x10^{-4}, f_{Ne}=0.7x10^{-4}, f_{Mg}=0.29x10^{-4}, f_{Si}=0.34x10^{-4}, f_S=0.16x10^{-4}, and f_{Fe}=0.27x10^{-4}. The plasma emission rate is plotted in Fig. 2.11 as a function of temperature. The ion density is 10^8 cm^{-3} . Although plasma is composed primarily of H and He, the greatest contribution to the emission rate at temperatures above ~ 10^5 K is due to the bound-bound transitions of the minor constituents.

The dashed line in Fig. 2.11 is from the calculations of Shapiro and Moore [15].

2.2.5 Application to ICF Target Chambers

In this section, we examine the influence of non-LTE processes on the radiation and hydrodynamic energy transport in ICF target chamber plasmas. To study these effects, we used the one-dimensional Lagrangian radiation-hydrodynamics code, CONRAD [16,17]. Spherical symmetry is assumed. Radiation is transported in 20 photon energy groups using a flux-limited diffusion model, and electron conduction in the background plasma is calculated using Spitzer conductivities [18].

Energy from the target is deposited into the background gas using time-dependent debris ion and energy-dependent x-ray deposition models. In the calculations discussed below, the target x-ray and debris ion yields are 150 MJ and 50 MJ, respectively. The target x-ray spectrum is based on target

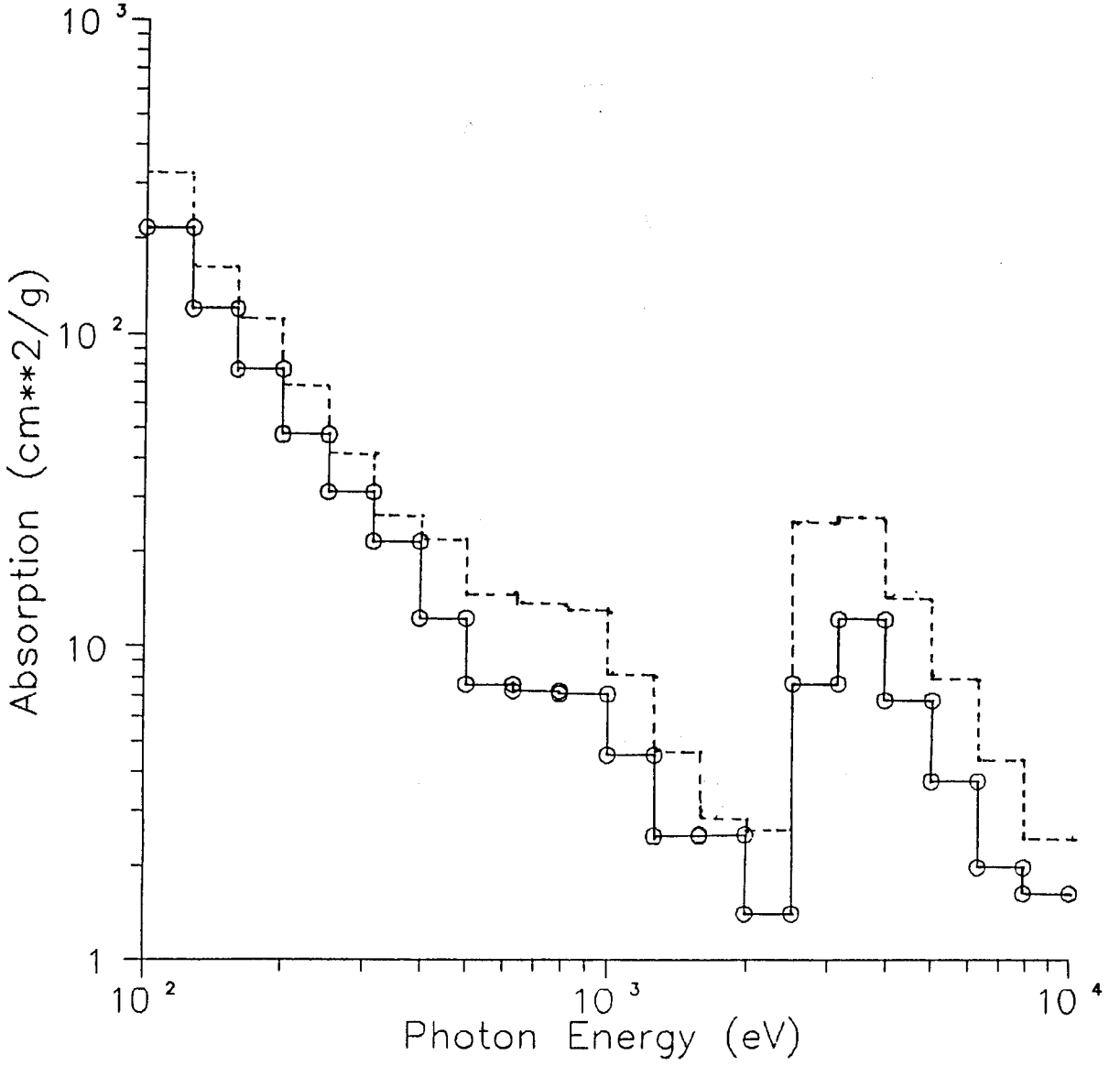

Figure 2.10. Rosseland mean group opacities for a SiO_2 plasma at T = 500 eV and ρ = 0.1 g/cm^3.

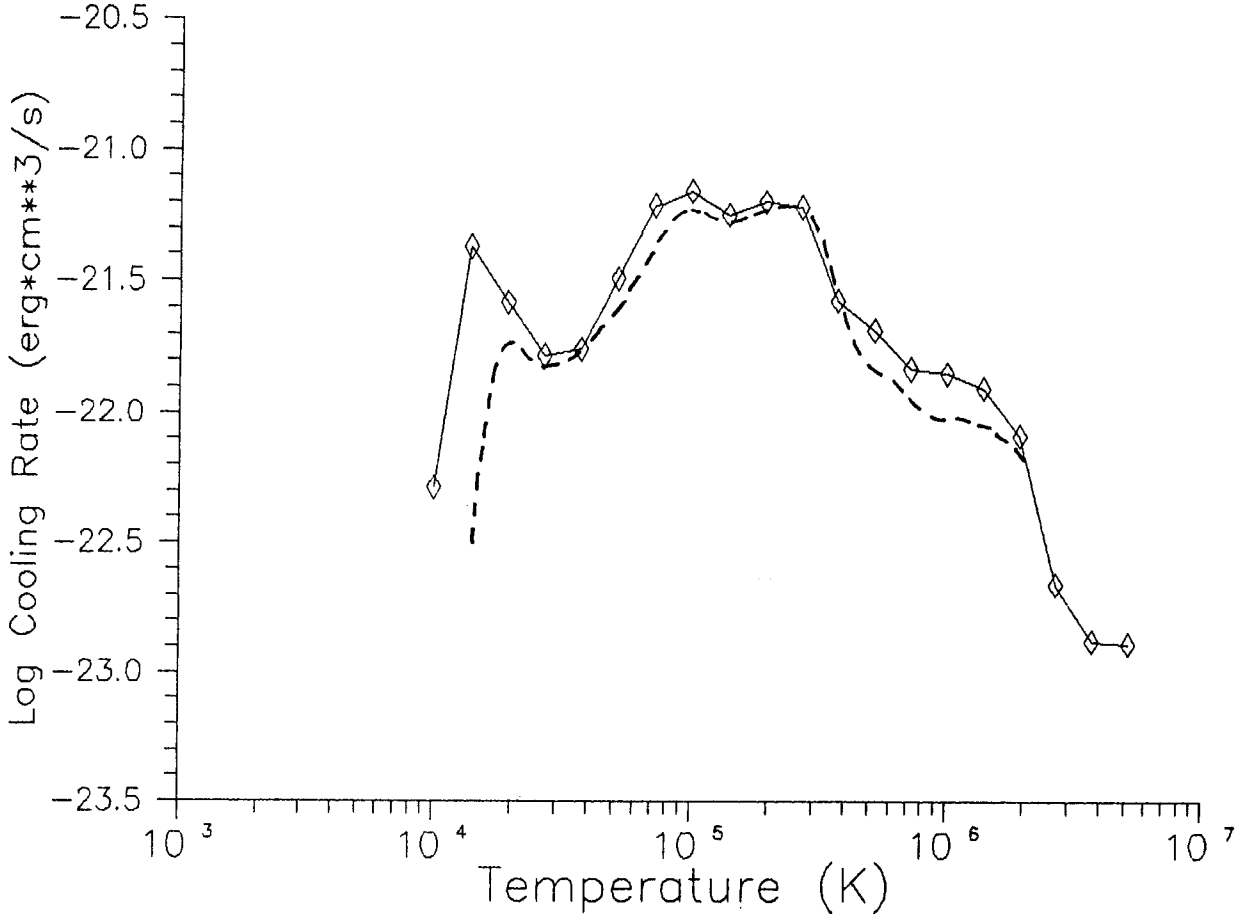

Figure 2.11. Plasma cooling rate vs. temperature for a low density "solar composition" plasma.

burn calculations [19] using the PHD-IV radiation-hydrodynamics code [20], and is shown in Fig. 2.12. The debris ions expand isotropically from the explosion point source at a constant rate during the first 100 ns of each simulation. The initial properties of debris ions are listed in Table 2.1. The debris ions transfer momentum and energy to the background plasma via ion-atom, ion-electron, and ion-ion collisions. The rate of energy loss by the debris ions is computed using a stopping power model which includes high temperature effects (i.e., free electron-ion collisions), and is described in detail elsewhere [21].

Table 2.1. Target Debris Ion Energies

Debris Ion	Initial Kinetic Energy	Total Energy (MJ)
Deuterium	1.9 keV/particle	0.082
Tritium	2.9 keV/particle	0.122
Helium	3.8 keV/particle	0.070
Lithium	6.6 keV/particle	1.89
Lead	198 keV/particle	23.9

The target chamber radius in these calculations is varied between 1 and 3 meters, and the background gas is composed of pure argon. For background gas densities $\gtrsim 10^{17}$ cm^{-3}, the debris ions deposit their energy within several centimeters of the target. On the other hand, the photon mean free paths of the target x-rays are often considerably longer, and a significant fraction of their energy will not be absorbed by the background gas.

Figure 2.13 shows the radiation flux as a function of time at the grid boundary (which represents the chamber wall) located 3 meters from the target. In this calculation, the background gas initially has a uniform density of 3.55×10^{15} cm^{-3}, corresponding to a pressure of 0.1 torr at room temperature. The solid curve represents the results obtained using an argon equation of state and opacities in which non-LTE processes are considered. For

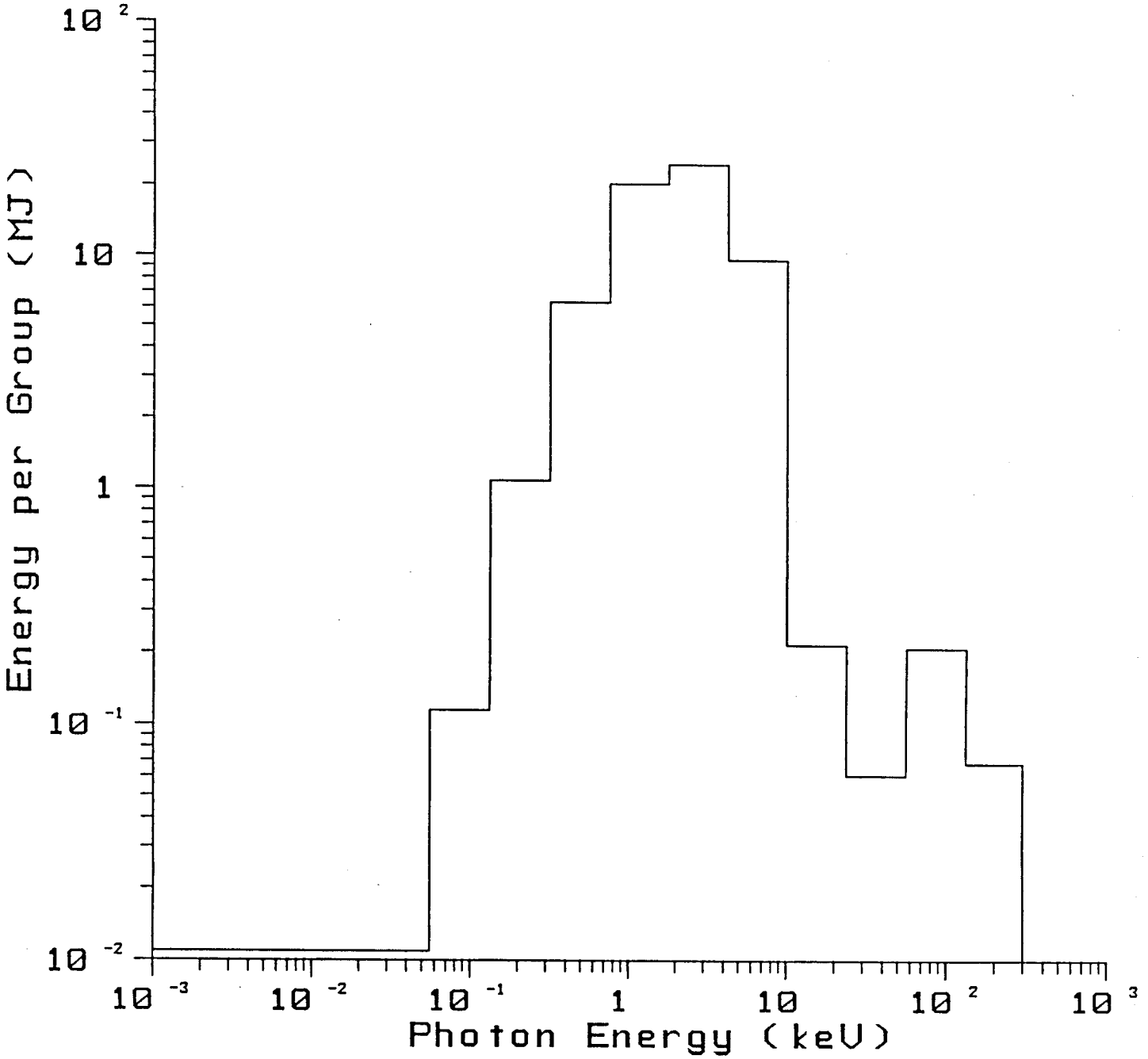

Figure 2.12. Target x-ray spectrum for radiation-hydrodynamic simulations.

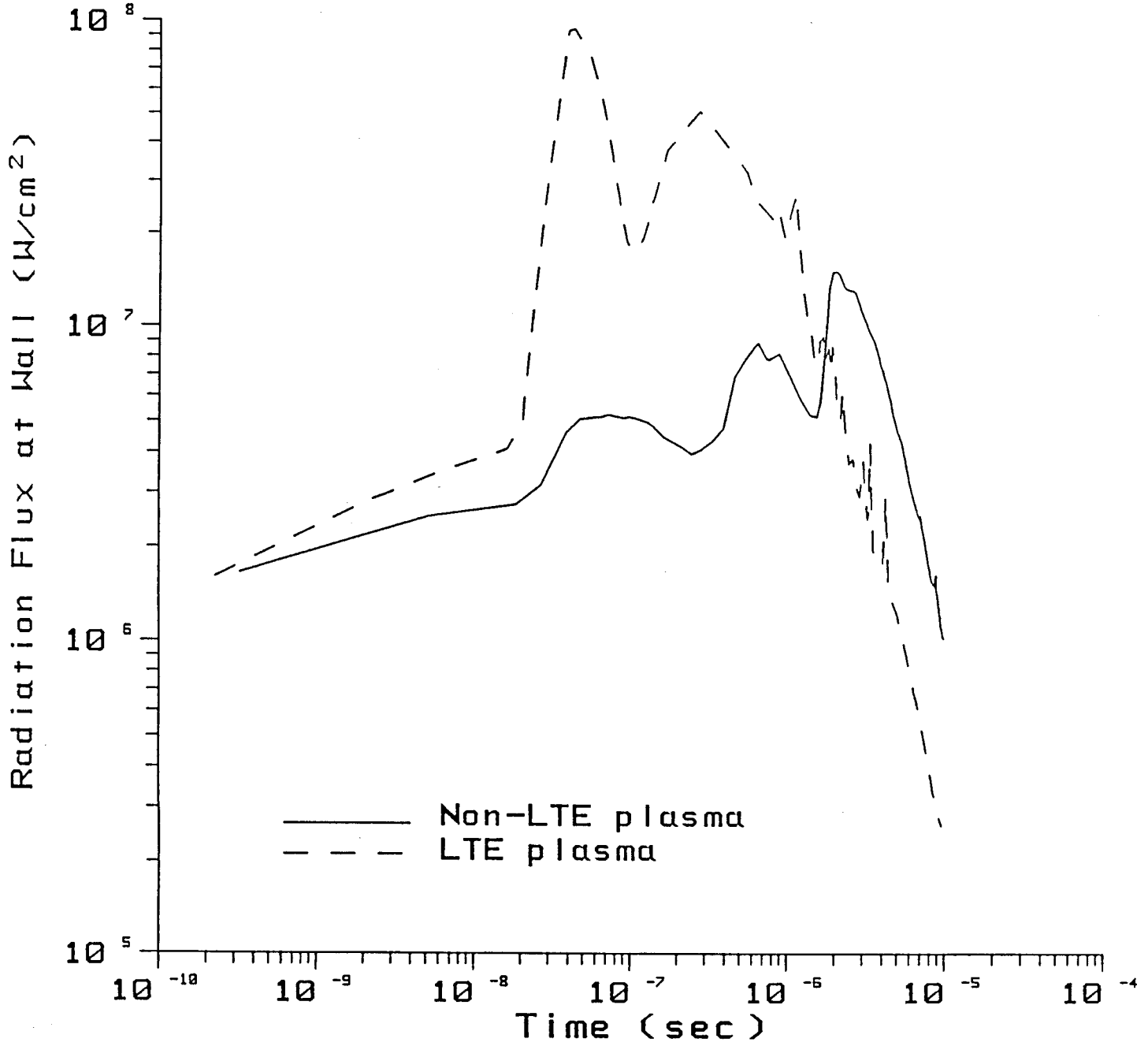

Figure 2.13. Radiation flux vs. time at a surface located 3 meters from the target. The background plasma is argon and has an initial density of 3.55×10^{15} cm^{-3}.

comparison, the dashed line shows the flux calculated using a strictly LTE equation of state and opacities. Including non-LTE effects in the background plasma tends to reduce the flux by roughly an order of magnitude. This is due to the fact that radiative deexcitation decreases the fraction of excited state ions, which in turn reduces the plasma emission rate. In the LTE case, the flux drops rapidly after ~ 2 μs because there is very little energy remaining in the plasma.

The time-integrated flux at 3 meters is shown in Fig. 2.14. Again, the non-LTE plasma is seen to lose its energy at a much slower rate. In this calculation, the total energy absorbed by the background plasma from the x-rays and debris ions was 72 MJ. Thus, at a distance of 3 meters, the plasma has lost all of its energy when the energy radiated to the wall reaches 64 J/cm^2.

Because of the lower non-LTE plasma emission rates, the microfireball will retain its thermal energy for a longer period of time. This is shown in Fig. 2.15, where the temperature at the center of the microfireball is plotted as a function of time. In both the LTE and non-LTE cases, the temperatures reach a maximum of several keV at ~ 10^{-1} μs as the debris ions deposit their energy. The central temperature calculated using non-LTE plasma properties remains above 100 eV out to ~ 10 μs. On the other hand, when non-LTE processes are neglected, the central temperature is predicted to decrease rapidly down to < 10 eV at ~ 5 μs.

Figure 2.15 clearly illustrates the importance of non-LTE processes in the background plasma following an inertial fusion target explosion. These processes will especially need to be considered in the interpretation of diagnostic data from high-gain target experiments, such as those envisioned for the Laboratory Microfusion Facility [22]. Non-LTE effects may also be

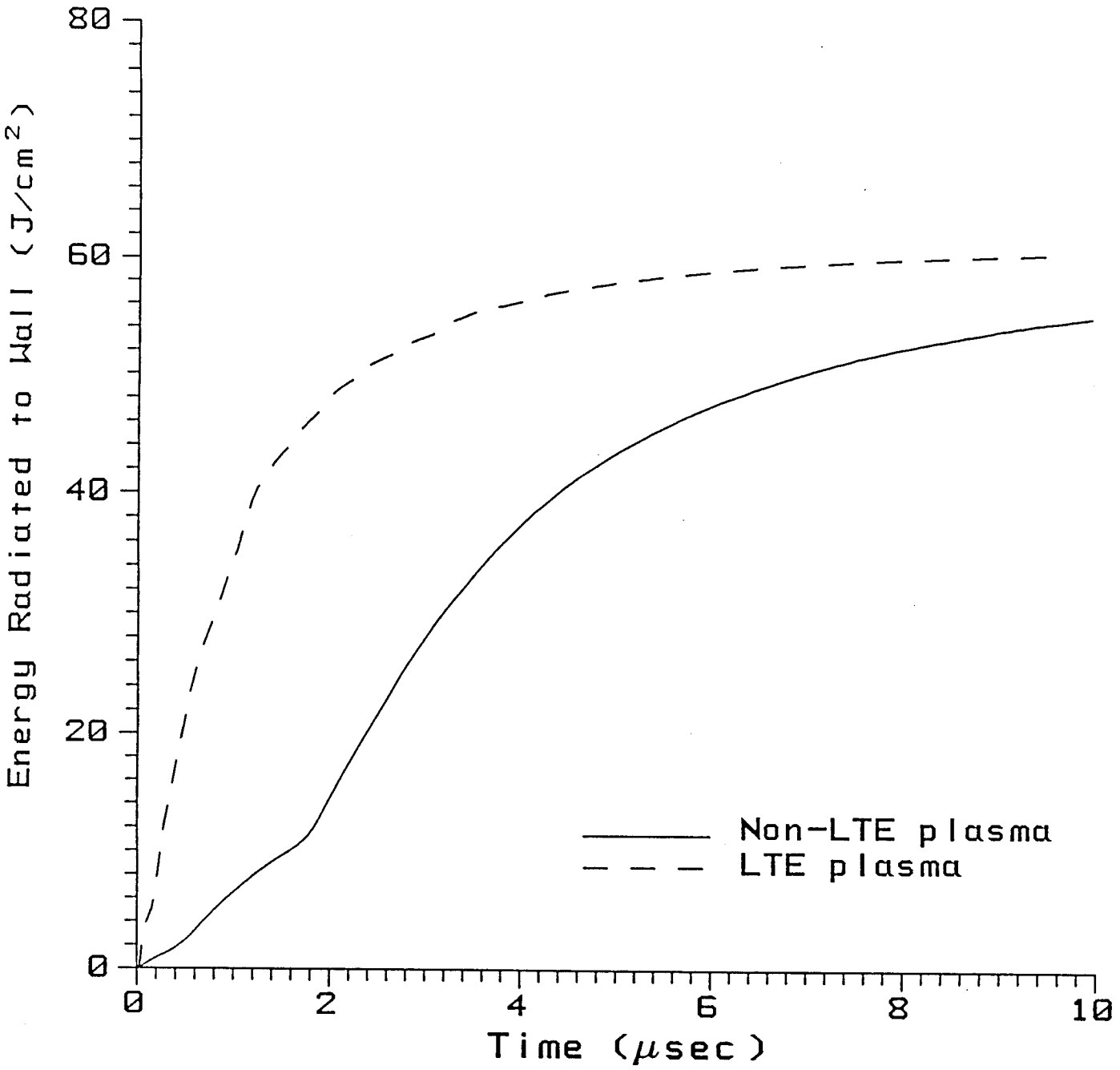

Figure 2.14. Time-integrated energy radiated to a surface located 3 meters from the target vs. time. The background plasma is argon and has an initial density of 3.55×10^{15} cm^{-3}.

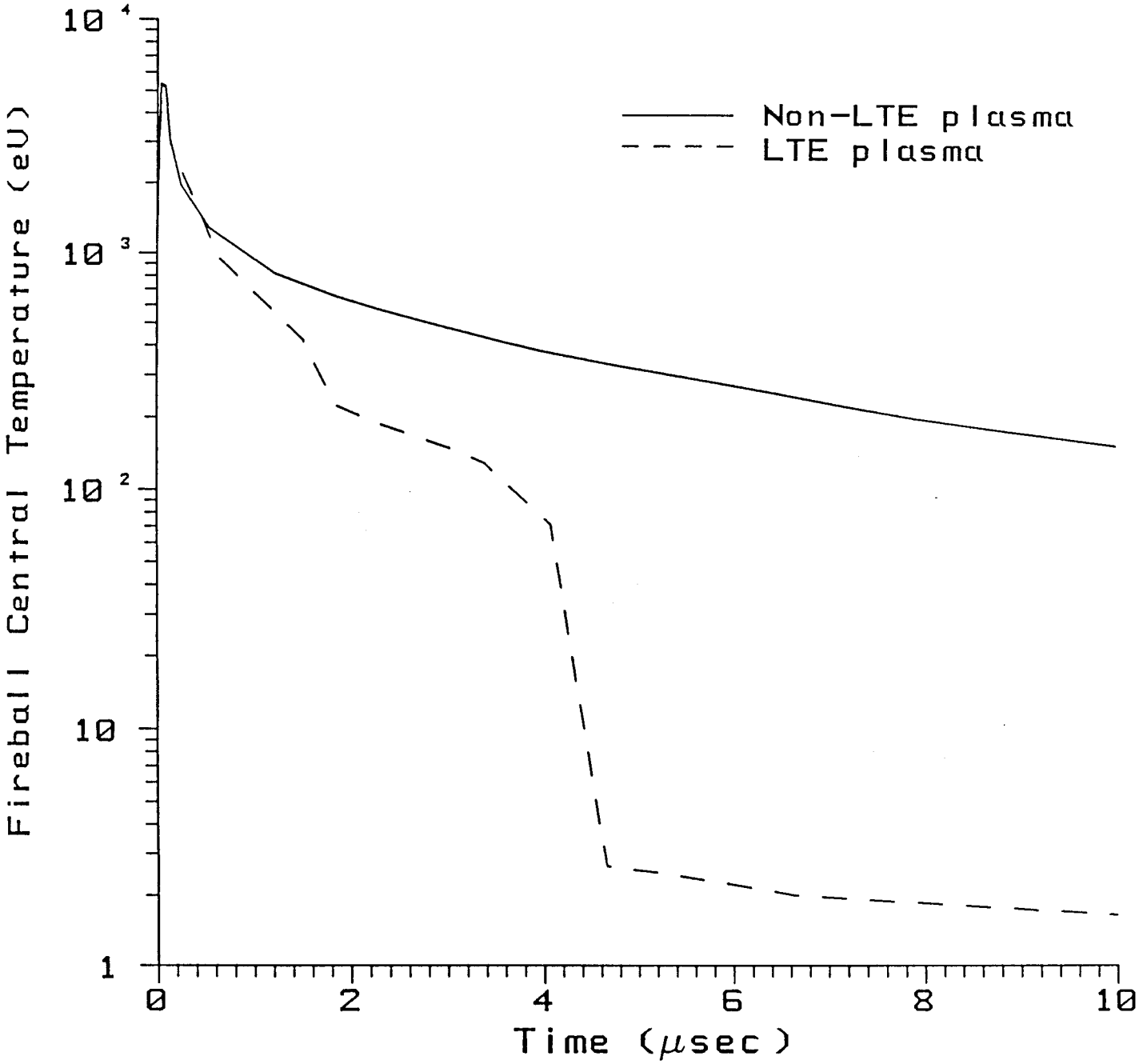

Figure 2.15. Temperature at the center of the microfireball vs. time. Non-LTE processes were included in the calculation of the solid curve. The dashed curve represents results of an LTE plasma.

important in target chambers with low density ($\lesssim 10^{14}$ cm^{-3}) background gases. In this situation, material ablated from the wall by target x-rays will interact with the later arriving target debris ions. This vapor could then be heated to temperatures ~ 10 to 10^2 eV, producing a non-LTE plasma. Thus, non-LTE effects will be important for a variety of processes associated with inertial fusion target explosions.

The lower emission rate of non-LTE plasmas also produces a stronger shock front emanating from the target. Figure 2.16 shows the pressure at a surface located 1 meter from the target as a function of time. In this problem, the initial background gas density was 3.55×10^{16} cm^{-3}, corresponding to a pressure of 1 torr at room temperature. The pressure determined using non-LTE plasma properties is represented by the solid curve. The dashed curve represents the pressure calculated using an LTE equation of state and opacities. For comparison, the dotted line in Fig. 2.16 represent the results from a calculation in which the plasma neither emitted nor absorbed radiation -- i.e., a pure hydrodynamics calculation.

In the non-LTE calculation, the average shock velocity (as determined by the arrival time at 1 meter), is almost twice as fast as the shock in the LTE case. Also, the peak pressure at 1 meter is seen to be roughly an order of magnitude higher in the non-LTE case. In the calculation with no plasma emission, the average shock velocity is more the twice as fast as in the non-LTE calculation and four times faster than the LTE shock. This is because as the plasma behind the shock retains more of its thermal energy, the pressure behind the shock front remains higher and there is more energy available to perform work (PdV) on the blast wave.

The shock-produced impulse at the surface in these calculations is 18, 11, and ~ 100 Pa-s for the non-LTE, LTE, and "no radiation" cases,

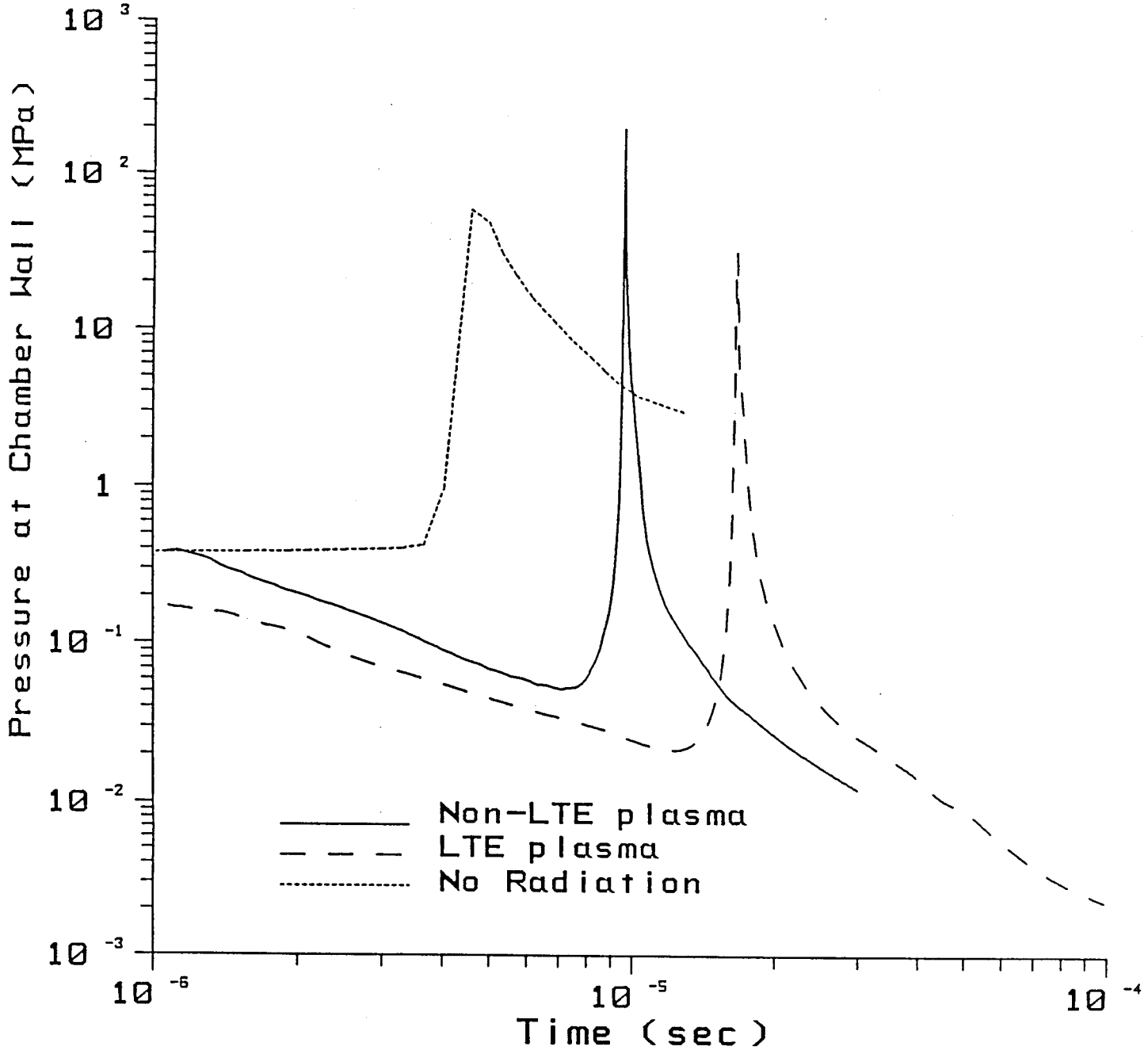

Figure 2.16. Pressure at a surface located 1 meter from the target vs. time. The background plasma is argon and has an initial density of 3.55×10^{16} cm^{-3}.

respectively. Clearly, radiation effects play a significant role in reducing the strength of the shock as it expands away from the target. However, the shock-generated impulse can be noticeably underestimated if the plasma properties are based on LTE assumptions. Determining the strength of the shock is critical because impulses of this magnitude are capable of inflicting an unacceptable level of damage to the chamber structure. Because of this, the shock properties play a major role in the designs of ICF target chambers.

2.2.6 Conclusions Concerning Non-LTE Effects

We have used IONMIX to calculate equations of state and radiative properties of plasmas over a range of densities and temperatures relevant to ICF target chamber applications, and which encompass the transition between the LTE and non-LTE plasma regimes. It was found that for plasma densities of $\sim 10^{18}$, 10^{19}, and 10^{21} cm^{-3}, 2-body (non-LTE) atomic processes dominate at temperatures $\gtrsim$ 1, 10, and 100 eV, respectively. At densities $< 10^{17}$ cm^{-3} collisional recombination and deexcitation are unimportant and the assumption of local thermodynamic equilibrium is invalid at all temperatures $\gtrsim$ 1 eV. Non-LTE processes in low density plasmas produce a relative depopulation of the excited states of ions, which in turn can significantly reduce the plasma emission rate.

Numerical simulations of ICF target chamber environments indicate that the background plasma will often -- though not always -- be dominated by non-LTE atomic processes. For target chambers with relatively high density background gases ($\gtrsim 10^{17}$ cm^{-3}), both 2-body (radiative) and 3-body (collisional) recombination and deexcitation processes must be fully considered when calculating equation of state and radiative properties of a plasma. The lower (relative to LTE) plasma emission rates can result in: (1) the microfireball

retaining its thermal energy for a longer period of time; (2) a more energetic blast wave capable of producing a stronger impulse at the chamber wall; and (3) a lower radiation flux at the chamber wall, which can potentially reduce the amount of material vaporized from the wall. In addition, non-LTE processes must be considered when material vaporized from the chamber wall is heated by the target debris ions. Thus, non-LTE processes are predicted to play a major role in a variety of ICF target chamber phenomena.

References for Section 2

[1] R.R. Peterson and G.A. Moses, Comput. Phys. Commun. 28 (1983) 405.

[2] G.I. Kerley, LASL-79-62, Los Alamos National Laboratory, Los Alamos, NM (1980).

[3] J.J. MacFarlane, University of Wisconsin Fusion Technology Institute Report UWFDM-750 (1987), submitted to Comput. Phys. Commun.

[4] R.R. Peterson, J.J. MacFarlane, G.A. Moses, M. El-Afify, and M.L. Corradini, University of Wisconsin Fusion Technology Report UWFDM-725 (1987).

[5] M. Uesaka, R.R. Peterson, and G.A. Moses, Nucl. Fusion 24 (1984) 1137.

[6] L.A. Glenn, Nucl. Eng. and Design 54 (1979) 1.

[7] D. Mihalas, Stellar Atmospheres (W.H. Freeman, San Francisco, 1978).

[8] Y.B. Zeldovich and Y.P. Raizer, Physics of Shock Waves and High-Temperature Hydrodynamic Phenomena (Academic Press, New York, 1966).

[9] D.E. Post, R.V. Jensen, C.B. Tarter, W.H. Grasberger, and W.A. Lokke, At. Data Nucl. Data Tables 20 (1977) 397.

[10] M.J. Seaton, Mon. Not. R. Astr. Soc. 110 (1959) 81.

[11] A. Burgess, Astrophys. J. 141 (1965) 1588.

[12] See, e.g., D.A. McQuarrie, Statistical Mechanics (Harper and Row, New York, 1976).

[13] W.J. Karzas and R. Latter, Astrophys. J. Suppl. 6 (1961) 167.

[14] M.F. Argo and W.F. Huebner, J. Quant. Spectrosc. Radiat. Transfer 16 (1976) 1091.

[15] P.R. Shapiro and R.T. Moore, Astrophys. J. 207 (1976) 460.

[16] G.A. Moses, R.R. Peterson, and T.J. McCarville, Comput. Phys. Commun. 36 (1985) 249.

[17] R.R. Peterson and J.J. MacFarlane, University of Wisconsin Fusion Technology Institute Report UWFDM-670, revised (1988).

[18] L. Spitzer, Physics of Fully Ionized Gases, Second Edition (Interscience, New York, 1966).

[19] HIBALL Group, University of Wisconsin Fusion Technology Institute Report UWFDM-450 (1981).

[20] G.A. Moses, G.R. Magelssen, R. Israel, and T. Spindler, University of Wisconsin Fusion Technology Institute Report UWFDM-194 (revised 1982).

[21] J.J. MacFarlane, G.A. Moses, and R.R. Peterson, University of Wisconsin Fusion Technology Institute Report UWFDM-723 (1987).

[22] W.J. Hogan, Bull. Amer. Phys. Soc. 32 (1987) 1788.

3. CONRAD COMPUTER CODE DEVELOPMENTS

Improvements to CONRAD have been made in two general areas: the vaporization/condensation model and the ion deposition model. For the vaporization/condensation model, we expanded the Lagrangian mesh to include the condensed (wall) material. This approach eliminates the need for rezoning and allows for better numerical conservation of energy. Modifications to the vaporization/condensation model are described in Section 3.1.

The ion deposition model has been modified so that the time-dependent ionization states of the debris ions are computed by solving the appropriate rate equations. In the past, we have assumed the debris ion charge states did not change throughout the simulation. When the background gas pressure is high so that the ion stopping distances are small, the time-dependence of the debris ion ionization states is unimportant. However, if the background gas pressure is $\lesssim$ 1 mtorr, their time-dependence must be tracked to accurately determine the energy deposition in the background gas. Improvements to the ion deposition model are discussed in Section 3.2.

3.1. Vaporization/Condensation Model

Vaporization of the target chamber first wall effectively occurs in two phases. During the first phase, hard x-rays from the target travel at the speed of light to the wall and, because of their long mean free paths, deposit their energy volumetrically in the condensed region. During the second phase, thermal radiation -- i.e., energy absorbed by the background gas and reemitted by the microfireball -- deposits its energy near the surface of the condensed region. In CONRAD, we model both of these phenomena, using a "volumetric" vaporization model at very early times and a "surface" vaporization model at later times.

In recent years, CONRAD employed vaporization and condensation models in which the position of the vapor/condensate interface was fixed, and mass flowed across the interface into the Lagrangian cells in the vapor region. Periodically, a rezoning procedure was used to redistribute mass throughout the Lagrangian mesh, causing some unphysical smoothing of the plasma properties. In addition, energy conservation was not strictly monitored throughout the calculation, making it difficult to assess the reliability of the results.

We have developed an alternative approach to simulating the vaporization and condensation of the condensed regions in an ICF target chamber. The modifications to the old model are primarily numerical in nature, with the underlying physics remaining much the same. In the new model, the Lagrangian mesh extends beyond the cavity (vapor region) into the condensed (wall) region. As material is vaporized, the Lagrangian cells undergo hydrodynamic motion. Later, as each cell recondenses, hydrodynamic motion ceases. No mixing occurs between the background gas--which is assumed to be a non-condensable gas--and the vaporized wall material. This approach eliminates the need for rezoning, and allows for better numerical energy conservation.

Hard x-rays emitted by the target are deposited "volumetrically" in the condensed region; i.e., over a depth of $\sim 10^{-3}$ to 10^{-2} cm. In practice, this takes place during the first time cycle of a CONRAD simulation (or during the first few cycles if the time-dependent x-ray deposition option is used). A typical energy deposition profile is illustrated in Fig. 3.1, where the energy density is plotted as a function of distance behind the vapor/condensate interface. The condensed layer is divided into 3 regions. In region A, the energy density is higher than the vaporization energy density. All material in this region becomes superheated vapor ($T > T_{vap}$, the vaporization temperature). In region C, the energy density remains lower than the "sensible"

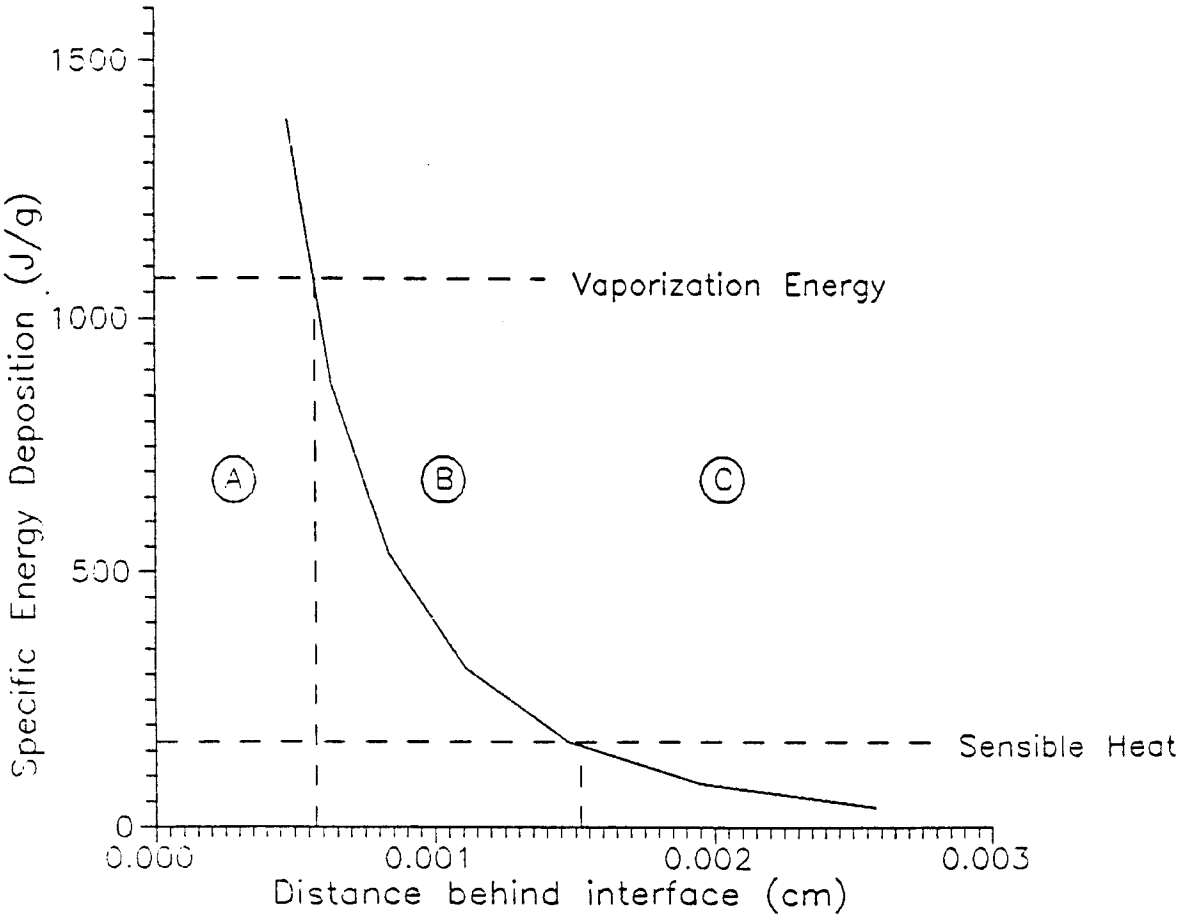

Figure 3.1. Specific energy in a solid (or liquid) vs. distance behind the vapor/condensate interface.

energy density. None of this material is vaporized during the volumetric vaporization phase, and the temperature remains below T_{vap}. In region B, the energy density lies between the vaporization and sensible energies, and the temperature throughout the region is equal to T_{vap}. To determine the amount of material from region B that gets vaporized, we redistribute the energy so that: (1) none of the condensed region has an energy density between the vaporization and sensible values, and (2) energy is conserved. The redistributed energy is represented by the dotted line in Fig. 3.1.

After material is vaporized, the pressure in the vapor region near the interface becomes very high because of the high density. This causes material to be rapidly accelerated away from the interface, and provides a "recoil" impulse to the wall. CONRAD monitors the pressure at the interface and computes the impulse on the wall directly.

In CONRAD, the primary distinction between the vapor and condensed phases is that vapor cells undergo hydrodynamic motion. The condensed region cells remain stationary due to chemical bonding. In addition, the conservation of momentum and energy equations are solved over all vapor cells. In the condensed region, a one-dimensional conduction equation is solved to determine the energy transport within the region.

The amount of material vaporized during the volumetric phase can be adjusted by setting ISW(25) = 2. This allows only material with energy density greater than the vaporization energy density to be vaporized. That is, none of the material in region B is vaporized. This model is less reliable, however, because energy is not conserved.

After the volumetric deposition phase, radiant energy transported to the condensed region will be effectively deposited at the surface of the interface because of the shorter photon mean free paths. The vaporization and conden-

sation rates are calculated using the kinetic theory model described by Labuntsov and Kryukov [1]. The mass vaporization rate is given by:

$$(dm/dt)_v = \frac{2}{3} P_{sat} A_{wall} \left(\frac{\mu}{RT_v}\right)^{1/2} \tag{3.1}$$

where A_{wall} is the surface area of the wall, T_v is the vapor temperature, R is the gas constant, μ is the mean atomic weight of the condensable material, and P_{sat} is the saturation vapor pressure:

$$P_{sat} = \exp\left[\frac{\Delta H_v}{kT_{vap,o}}\left(1 - \frac{T_{vap,o}}{T_c}\right)\right] \text{ bar} \tag{3.2}$$

ΔH_v is the specific heat of vaporization, k is Boltzmann's constant, T_c is the condensate temperature at the interface, and $T_{vap,o}$ is the vaporization temperature at 1 bar. The mass condensation rate is:

$$(dm/dt)_c = \frac{2}{3} f_s f_{nc} P_{vap} A_{wall} \left(\frac{\mu}{RT_v}\right)^{1/2} \tag{3.3}$$

where P_{vap} is the vapor pressure given by the ideal gas law:

$$P_{vap} = \rho_v \frac{RT_v}{\mu} \tag{3.4}$$

and ρ_v is the vapor density. In Eq. (3.3), f_s is the sticking coefficient, and f_{nc} is a correction factor for noncondensable gas effects. We realize that when $f_s \cdot f_{nc} \neq 1$, the net flux between the vapor and condensed phases is nonzero when the vapor pressure equals the saturation vapor pressure. We intend to correct this in the future.

Lagrangian cells undergo hydrodynamic motion only after an entire cell is vaporized. Figure 3.2 illustrates the evolution of mesh points during a typical simulation. Vapor cells are to the left of the dashed line and the condensed region is to the right of it. The "+"s represent the cell boundaries and the vertical dashed line represents the vapor/condensate interface. A short time after the target explodes ($t_1 = t_o + \varepsilon$), the target's hard x-rays are deposited in the condensed region, vaporizing a number of cells. Since the vaporized mass is not in general an integral number of cells, the interface is located between cell boundaries. At later times (t_2), the vapor expands away from the wall while thermal radiation from the fireball vaporizes additional cells. No mass is ever exchanged between Lagrangian cells as mixing effects are neglected.

As the radiative flux from within the cavity subsides and the temperature at the surface of the condensed region drops, the condensation rate begins to exceed the vaporization rate. Again, the interface is tracked as condensation occurs. Fig. 3.2 shows vapor moving toward the interface as material recondenses back onto the surface (t_3 and t_4). If any portion of a Lagrangian cell has condensed, it no longer undergoes hydrodynamic motion.

To calculate energy transport within the condensed region, CONRAD solves the one-dimensional conduction equation:

$$C_p \frac{dT}{dt} = \frac{\kappa}{\rho} \frac{d^2T}{dx^2} + S \qquad (3.5)$$

where C_p is the specific heat at constant pressure, κ is the thermal conductivity, ρ is the density in the condensed region, T is the temperature, and x the spatial coordinate. S is a source term which accounts for the radiative heat flux. In practice, only the first cell has a non-zero source term because the heat flux is assumed to be deposited at the surface.

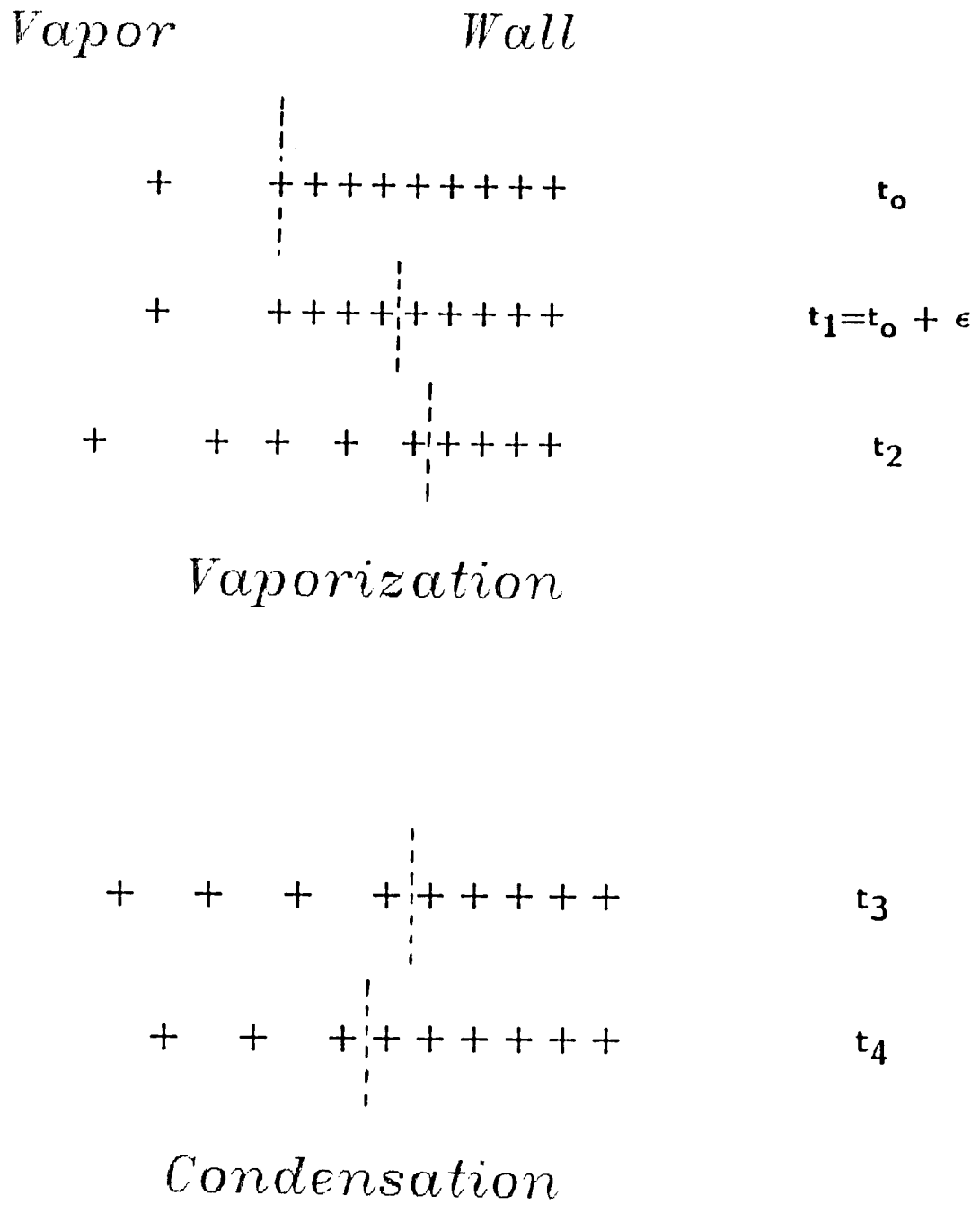

Figure 3.2. Schematic evolution of Lagrangian mass cells due to vaporization and condensation.

The conduction equation is also subject to the following boundary conditions. The temperature at the back of the condensed layer is constant (Dirichlet condition) as heat flows through the back of the condensed region. At the vapor/condensate interface, the conductive heat flux is assumed to be zero (Neumann condition).

Energy conservation is monitored for the entire vapor/condensate system. At the end of each time step, a check is made to ensure that the difference equations are conserving energy. After integrating the energy equations over time and space, the conservation equations for the vapor (plasma), condensate, and radiation can be written as:

Plasma	$e_p + T_p = e_p^o + T_p^o + H_p + E_{RP} - F_p - G_R + J_{PT}$
Condensate	$e_c = e_c^o + F_R + F_p - J_{PT} - Q_B + H_c$
Radiation	$e_R = e_R^o - E_{RP} - F_R + G_R$
Total	$e_{TOT} + T_P = e_{TOT}^o + T_P^o + H_P - Q_B$

The superscript "o" signifies the initial values. The physical definitions of each term are:

e_x total internal energy of the plasma, condensate, or radiation.

T_p total kinetic energy of the plasma.

H_x total source of energy to the plasma or condensate.

E_{RP} total radiation energy exchanged between the plasma and radiation field.

F_x total energy conducted across the vapor/condensate interface from the plasma or radiation.

G_R work exchanged between the gas and radiation.

Q_B total energy conducted through the back of the condensed region.

J_{PT} total energy exchanged during phase transformation between the plasma and condensate.

Each of these terms at time step "n" are given in finite difference form as follows:

$$e_x^{n+1} = \sum_{j=1}^{JMAX} (e_x)_{j-1/2}^{n+1} \, \Delta m_{o_{j-1/2}} \tag{3.6}$$

$$T^{n+1} = \frac{1}{4} \, \Delta m_{o_{JMAX-1/2}} \, (u_{JMAX}^{n+1/2})^2 + \frac{1}{2} \sum_{j=1}^{JMAX} \Delta m_{o_j} (u_j^{n+1/2})^2 \tag{3.7}$$

$$H_x^{n+1} = H_x^n + \Delta t^{n+1/2} \sum_{j=1}^{JMAX} (H_x)_{j-1/2}^{n+1/2} \, \Delta m_{o_{j-1/2}} \tag{3.8}$$

$$E_{RP}^{n+1} = E_{RP}^n + \Delta t^{n+1/2} \sum_{j=1}^{JMAX} (E_{RP})_{j-1/2}^{n+1/2} \, \Delta m_{o_{j-1/2}} \tag{3.9}$$

$$G_R^{n+1} = G_R^n + \Delta t^{n+1/2} \sum_{j=1}^{JMAX} u_j^{n+1/2} \, (r^{\delta-1})_j^{n+1/2} \, (P_{R_{j+1/2}}^{n+1/2} - P_{R_{j-1/2}}^{n+1/2}) + \Delta t^{n+1/2} \, u_{JMAX}^{n+1/2} \, (r^{\delta-1})_{JMAX}^{n+1/2} \, [P_{R_{JMAX+1}}^{n+1/2} - P_{R_{JMAX-1}}^{n+1/2}]/2 \tag{3.10}$$

$$F_P^{n+1} = F_P^n + \Delta t^{n+1/2} \left[\frac{r^{\delta-1}}{(\frac{\Delta r}{\kappa_P})}\right]_{JMAX}^{n+1/2} (T_{P_{JMAX+1/2}}^{n+1/2} - T_{P_{JMAX-1/2}}^{n+1/2}) \tag{3.11}$$

$$F_R^{n+1} = F_R^n + \Delta t^{n+1/2} \left[\frac{r^{\delta-1}}{(\frac{\Delta r}{\kappa_R}) + \frac{\Delta E_R}{F_R}}\right]_{JMAX}^{n+1/2} (E_{R_{JMAX+1/2}}^{n+1/2} - E_{R_{JMAX-1/2}}^{n+1/2}) \tag{3.12}$$

$$J_{PT}^{n+1} = J_{PT}^{n} + \Delta t^{n+1/2} \left[\left(\frac{dm}{dt}\right)_v^n - \left(\frac{dm}{dt}\right)_c^n\right] \cdot \left[e_v^{n+1} - e_c^{n+1}\right] \tag{3.13}$$

$$Q_B^{n+1} = Q_B^n + \Delta t^{n+1/2} \left(\frac{r^{\delta-1}}{\frac{\Delta r}{\kappa_P}}\right)^{n+1/2}_{JMAXC} \left(T^{n+1}_{P_{JMAXC+1/2}} - T^{n+1}_{P_{JMAXC-1/2}}\right) \tag{3.14}$$

The calculations usually conserve energy to within better than 10%.

We next present some typical results obtained using the new vaporization/condensation model. Figure 3.3 shows the mass vaporized from the wall as a function of time for target chambers with 2 initial gas pressures: 10 torr (solid curve) and 10^{-5} torr (dashed curve). In each case, the background gas was argon, the condensed region was $Li_{17}Pb_{83}$, the chamber radius was 3 m, the target x-ray energy was 63 MJ, and the target debris ion energy was 26 MJ. The target x-ray spectrum for the calculations described in this section is shown in Fig. 2.12.

The hard x-rays vaporize 3.3 kg for the 10 torr case and 10.4 kg for the 10^{-5} torr case. In CONRAD, the target x-ray deposition is computed during the first cycle, so the x-rays in effect have infinite velocity. For the low gas density case, more mass is initially vaporized because very little energy is absorbed by the background gas. A relatively small amount of LiPb is vaporized at later times when the debris ion energy is deposited in the LiPb vapor near the wall and reradiated to the vapor/condensate interface. For the high density case, a rather large amount of the target x-ray energy is absorbed by the background gas and reradiated to the wall. The maximum amount of LiPb vaporized in this problem is roughly 40 kg.

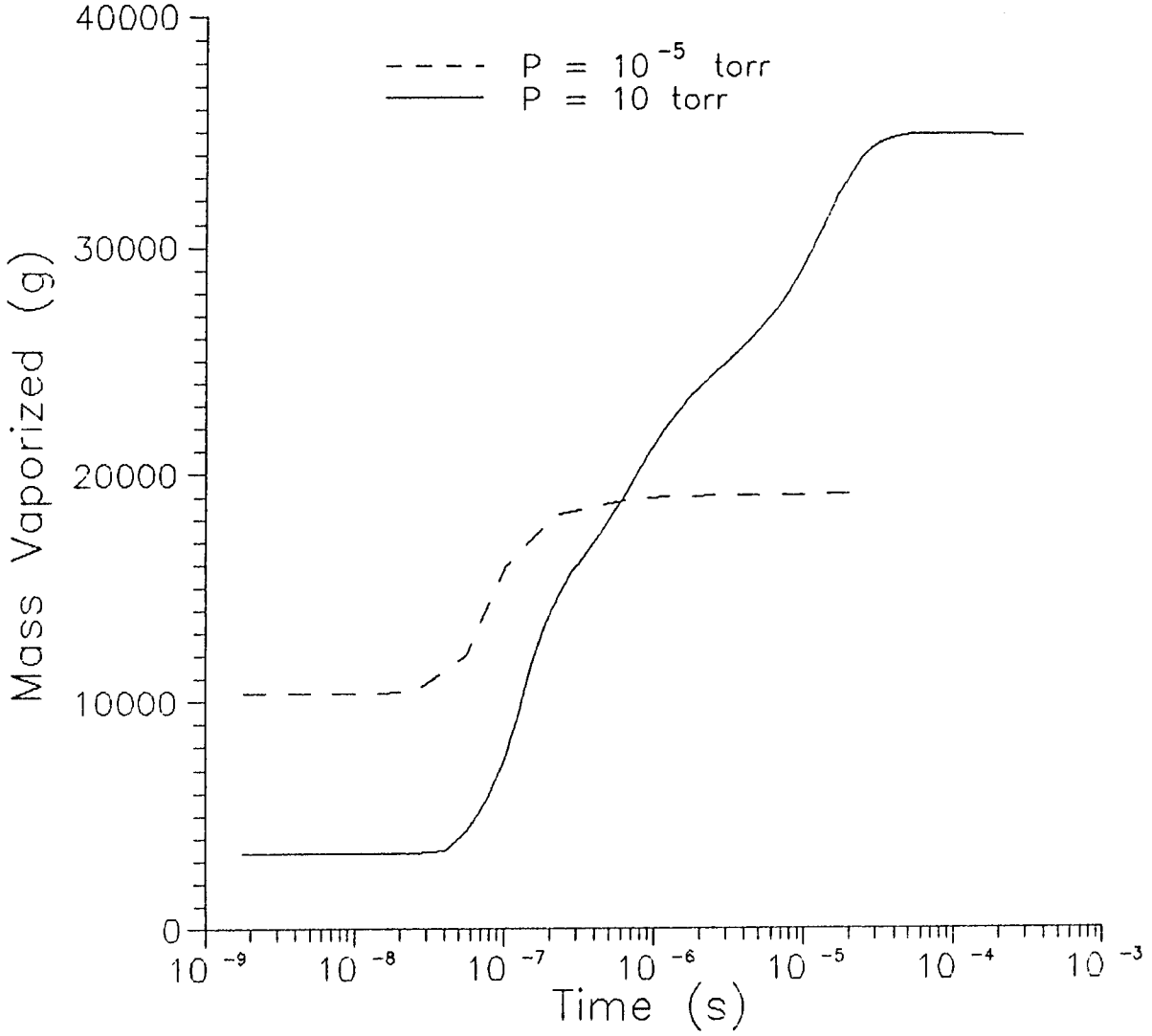

Figure 3.3. LiPb mass in the vapor phase as a function of time for calculations with initial background gas pressures of 10 torr (solid curve) and 10^{-5} torr (dashed curve).

Figure 3.4 shows the radius of the Lagrangian cells as a function of time for the 10 torr case. The simulation was run out to 0.3 seconds. The condensed region is at a radius of 3 meters from the target explosion. A region of very high vapor density exists near the wall until the vaporized material has had time to hydrodynamically respond to the pressure gradients. After ~ 0.1 ms, the LiPb is seen to move away from the interface region. Near a radius of 1 meter, a shock is seen to be pushing the argon radially outward.

The mass vaporization rate for the 10 torr calculation is shown in Fig. 3.5. The vaporization rate peaks at ~ 10^{-7} s as the radiative flux from the fireball reaches the wall. The maximum vaporization rate is ~ 10^{11} g/s. The discontinuities in the figure are an artifact of using a Lagrangian approach to modeling the vaporization. As the vapor/condensate interface moves from one Lagrangian cell to the next, an abrupt change in conditions on either side of the interface can occur. We feel, however, that because CONRAD conserves energy reasonably well, the time-integral of the vaporization rates (Fig. 3.3) should be fairly reliable.

Figure 3.6 shows the results of a similar calculation that was run out to longer times to study condensation effects. In this calculation, the background gas was 100 torr of helium. The other input parameters are identical to the previously discussed calculations. In this case, 7.2 kg of LiPb is vaporized by the hard x-rays and the maximum amount of LiPb vaporized is roughly 9.4 kg. After ~ 0.3 ms, the condensation rate exceeds the vaporization rate and the LiPb begins to condense back onto the wall. When noncondensable gas effects are neglected (solid curve), roughly 90% of the LiPb has recondensed by 10 ms so that the remaining vapor consists of ~ 99% helium by number. However, when the effects of the noncondensable He gas are considered (dashed curve), the condensation rate is seen to be dramatically

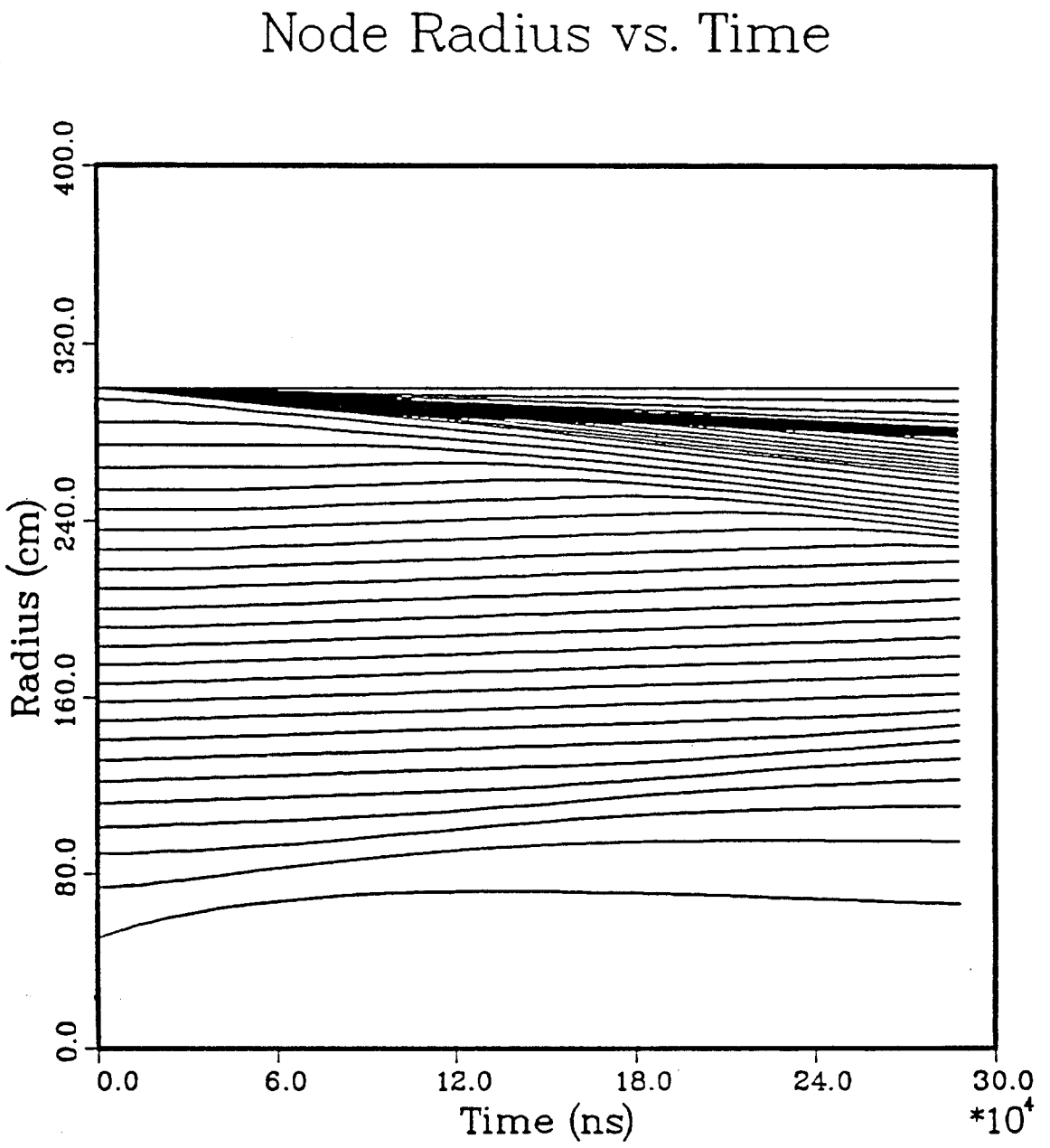

Figure 3.4. Radial positions of Lagrangian mass cells vs. time. The initial background gas pressure was 10 torr.

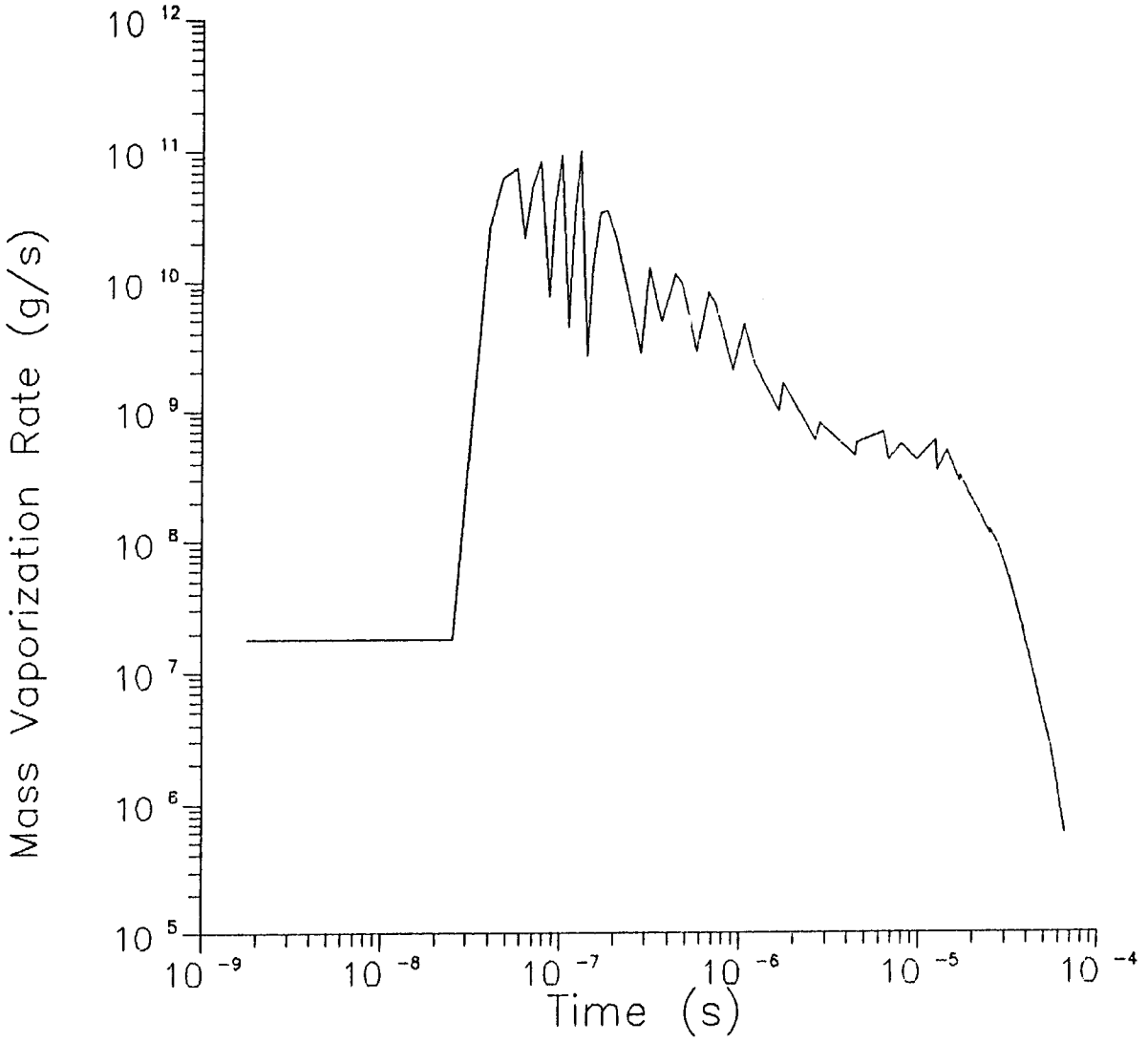

Figure 3.5. LiPb vaporization rate as a function of time.

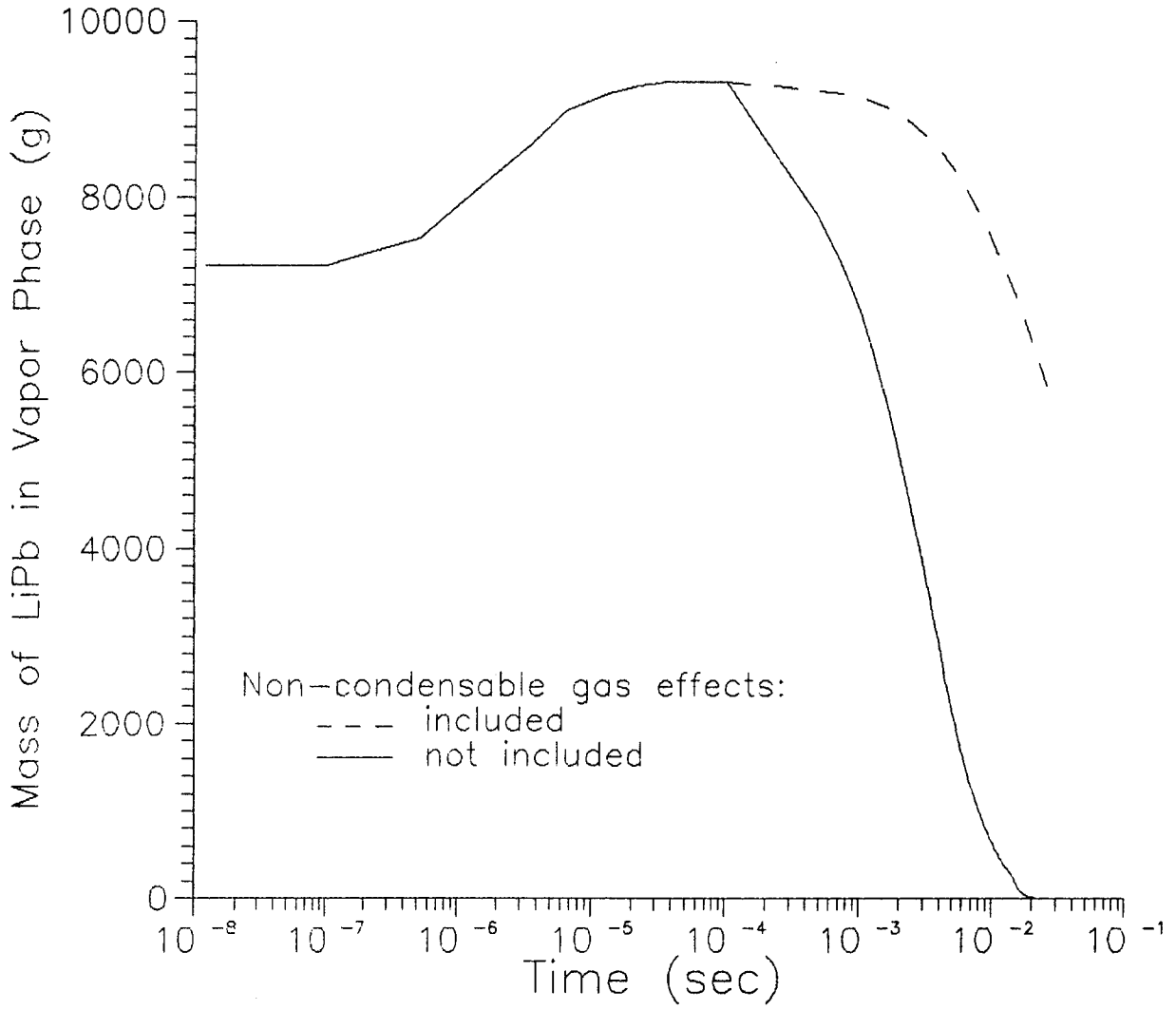

Figure 3.6. LiPb mass in the vapor phase vs. time. The initial gas pressure was 100 torr (helium). The dashed and solid curves represent results in which noncondensable were included and neglected, respectively.

slower. The influence of noncondensable gases on condensation rates is currently being studied by M. El-Afify, and results from his work will be included in CONRAD in the future.

These examples illustrate some typical results of the new vaporization/condensation model in CONRAD. Results applicable to the Laboratory Microfusion Facility are discussed in Section 5. More details on how to use the various models in CONRAD are provided in the CONRAD documentation [2].

3.2. Ion Deposition Model

In previous attempts to simulate laser-generated plasma expansion experiments carried out at the Naval Research Laboratory (NRL) [3-8], we found that the time-dependence of the debris ion charge states can play an important role in determining where their momentum and energy is deposited. This is because when energetic ions move through a high temperature plasma, free electron-ion collisions are the dominant energy transfer mechanism, and the stopping power is approximately proportional to q_1^2 (q_1 = debris ion charge state). Under certain circumstances, the energy deposition properties of ICF target debris ions may also depend sensitively upon their charge states. In our earlier simulations of the NRL experiments, we specified the ionization states of the debris ions at the beginning of each calculation, and assumed them to be constant throughout the simulation. Recently, we have modified the ion deposition model in CONRAD to compute the time-dependence of the debris ion charge states by solving the appropriate rate equations. In this section, we describe the modified ion deposition model.

Debris ions exploding from the target into the background plasma are highly ionized and have a velocity much greater than the thermal velocity of the background plasma. The mean ionization of the debris ions decreases as

they undergo ion-electron, ion-neutral, and ion-ion collisions until they eventually reach a state of equilibrium with the surrounding plasma. The rate at which ions transfer their momentum and energy to the background is calculated by the stopping power expression:

$$S = \frac{1}{N_{bg}} \left[\left(\frac{dE}{dx}\right)_{fe} + \left(\frac{dE}{dx}\right)_{be} + \left(\frac{dE}{dx}\right)_{nucl} \right] \tag{3.15}$$

where $\left(\frac{dE}{dx}\right)$ is the kinetic energy lost by a debris ion as it traverses a distance dx through a background medium of density N_{bg}. The 3 terms on the right hand side of Eq. (3.15) represent (from left to right) the contributions from collisions with free electrons, bound electrons, and nuclei of the background plasma.

The free electron contribution to the stopping power is given by [9]:

$$\left(\frac{dE}{dx}\right)_{fe} = \left(\frac{\omega_p q_1 e}{v_1}\right)^2 G(y^2) \ln \Lambda_{fe} \tag{3.16}$$

where

$$G(y^2) = \mathrm{erf}(y) - \frac{2}{\sqrt{\pi}} e^{-y^2}$$

and

$$\omega_p = \left(\frac{4\pi e^2 n_e}{m_e}\right)^{1/2}$$

is the plasma frequency. y is the ratio of the debris ion velocity v_1 to the mean electron velocity $\langle v_e \rangle$, and erf(y) is the error function. q_1 is the debris ion charge state, e is the electron charge, n_e is the electron density,

and m_e is the electron mass. The Coulomb logarithm is given by

$$\Lambda_{fe} = (0.764\ v_1)/(\omega_p b_{min})$$

where

$$b_{min} = a_o \max[q_1(\frac{v_1}{v_o})^2, \frac{v_1}{2v_o}]$$

a_o is the Bohr radius, and v_o is the Bohr velocity (= 2.2×10^8 cm/s). At high temperatures, the background plasma is highly ionized and the stopping power is dominated by the free electron term. Under these conditions, the stopping power is proportional to q_1^2.

Inelastic scattering with bound electrons and elastic nuclear scattering are important at low temperatures. The nuclear contribution can be written as [9]:

$$(\frac{dE}{dx})_{nucl} = C_1 \varepsilon^{1/2} \exp\{-45.2(C_2\varepsilon)^{0.277}\} \qquad (3.17)$$

where

$$\varepsilon = E/A_1 (MeV/amu)$$

$$C_1 = (4.14 \times 10^6\ MeV\ cm^2 g^{-1})\ \frac{\rho_2}{A_2^2}\ (\frac{A_1 A_2}{A_1 + A_2})^{3/2} (\frac{(Z_1 Z_2)^{1/2}}{Z_1^{2/3} + Z_2^{2/3}})^{3/4}$$

and

$$C_2 = (\frac{A_1 A_2}{A_1 + A_2})(Z_1 Z_2)^{-1}(Z_1^{2/3} + Z_2^{2/3})^{-1/2}\ .$$

The subscripts 1 and 2 refer to the debris ion and background plasma, respectively. A, Z, and ρ represent the atomic weight, atomic number, and mass density, respectively.

The bound electron contribution is calculated using one of two theories, depending on the debris ion velocity. Lindhard-Scharff theory [10] is valid when the debris ion velocity is small compared to the orbital velocity of the bound electrons. In this case, the bound electrons are treated as a "cloud", as opposed to point charges. The expression for the Lindhard-Scharff stopping power is:

$$\left(\frac{dE}{dx}\right)_{LS} = (3.84 \times 10^{-18}\ \text{keV cm}^{-1}) N_2 \frac{Z_1^{7/6} Z_2^*}{[Z_1^{2/3} + (Z_2^*)^{2/3}]^{3/2}} \left(\frac{E_1}{A_1}\right)^{1/2} \qquad (3.18)$$

where E_1 is the debris ion kinetic energy in keV, and Z_2^* is the average number of bound electrons per nucleus. Thus, at low velocities, the rate at which the debris ions lose their energy is proportional to their velocity. When the debris ion velocities are large compared to the electron orbital velocities, the bound electrons can be treated as point charges, and Bethe theory is used to determine the debris ion energy loss rate. The expression for the Bethe stopping power is [11]:

$$\left(\frac{dE}{dx}\right)_{Bethe} = \left(\frac{\omega_p q_1 e}{v_1}\right)^2 \left[\ln\left(\frac{2m_e v_1^2}{\langle \Phi_2 \rangle (1 - \frac{v_1^2}{c^2})}\right) - \left(\frac{v_1}{c}\right)^2\right] \qquad (3.19)$$

where $\langle \Phi_2 \rangle$ is the average ionization potential of the background plasma. To ensure a smooth transition between the 2 models, we interpolate to get the total bound electron stopping power:

$$\left(\frac{dE}{dx}\right)_{be} = \begin{cases} \left(\frac{dE}{dx}\right)_{LS} & v_1 < v_L \\ (1-f)\left(\frac{dE}{dx}\right)_{LS} + f\left(\frac{dE}{dx}\right)_{Bethe}, & v_L \le v_1 \le v_B \\ \left(\frac{dE}{dx}\right)_{Bethe} & v_1 > v_B \end{cases} \tag{3.20}$$

where $v_L = Z_1^{2/3} v_o$ and $v_B = 3 Z_1^{2/3} v_o$, and $f = (v_1 - v_L)/(v_B - v_L)$.

When the stopping ranges are comparable to or larger than the dimensions of interest (e.g., the fireball), the time-dependence of the debris ions' charge states must be computed to accurately determine the energy deposition. In CONRAD, we consider the following reactions in calculating the rate of change in the mean ionization: collisional ionization and recombination, radiative recombination, and recombination due to charge exchange with the background plasma. The debris ion ionization populations are computed by solving the coupled set of rate equations:

$$\frac{dN_q}{dt} = = N_{q-1} n_e C_{q-1} + N_{q+1} \left(n_e^2 \alpha_{q+1}^{coll} + n_e \alpha_{q+1}^{rad} + N_{bg} v_1 \sigma_{cx,q+1}\right) \tag{3.21}$$

$$- N_q \left(n_e C_q + n_e^2 \alpha_q^{coll} + n_e \alpha_q^{rad} + N_{bg} v_1 \sigma_{cx,q}\right)$$

where N_q is the number of ions in the q^{th} ionization state, N_{bg} is the background plasma number density, and $\sigma_{cx,q}$ is the charge exchange cross section. C_q α_q^{coll}, and α^{rad} represent the collisional ionization, collisional recombination, and radiative recombination rate coefficients, respectively. Expressions for these quantities are given in Section 2.2. Equation (3.21) neglects charge exchange reactions in which the debris ions increase with charge. To properly include these reactions, CONRAD would have to also track the time-dependence of the background plasma ionization populations; something

it is not currently set up to do. This can cause the debris ion charge states to fall to anomalously low values. This will be discussed in more detail below.

To calculate the charge exchange reaction rates, we use the classical cross sections given by Knudson et al. [12]:

$$\sigma_q = \pi a_o^2 q_1 \begin{cases} \frac{1}{2} Z_2^{2/3} \left[\left(\frac{\alpha v_a}{v_o}\right)^{-2} - (\beta Z_2)^{-2}\right], & v_1 < \alpha v_a \\ \frac{8}{3} \xi^{-7} \left[\left(\frac{Z_2^{2/3}}{8} \xi^7\right)^{3/5} - \left(\frac{\alpha v_a}{v_o}\right)^3\right] & \\ \quad + \frac{1}{2} Z_2^{2/3} \left[\left(\frac{Z_2^{2/3}}{8} \xi^7\right)^{-2/5} - (\beta Z_2)^{-2}\right], & \alpha v_a < v_1 < \beta Z_2 v_o \\ \frac{8}{3} \xi^{-7} \left[(\beta Z_2)^3 - \left(\frac{\alpha v_a}{v_o}\right)^3\right], & v_1 > \beta Z_2 v_o \end{cases} \tag{3.22}$$

where $\xi = q_1^{-2/7}(v_1/v_0)$, $v_a = v_o(\langle\Phi_2\rangle/13.6\ \text{eV})^{1/2}$, $\beta Z_2 = Z_2^{2/3} + \alpha v_a/v_o$, and α is an adjustable parameter.

Knudson et al. found values for α by fitting Eq. (3.22) to experimental data for ion-neutral charge exchange reactions. The selected values for α are: 0.25 for H, 0.40 for He, 0.46 for Ar, and 0.54 for Xe. Values for other atoms can be obtained by simple interpolation. Figure 3.7 compares the calculated cross sections (solid curve) with the experimental values (symbols) for charge exchange reactions between highly charged ions and neutral argon. Here, the scaled cross sections are plotted as a function of the scaled kinetic energy of the projectile ions. The agreement between the calculated and experimental cross sections is reasonably good, suggesting the scaling laws used by Knudson et al. is reliable for a wide range of projectile ions.

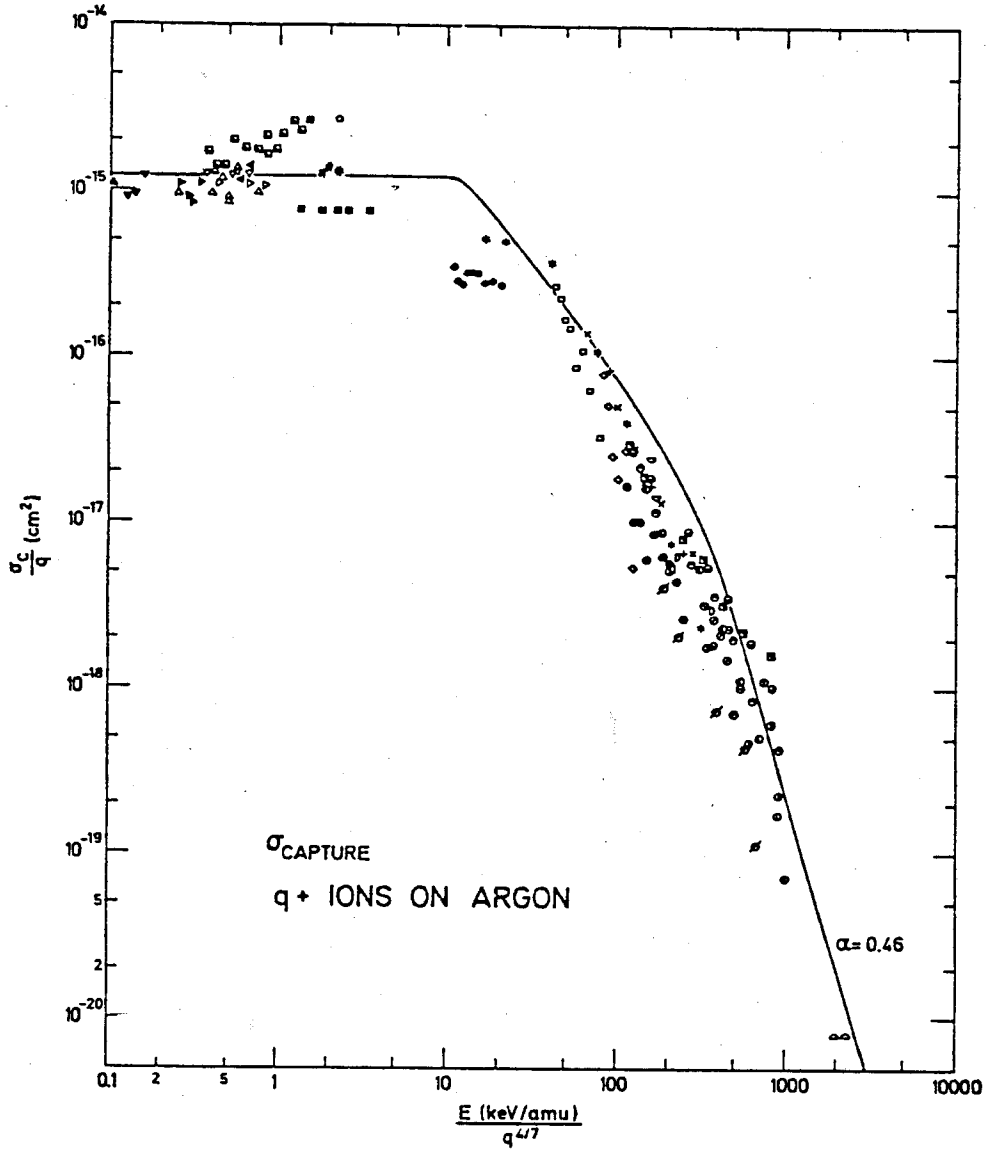

Figure 3.7. Calculated (solid curve) and experimental charge exchange cross sections vs. scaled energy for highly charged ions on neutral argon.

When the background plasma is ionized, the charge exchange cross sections decrease dramatically when the debris ion kinetic energy is not large enough to overcome the Coulomb repulsion energy. To model this effect, we use a low velocity cutoff for the cross sections of ion-ion charge exchange reactions that is based on the results of calculations by Hyman et al. [13]. The cutoff velocity is given by:

$$v_{crit} = 6 \times 10^5 \text{ cm/s } q^{2/7} \ (\Phi_2/13.6) \tag{3.23}$$

When the background plasma is ionized and the debris ion velocity is less than the cutoff velocity, the charge exchange cross section is zero in CONRAD; otherwise, we use the Knudson values. Figure 3.8 shows the charge exchange cross section for Al ions moving through a nitrogen background plasma as a function of the Al ion velocity ("z" in Fig. 3.8 refers to the charge state of the Al ions). The solid curve was computed using Eq. (3.22) and the data points represent the calculations by Hyman et al. At scaled velocities below 6×10^5 cm/s, the cross sections decrease rapidly due to Coulomb repulsion. Above the cutoff velocity, the Hyman cross sections are up to a factor of 4 larger than the Knudson cross sections. Because of the lack of experimental data for charge exchange reactions between highly charged ions, we cannot predict with confidence the accuracy of either curve. Rather, Figs. 3.7 and 3.8 give an indication of the range of uncertainty in the charge exchange cross sections that are used in CONRAD, which seems to be a factor of ~ a few.

Next, we present results of numerical calculations which illustrate some of the features of the revised ion deposition model. We have simulated NRL plasma expansion experiments with a relatively low background gas density so that the results would be sensitive to temporal changes in the debris ion

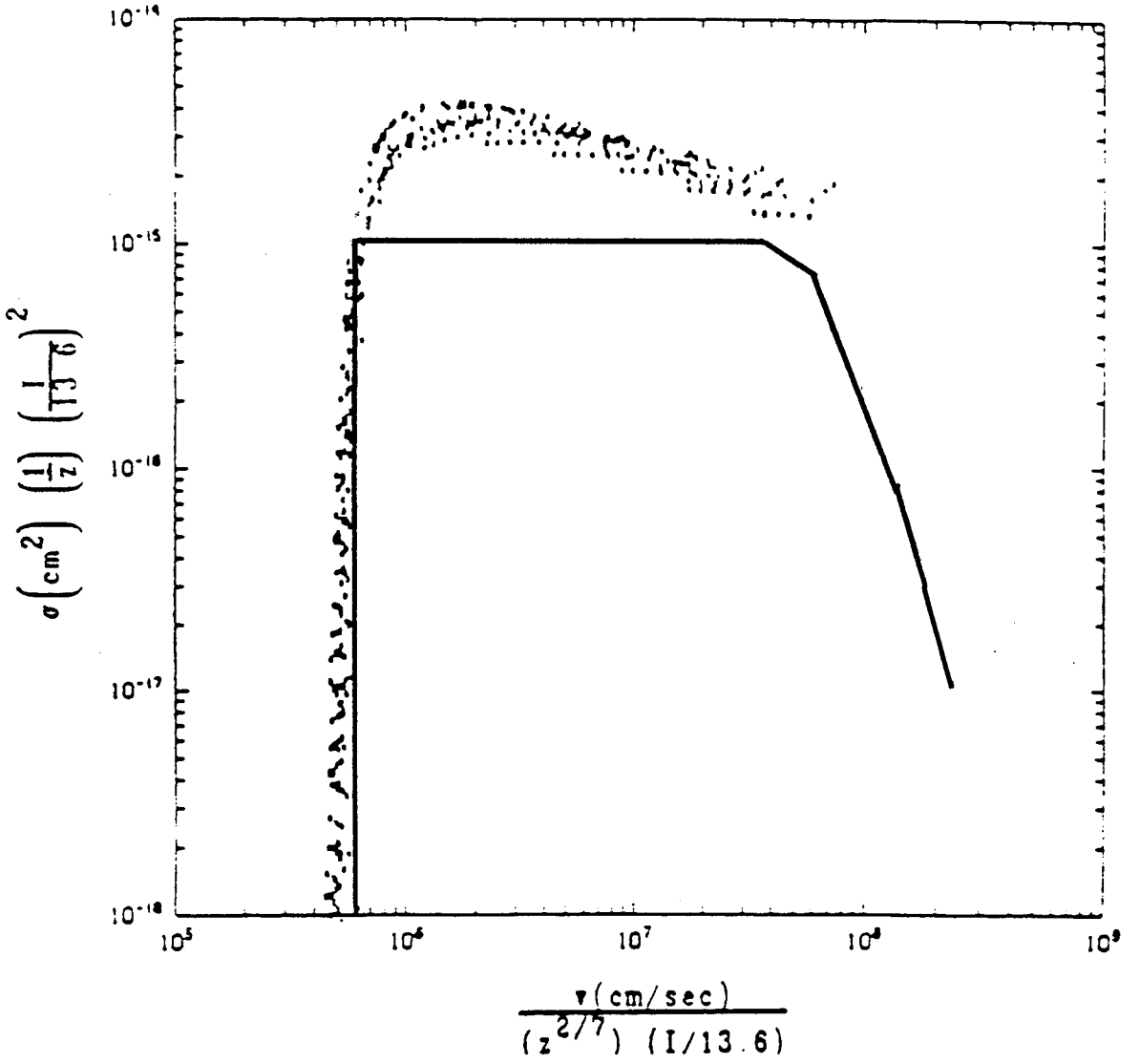

Figure 3.8. Comparison of charge exchange cross sections calculated using Eqs. (3.22) and (3.23) (solid curve) and those computed by Ref. [13].

charge states. To briefly review the NRL experiments, a solid planar aluminum target was illuminated by an intense laser pulse (~ 10^{12} W/cm^2 with pulse width ~ 5 ns), producing an explosion of highly charged Al ions with velocities ~ 5 x 10^2 cm/s. The Al ions transfer energy and momentum to the surrounding nitrogen gas, heating the gas to ~ 10^2 eV. The Al ions, which are fully ionized as they leave the target, undergo charge-exchange and electron-capture reactions as they speed through the background gas, thereby decreasing in charge as they travel through the gas. The location of the shock front as it evolved was monitored using both dark-field shadowgraphy and framing photography. In addition, spectroscopic observations were made to estimate the temperature, density, and charge state of the plasma.

The initial background gas pressure for the simulations discussed below was varied between 0.025 and 0.3 torr. Data also exists for 1.5 and 5 torr experiments, but our results are rather insensitive to the details of the ion deposition model. The total debris ion energy expanding into 4π steradians was 150 J. The x-ray energy emitted from the target in the experiments was small, and therefore neglected in our calculations. Thermal radiation was transported in 20 frequency groups using the flux-limited radiation diffusion model. The equation of state and radiative properties of the background plasma were supplied by the IONMIX code [14].

The debris ions were divided into a large number of groups to approximate their continuous emission (in time and energy) from the target. The ions were grouped into 10 velocity bins, with the distribution shown in Fig. 3.9. Each velocity group was subdivided into 10 groups that were emitted from the target at 10 times over a period of 5 ns. Thus, there were a total of 100 different ion "bunches" tracked throughout the calculations. The debris ions were fully ionized (Al^{3+}) as they left the target. CONRAD tracks the ionization

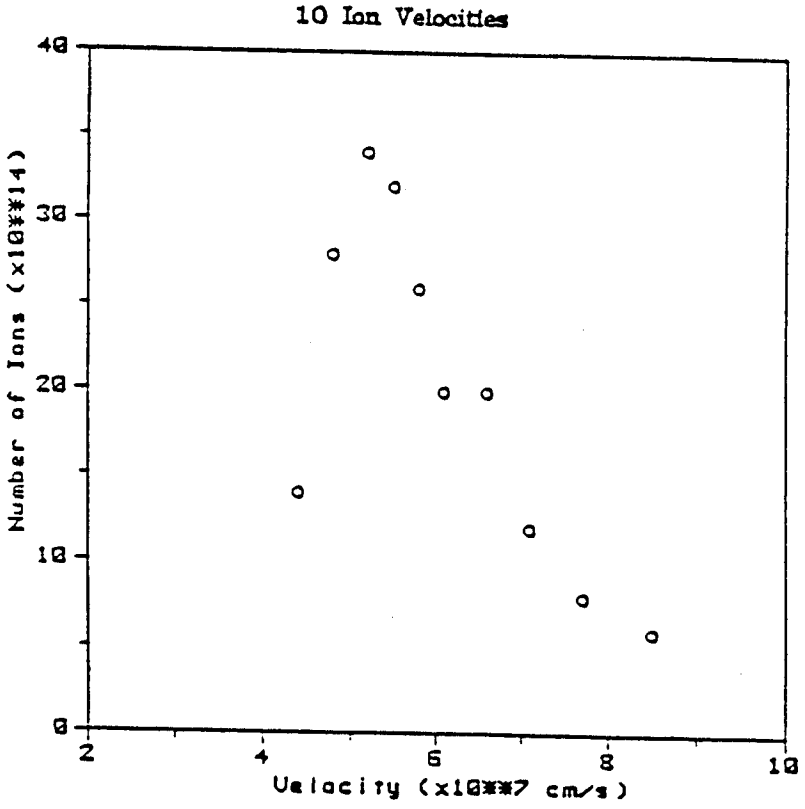

Figure 3.9. Initial Al debris ion velocity distribution for CONRAD simulations of the NRL experiments.

populations for each ion bunch, and uses the mean ionization of each bunch to calculate the stopping power.

Results from our calculations are shown in Figs. 3.10 through 3.13. Figure 3.10 shows the average charge state for the lowest, middle, and highest energy groups as a function of distance from the target for the 0.1 torr calculation. The initial kinetic energies for the 3 groups are 27, 47, and 102 keV/particle. The curve representing the highest energy group is on the left, while that for the lowest energy group is on the right. The letters near each point refer to the corresponding simulation times. For example, the ion bunch that left the target with an initial energy of 47 keV/particle reached a radius of 2.3 cm at 43 ns and had a mean charge state of 7.6. A "snapshot" in time can be obtained by drawing a curve between symbols with the same letter. At early times, all ion bunches are near the target and are essentially fully ionized.

Figure 3.10 shows that the average ionization state of the highest energy group drops most rapidly, attaining a charge state of ~ 1 by 17 ns. By comparison, the lowest energy group is still very highly ionized ($\langle Z \rangle \sim 12$) at 17 ns. The reason this occurs is because the charge exchange reaction rates, which are the dominant recombination mechanism in Eq. (3.21), are higher for the faster ions. The reasons for this are: (1) the faster ions see more collisions with neutral particles and hence are less affected by Coulomb repulsion; (2) the slower ions see fewer background gas particles per unit time because their velocity is lower; and (3) the slower ions move through material that was previously heated, which increases the cutoff velocity for ion-ion reactions and also increases the collision ionization rates. Figure 3.10 shows that at any given time, the mean charge state of the debris ions decreases with distance from the target. Similar conclusions were reached by Guilliani et al. in separate calculations [15,16].

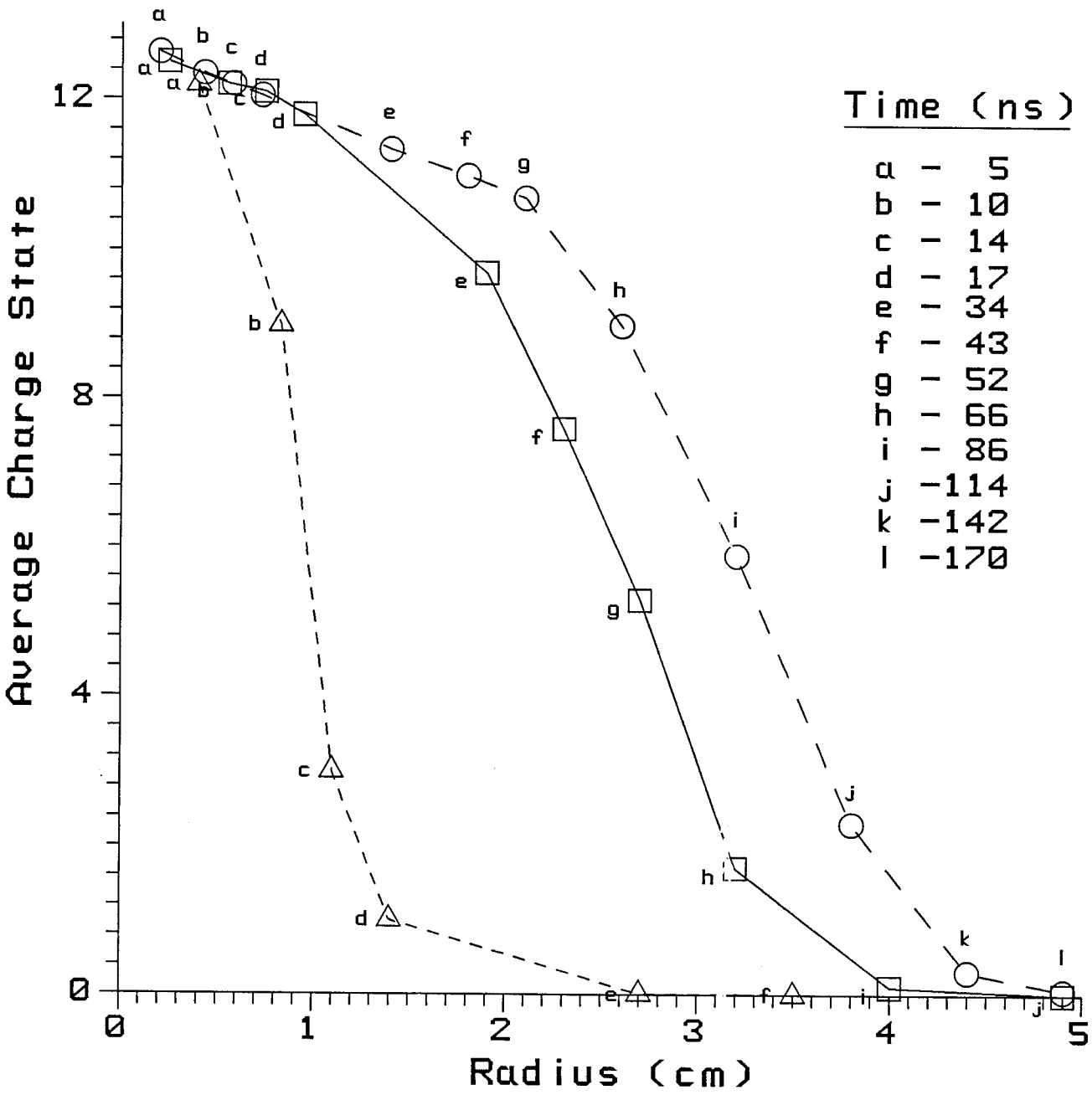

Figure 3.10. Average ionization state of the lowest, middle, and highest (right to left) ion energy groups as a function of position and time.

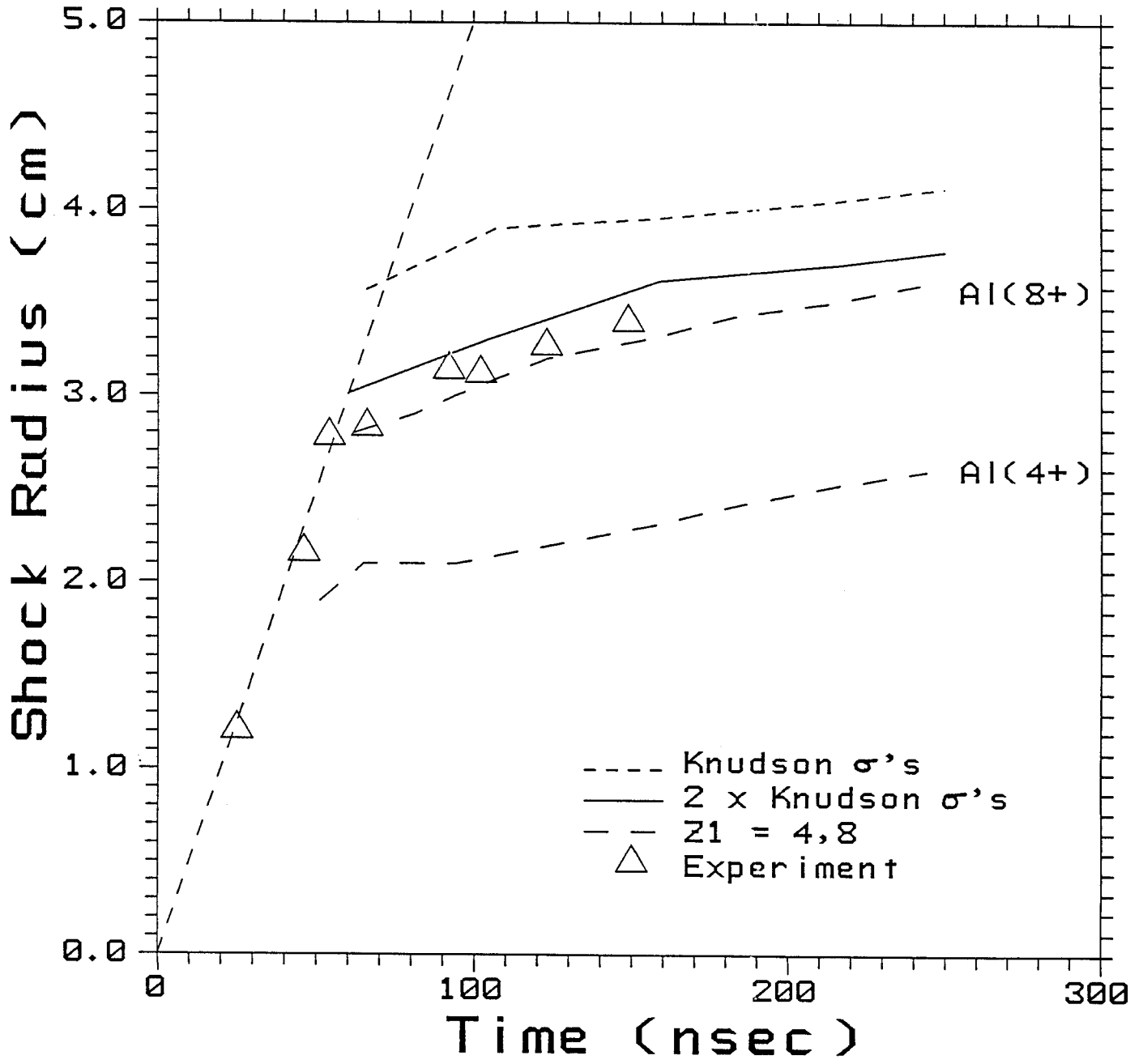

Figure 3.11. Shock radius vs. time for 0.025 torr calculations using the Knudson (Eq. (22)) cross sections (short dashed curve), twice the Knudson values (solid curve), and constant change states of Al^{4+} and Al^{8+} (dashed curves). The experimental data are represented by the open triangles.

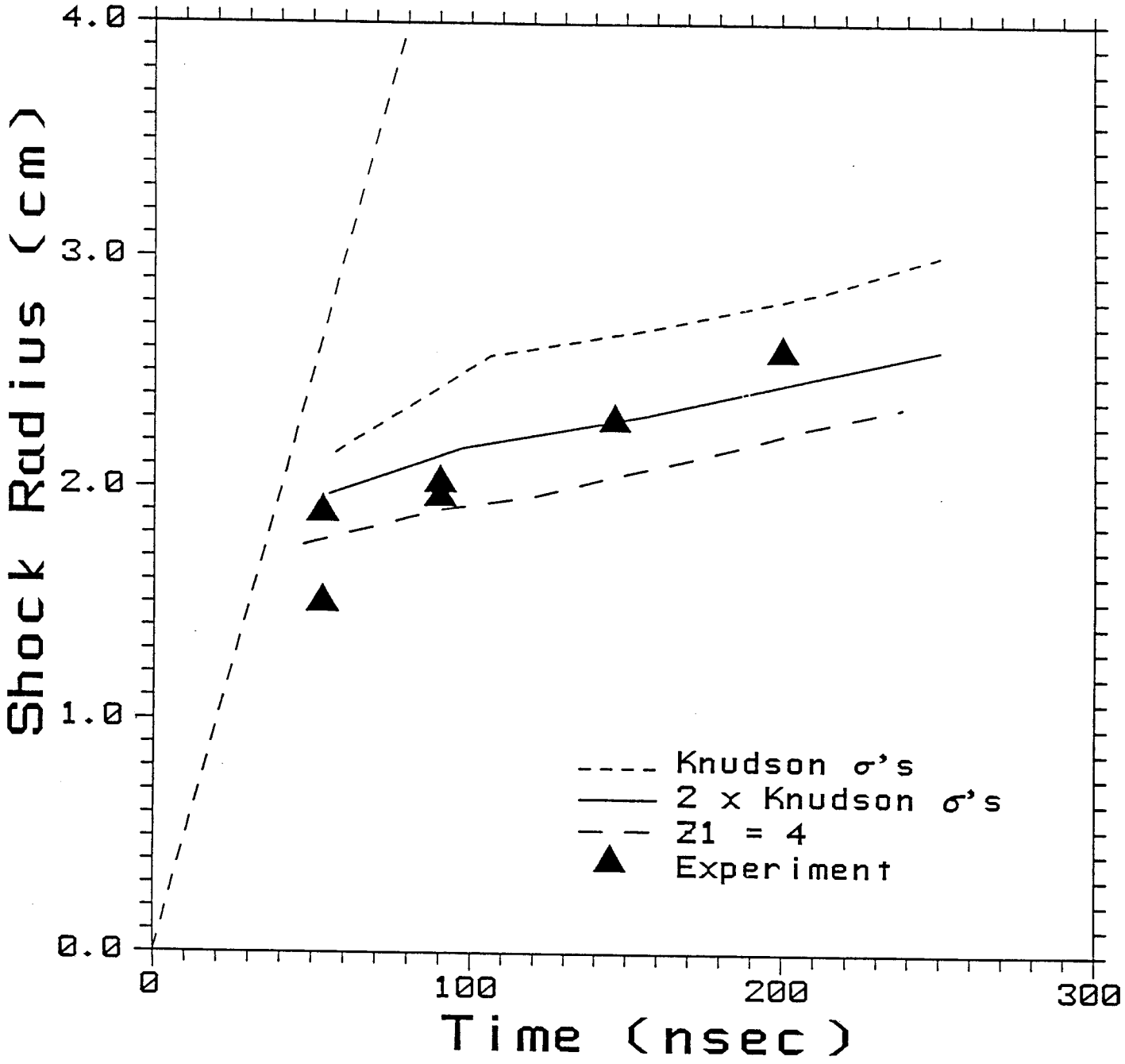

Figure 3.12. Shock radius vs. time for 0.1 torr calculations using the Knudson cross sections (short dashed curve), twice the Knudson values (solid curve), and a constant change state of Al^{4+} (long dashed curve). The experimental data are represented by the solid triangles.

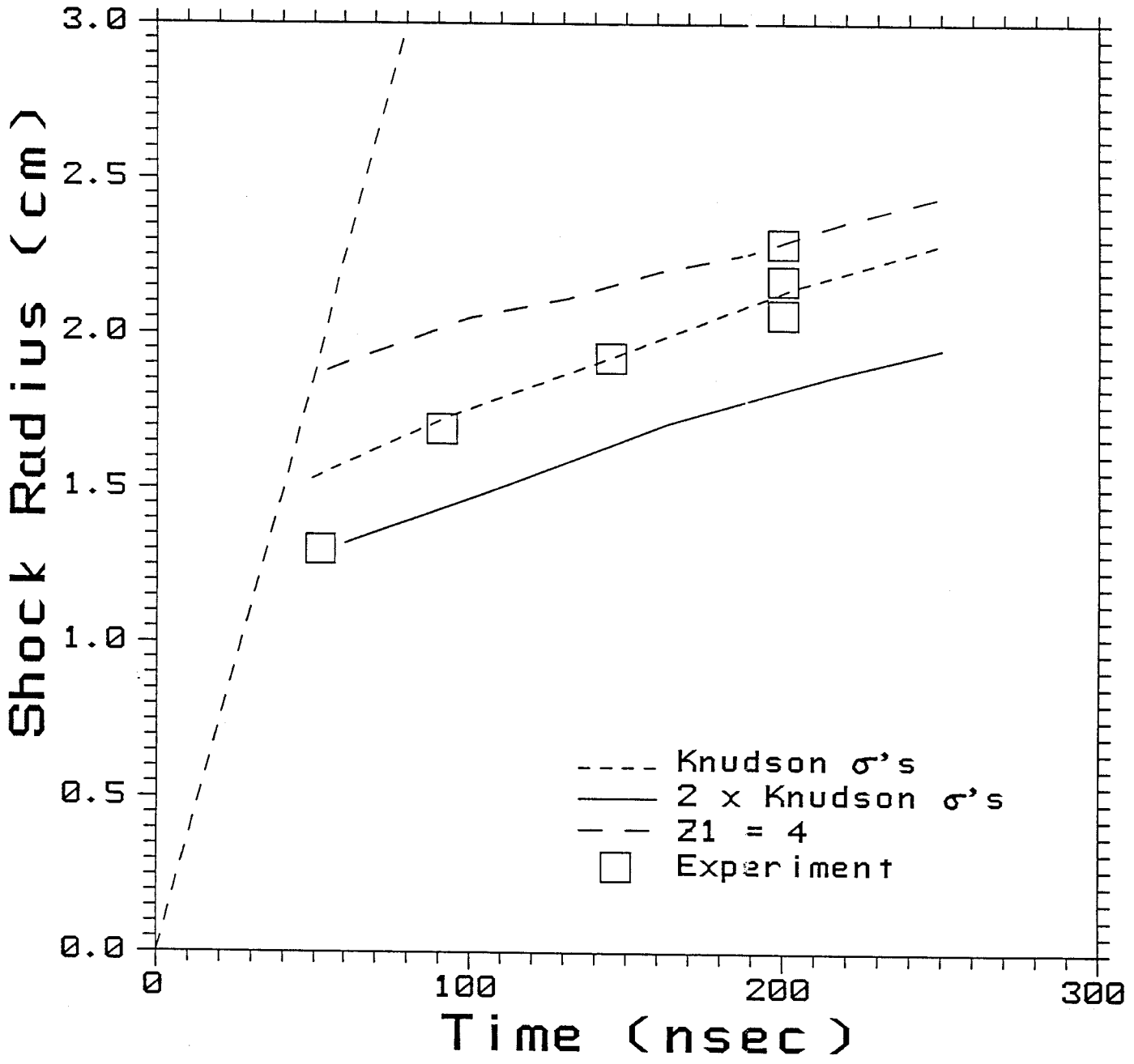

Figure 3.13. Shock radius vs. time for 0.3 torr calculations using the Knudson cross sections (short dashed curve), twice the Knudson values (solid curve), and a constant change state of Al^{4+} (long dashed curve). The experimental data are represented by the open squares.

The Al ion charge states fall to erroneously low values at late times because charge exchange reactions in which the Al ions lose electrons are ignored. That is, the charge exchange model in CONRAD does not conserve electrons. The reason for this is that in CONRAD, the ionization state of the background plasma depends only on the local density and temperature, and is independent of the charge exchange reaction rates. Physically, the background plasma must give up electrons as it undergoes charge exchange reactions with the debris ions. As the nitrogen becomes more highly ionized and the Al less ionized, reactions in which Al loses electrons will proceed faster. By ignoring this effect, the charge states of the debris ions can fall to near zero. However, since most of the energy deposition occurs while the debris ions are highly ionized, this is not expected to significantly affect the properties of the microfireball or blast wave.

The calculated shock radii are compared with experimental data in Figs. 3.11, 3.12, and 3.13 for the 0.025, 0.1, and 0.3 torr calculations, respectively. The experimental data are represented by the triangles or squares, and the dashed line going through the origin corresponds to the mean velocity of the debris ions. The shock radii computed using the Knudson charge exchange cross sections are represented by the short dashed lines in each figure. The computed shock radii are found to be only slightly greater (~ 10-20%) than the experimental values for the 0.025 and 0.1 torr cases, and are in very good agreement with the 0.3 torr experimental data. This agreement is quite good considering the uncertainties in the charge exchange cross sections. The calculated shock radii for the 0.025 and 0.1 torr cases are found to be in better agreement with the experimental data when the cross sections are increased by a factor of 2 (solid curves). The shock radii decrease in this instance because the mean charge states of the Al ions, and

hence the energy deposition rate, are lower. Also shown in each figure are curves from previous calculations in which the debris ions were assumed to have constant values of 4 or 8. In Fig. 3.11, it is seen that using a different charge state can significantly change the results, particularly at low background gas densities [17]. These results show that given the uncertainties in the charge exchange cross sections, the improved ion energy deposition model is able to reproduce available experimental data quite well.

To summarize, we have improved the ion deposition model in CONRAD so that the evolution of the debris ion charge states is computed using physically plausible models. Agreement between experimental blast wave data and the CONRAD calculation is good, suggesting the ion deposition model is reliable. In addition, our calculations indicate the mean charge state of the debris ions exploding from the target should generally decrease with increasing distance from the explosion. This effect could potentially be observed in target explosions within the Laboratory Microfusion Facility.

References for Section 3

[1] D.A. Labuntsov and A.P. Kryukov, Int. J. Heat Mass Transfer 22 (1979) 989.

[2] R.R. Peterson, J.J. MacFarlane, and G.A. Moses, University of Wisconsin Fusion Technology Institute Report UWFDM-670, revised (1988).

[3] B.H. Ripin, A.W. Ali, H.R. Griem, J. Grun, S.T. Kacenjar, C.K. Manka, E.A. McClean, A.N. Mostovych, S.P. Obenschain and J.A. Stamper, in Laser Interaction and Related Plasma Phenomena, Vol. 7, edited by G. Miley and H. Hora (Plenum, New York, 1986), pp. 857-877.

[4] B.H. Ripin, J.A. Stamper and E.A. McClean, NRL Memorandum Report 5279, Naval Research Laboratory, Washington, D.C. (1984).

[5] E.A. McClean, J.A. Stamper, H.R. Griem, A.W. Ali, B.H. Ripin and C.K. Manka, NRL Memorandum Report 5274, Naval Research Laboratory, Washington, D.C. (1984).

[6] B.H. Ripin, E.A. McClean, J.A. Stamper, J. Grun, C.K. Manka and A.N. Mostovych, ETHANL, Issue #7, p. 75, SRI International, Menlo Park, CA (1987).

[7] A.W. Ali and E.A. McClean, J. Quant. Spectrosc. Radiat. Transfer 33, 381 (1985).

[8] E.A. McClean, B.H. Ripin, A.W. Ali, H.R. Griem, J. Grun, C.K. Manka, A.N. Mostovych, S.P. Obenschain and J.A. Stamper, ETHANL, Issue #7, p. 20, SRI International, Menlo Park, CA (1987).

[9] T.A. Melhorn, J. Appl. Phys. 52 (1981) 6522.

[10] J. Lindhard and M. Scharff, Phys. Rev. 124 (1961) 128.

[11] J.D. Jackson, Classical Electrodynamics, 2nd Edition (Wiley, New York, 1975).

[12] H. Knudson, H.K. Hangen, and P. Hvelplund, Phys. Rev. A23 (1981) 597.

[13] E. Hyman, M. Mulbrandon, and J. Giuliani, ETHANOL, Issue #8, p. 281, SRI International, Menlo Park, CA (1987).

[14] J.J. MacFarlane, University of Wisconsin Fusion Technology Institute Report UWFDM-750 (1987), submitted to Comput. Phys. Commun.

[15] J. Giulliani, Bull. Amer. Phys. Soc. 32 (1987) 1801.

[16] J. Giulliani, private communication, 1988.

[17] R.R. Peterson, J.J. MacFarlane, G.A. Moses, M. El-Afify and M.L. Corradini, University of Wisconsin Fusion Technology Institute Report UWFDM-723 (1987).

4. LIQUID METAL CONDENSATION EXPERIMENT

4.1 Introduction

Many of the conceptual Inertial Confinement Fusion (ICF) designs which have been previously developed by many groups utilize the vaporization and condensation of liquid metals for protection of the first wall of the ICF reaction chamber and/or for heat transport and power conversion. The condensation of liquid metal vapor from the reaction chamber atmosphere, in particular, has been estimated to be one of the constraining factors limiting the allowable repetition rate in reactor applications [1]. Up until now, little in the way of experimental data has been available for verification of theoretical models.

The Liquid Metal Condensation Experiment (LMCE) was undertaken in an effort to generate condensation data on a small scale under conditions generally similar to those which might be found in an ICF reactor cavity. A feasibility study of a conceptual design for the experiment was performed in the previous year [2]. During the current year, the capacitive discharge system (CDS) was set up and tested, a set of diagnostics was developed, and several preliminary runs were made. The next section reviews the conceptual design of the experiment including several changes which were made during the past year. The following sections discuss the progress that was made on the CDS and diagnostics and the work anticipated in the coming year.

4.2 Changes in Conceptual Design of LMCE

The objective of the LMCE is to experimentally estimate the condensation rate under conditions similar to those in an ICF reactor cavity. The conditions which were used to develop the conceptual design are given in Table 4.1. These were chosen to correspond to the cavity conditions computed for the

Table 4.1. Parameter Comparison

HIBALL Reactor Design [3]	
Maximum initial vapor temperature	4500 K
Final vapor pressure	0.01 torr
Final vapor temperature	800 K
Chamber geometry	cylindrical 5 m radius
Vaporized mass	18 kg
Conceptual Experimental Design [2]	
Maximum initial vapor temperature	3500-4500 K
Final vapor pressure	0.01 torr
Final vapor temperature	800 K
Chamber geometry	cylindrical 30 cm radius
Vaporized mass	4 g

HIBALL reactor design [3]. Due to the difference in scale between the experiment and the ICF reactor, it was expected that the experimental results would not be directly applicable to the reactor case but would provide data with which to verify theoretical models. These would in turn be applied to the reactor case. Therefore, although the cavity conditions may vary fairly widely depending on the particular ICF reactor design which is considered, the selection of a particular set of experimental parameters is less critical.

The original conceptual design of the LMCE [2] utilized a cylindrical chamber in which a sample of the metal is inserted in the form of a coating on a tungsten wire. A capacitive discharge system is used to vaporize the metal on a millisecond time scale. The vaporized metal would then condense onto the chamber walls over an estimated 10-20 milliseconds. The chamber pressure over the course of the transient would be recorded and the condensation rate computed.

During the past year several refinements in the design concept have been made as problems with the details of the design become evident. The original proposed experiment was to use the $Li_{17}Pb_{83}$ alloy as the vaporizing and condensing metal. There are a number of difficulties inherent in using a fairly exotic and reactive metal such as $Li_{17}Pb_{83}$. The metal must first be procured in the form of a coating on a tungsten wire. A few simple experiments were performed to investigate the local manufacture of a coated wire without success. We have contacted several companies regarding this and none of them have expressed an interest in manufacturing a coated wire of this type either. We then proposed abandoning the tungsten wire core and using a solid wire made of $Li_{17}Pb_{83}$. It was hoped that this material might be easier to procure from the laboratories currently working with $Li_{17}Pb_{83}$.

Further considerations of the experimental chamber design were also complicated by the anticipated use of $Li_{17}Pb_{83}$. Due to the reactivity of the metal, it must be kept in an inert environment to prevent contamination by air or moisture. The most straightforward method of handling such a material would be to use an inerted glove box of some type. Due to the size of the experimental chamber and diagnostics, however, any such glove box would be extremely large and expensive. Less costly methods of limiting contamination might be possible, but would probably greatly complicate the experimental procedure and would also most likely allow some contamination to take place.

For these reasons, we proposed abandoning the use of $Li_{17}Pb_{83}$ and utilizing plain Pb wires instead. LLNL concurred with this change at the February review meeting. We have noted, however, that the use of $Li_{17}Pb_{83}$ or another binary metal alloy might be of important interest to LLNL and may be worth consideration for a future investigation. We have chosen to continue to work with solid wires rather than with coatings on tungsten wires.

A second materials problem was also encountered. The original design called for the use of a SiC-laminated stainless steel wall [2]. It was believed that rectangular panels of this material were commercially available and could be welded into a prismatic cylindrical chamber. Further review indicated that a stainless steel chamber would be simpler and cheaper to construct.

Another change in the design concept involved the pressure diagnostic. Initially a fast response capacitance vacuum gauge was to be used to measure the pressure history in the chamber over the course of the transient. Significant doubts were expressed by both UW and LLNL staff regarding the accuracy and robustness of this technique. At the suggestion of LLNL, we investigated laser diagnostic techniques. The review indicated that a laser

Rayleigh scattering system would provide a more accurate measure of the vapor density in the experimental chamber. In addition, some of the components for such a system were already available in our laboratory. For these reasons, the laser scattering system was adopted as the primary vapor density diagnostic.

4.3. Test Chambers and Miscellaneous Equipment

Two test chambers have been used up until now in the experiments. The first one was a simple acrylic cylinder which was used in the testing of the modified CDS. The chamber was 150 mm in diameter and 450 mm long. A second chamber was needed to develop and test the diagnostics. For this chamber, a Pyrex cross with a 150 mm ID and an overall length of about 450 mm across was used. The configuration of the Pyrex chamber is shown in Fig. 4.1.

A small mechanical vacuum pump has been used in the preliminary testing of the experiment. Although the pump has worked well thus far, the manufacturer's guaranteed blankoff pressure is 15 millitorr. The initial experimental parameters called for pressures of about 10 millitorr. For this reason, we are changing to a slightly larger vacuum pump with a blankoff pressure of 0.1 millitorr.

In order to determine the conditions in the chamber prior to the triggering of the discharge, a vacuum gauge is needed. We were initially using a portable handheld thermocouple gauge borrowed from another lab. A Granville-Phillips Convectron gauge with digital readout has been purchased and will be installed soon. The gauge tube is isolated from the chamber by a valve during the shot to protect it from condensing vapor.

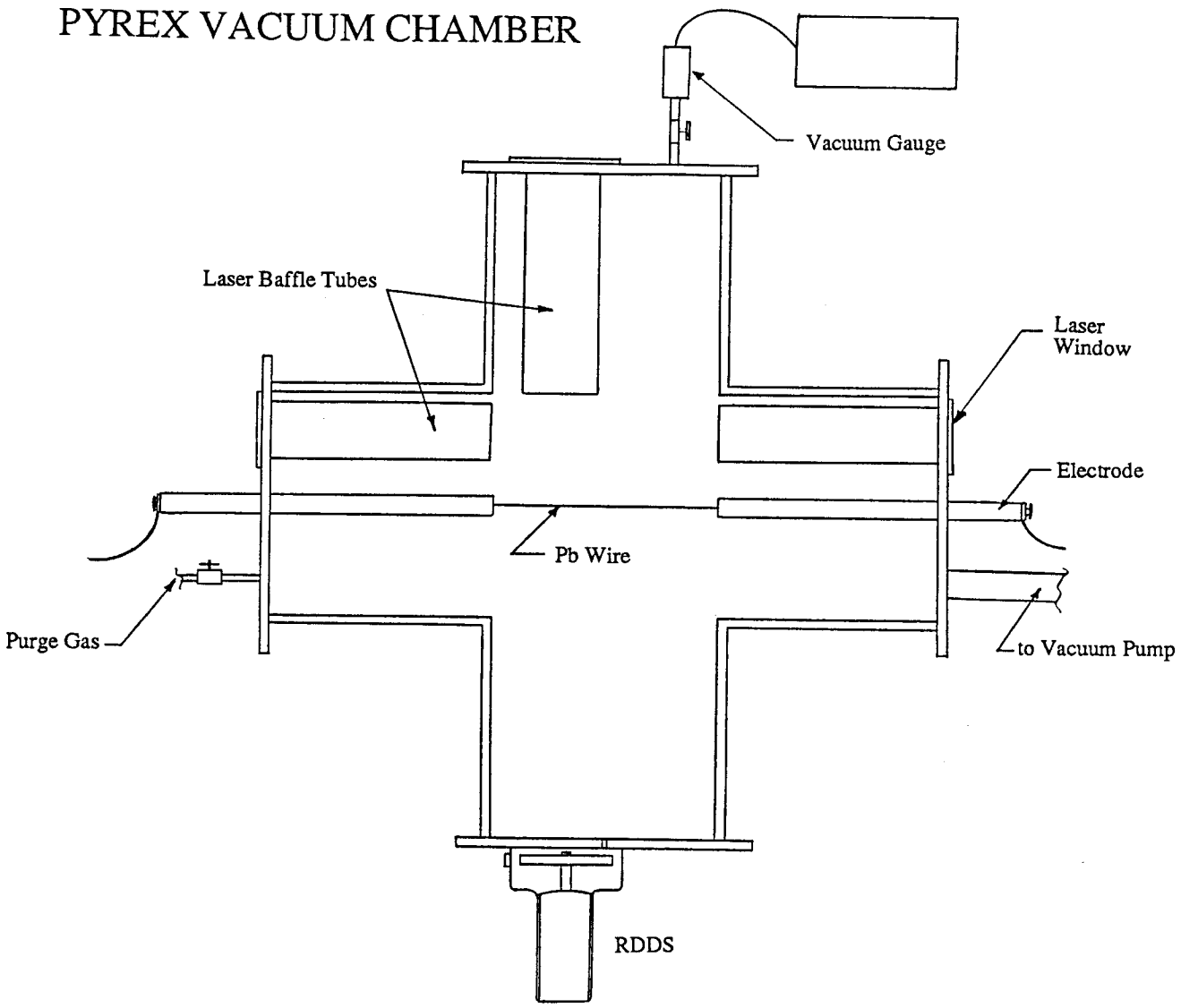

Figure 4.1 Pyrex experimental chamber.

4.4. Capacitive Discharge System

The CDS is used to vaporize the metal wire by delivering a large quantity of energy, of the order of kilojoules, to the wire in about a millisecond. A spare CDS was borrowed from the Phaedrus plasma physics laboratory at the UW, but required several modifications for our purposes. The CDS was originally set up to deliver a long, square pulse and had to be rearranged to allow it to vaporize the wire in as short a time as possible. The current operating parameters of the CDS are listed in Table 4.2.

A timing and triggering circuit was fabricated to allow the length of the discharge and the amount of energy dumped into the wire to be controlled. When the trigger button is pressed, a start trigger pulse is sent to the CDS where it begins the discharge. After a predetermined time period that may be varied from 200-1400 microseconds, a stop trigger pulse is sent to the CDS which terminates the discharge. The start trigger is also used to trigger the data acquisition system.

The temperature of the metal vapor is estimated by measuring the energy input to the wire. The voltage across the wire is determined using a voltage divider. A Rogowsky coil is used to measure the current. The two signals are recorded on the data acquisition system. The power and energy are subsequently calculated on the computer.

4.5 Rotating Disk Deposition System

One of the primary parameters of interest in the experiment is a measure of the time history of the metal vapor pressure. A strongly related variable is the condensation mass flux. The rotating disk deposition system (RDDS) diagnostic was developed to provide a measure of the condensation mass flux. The system, pictured in Fig. 4.2, consists of a rotating disk on which a set

Table 4.2. CDS Parameters

Capacitance	500 μF
Inductance	35 nH
Internal resistance	0.128 ohms
Maximum voltage	5 kV

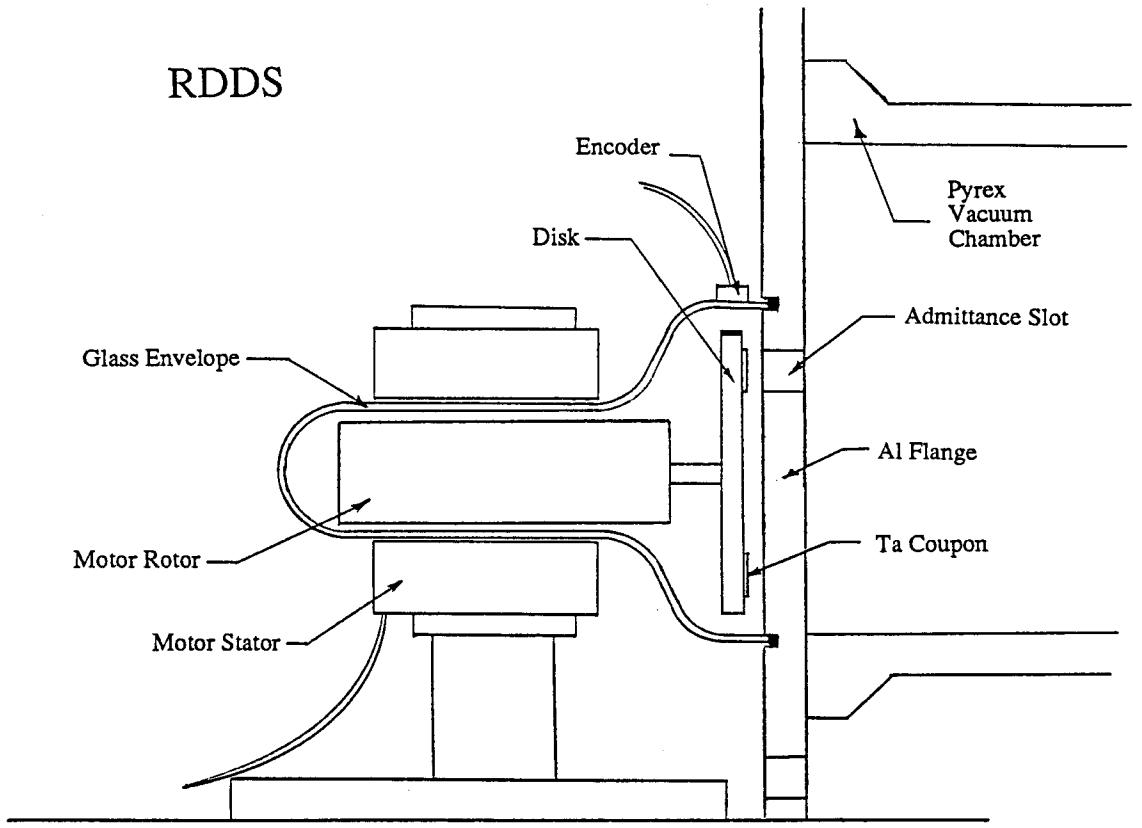

Figure 4.2. Rotating Disk Deposition System (RDDS) for measuring condensation mass flux.

of coupons is fixed. The coupons are exposed to the condensation flux as they are rotated past a slot. Following a test, the coupons are analyzed for the amount of condensed metal which has been deposited on each. Knowing the position of the coupons and the rotational speed of the disk, the condensation mass flux as a function of time can then be estimated.

One of the primary problems involved in applying this measurement technique is quantitatively analyzing the coupons for the mass of the condensed metal. A number of analysis methods for lead were reviewed, both chemical and nuclear. None appeared to be simple and amenable to our local resources. For this reason, we have elected to send our coupons to a commercial chemical analysis laboratory. Unfortunately, the techniques which they must use are labor-intensive, hence costly. Therefore we will be quite limited in the number of coupons that we will be able to analyze. If the RDDS proves to be particularly useful, further exploration into setting up our own local analysis capability might be warranted.

The primary component of the RDDS is a modified x-ray tube. The rotor of the electric motor is positioned inside the glass envelope and is magnetically coupled to the stator which is fixed around the outside. The top of the x-ray tube was cut off and the edge was ground flat and fire-polished. This provides a simple and effective vacuum seal to the chamber flange. The disk containing the coupons is attached to the rotor shaft. Due to the very low resistance of the motor bearings, the disk is made of copper so that an adjustable external magnet may be used to generate a drag force. Speed is controlled by changing the position of the magnet and by varying the input power to the motor with a variac.

It is necessary to determine the rotational speed and position of the disk in order to fix the time of each coupon's exposure. An encoder using an

infrared photodiode and phototransitor was constructed which generates a TTL pulse each time a dark band on the edge of the disk passes by. The pulse train from the encoder is currently recorded by the data acquisition system. The time to the first pulse and the time interval between consecutive pulses then determine the rotational speed and position at the time of the start trigger. If the RDDS proves successful, the triggering circuit may be modified so that the start trigger is generated at the encoder pulse. This would allow coupons to be concentrated at a specific position of interest on the disk rather than being uniformly distributed. In addition, a digital tachometer readout may be added for convenience.

The RDDS has been successfully tested operationally. The speed control and encoder work well. Unfortunately, in the experiments to date little of the metal vapor has reached the extreme ends of the cross. Hence, there has been little condensation on the disk and coupons. Due to the expense of the coupon analysis, none of the coupons has been analyzed. It is believed that the reason for the localization of the metal vapor and condensation in the central region of the chamber is that a relatively soft vacuum has been used. The large noncondensable gas presence has probably impeded the flow of the vapor to the far regions of the chamber.

4.6 Laser Density Diagnostic

A laser Rayleigh scattering system is to be used to record the metal vapor density as a function of time during the experiment. The system is pictured in Fig 4.3. A 15 mW HeNe laser that was available in our laboratory is used as the light source. The beam is expanded and then focused on a point about 36 mm to the side and about 22 mm below the centerline of the chamber. The scattered light is collected at a 90 degree angle. The scattered photons

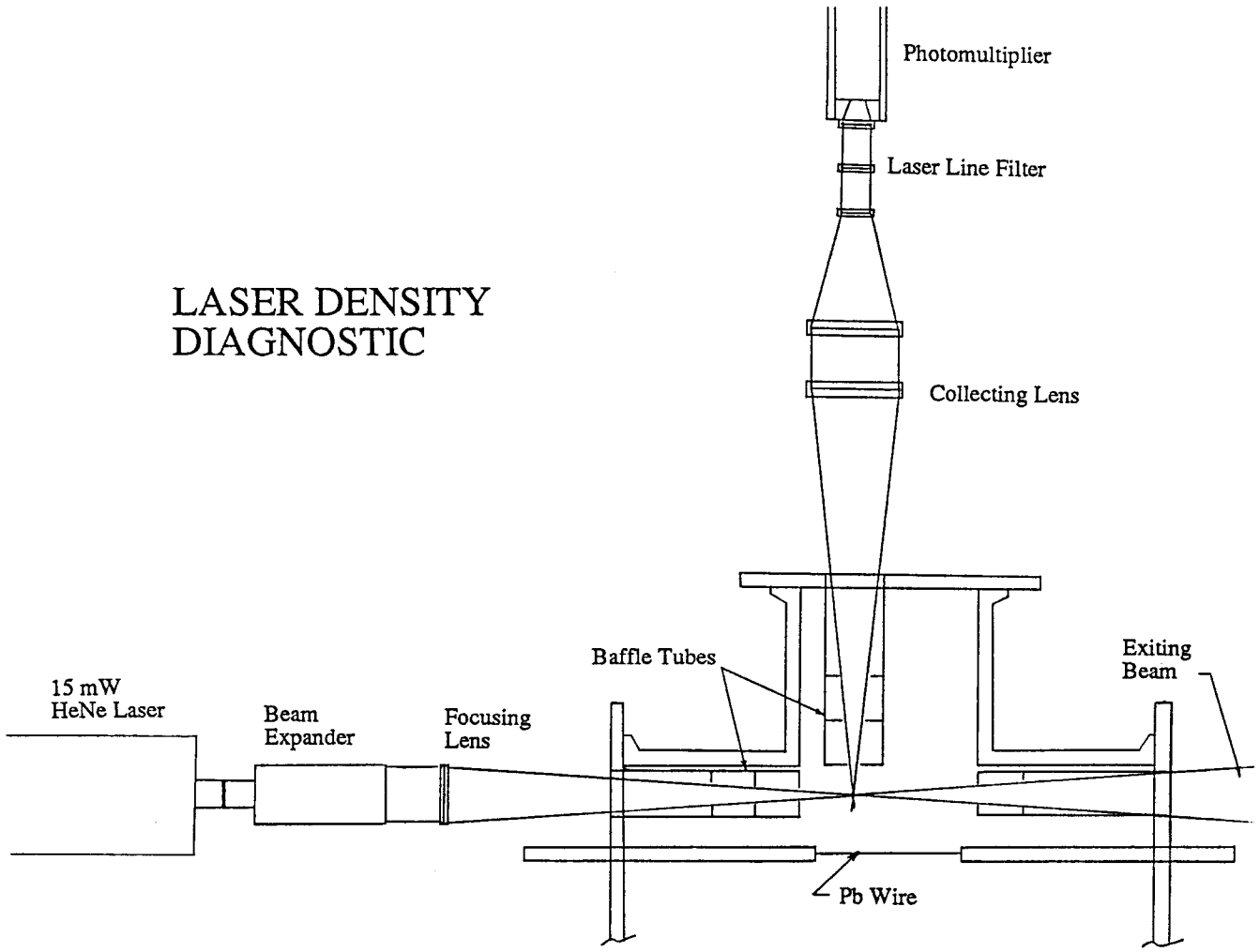

Figure 4.3. Laser Rayleigh scattering density diagnostic system.

are then filtered and focused onto a photomultiplier tube detector. The unscattered light is directed out of the chamber to a beam swallower. The system is mounted on a rigid framework constructed of heavy steel channel.

One of our early concerns about such a system was that the laser windows in the chamber would become fogged with condensing metal during the course of a single test. This might seriously attentuate the signal and would make the interpretation of the results more uncertain. To reduce the potential for fogging, baffle tubes were installed at each of the three laser windows in the chamber. Each has a series of two or three baffles which have center holes only slightly larger than the diameter of the converging or diverging laser beam. This limits the area exposed to the condensing vapor. In addition the baffle tubes do not point directly to the centerline and the vaporizing wire. The baffle tubes have an important side benefit in that they also block a great deal of stray light which might also mar the signal.

The system has been assembled and the optical components set up, aligned, and focused. Since the photomultiplier tube has not yet been delivered, preliminary experiments were performed using an avalanche photodiode detector that was available in our laboratory. Due to the lower gain of this detector, it was necessary to use it in a transmission mode. The beam swallower was removed and the photodiode detector mounted in its place. The AC-coupling of this detector limits it to measurement of fast transient signals only.

The preliminary experiments yielded detector signals similar to the example shown in Fig. 4.4. After the discharge is triggered, the signal drops due to the scattering of the light by the vapor. The signal then recovers over a significantly longer period of time. This is the expected behavior. The peak which is superimposed on the recovering voltage may be due to the visible flash of the wire vaporizing.

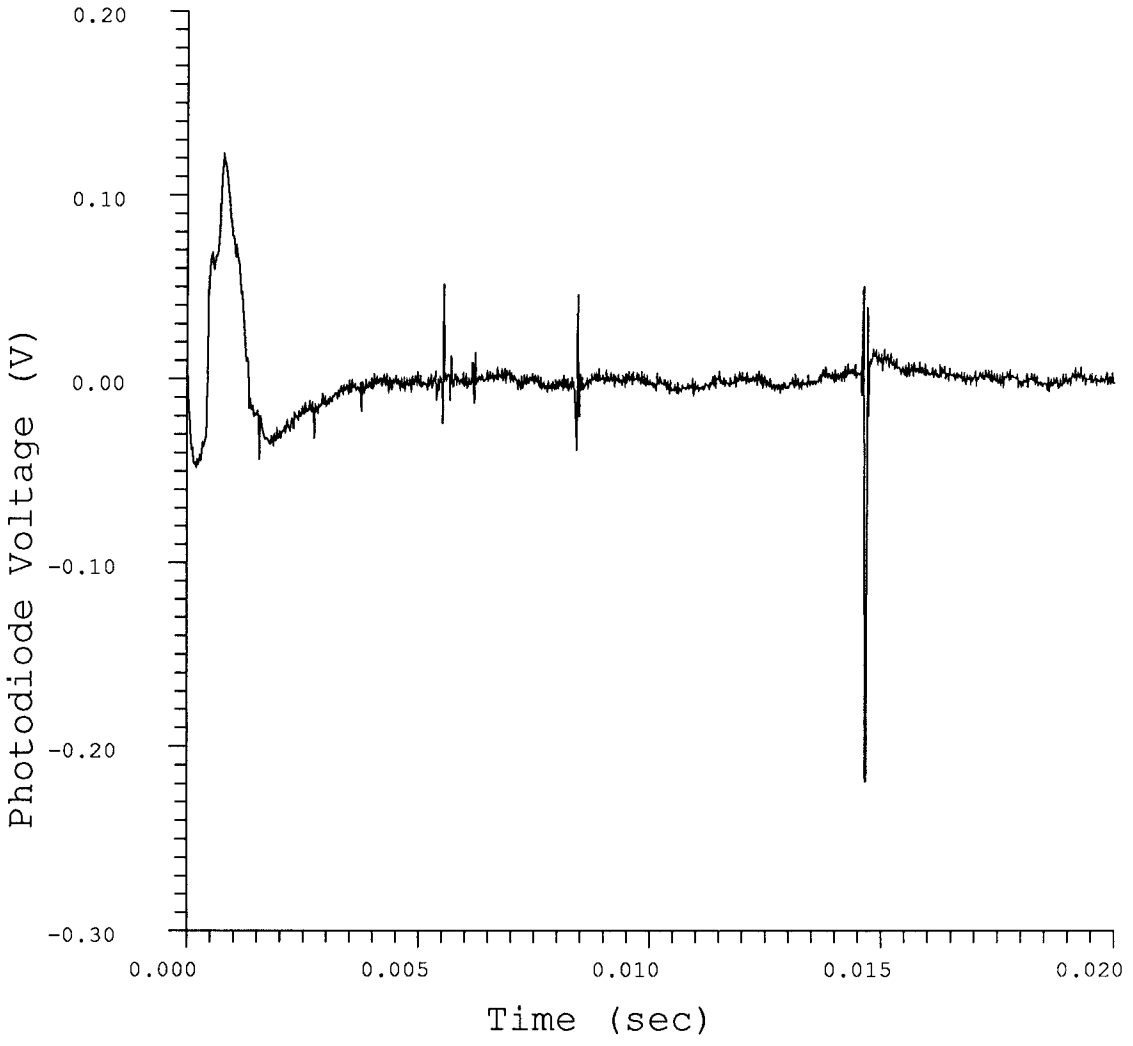

Figure 4.4. Photodiode voltage vs. time. Experiment characteristics: transmission mode, 3500 volts, 0.88 gm Pb, 82 m torr.

4.7 Future Work

The tasks undertaken in the immediate future will be to complete the installation and checkout of the diagnostics in the Pyrex chamber. A set of tests will then be performed to characterize the performance of the diagnostics and to better understand the physical phenomenon of the wire vaporization and vapor condensation. Based on these tests, modifications and refinements in the equipment, procedure, and diagnostics would be evaluated and implemented as necessary.

Using the experience gained in the tests in the Pyrex chamber, the detailed design of the heated experimental chamber would then begin. Following the completion of the design, materials and supplies would be ordered. Construction of the chamber would start as soon as the materials arrived. Testing and checkout of the chamber would follow immediately. The actual experimental runs would then commence.

References for Section 4

[1] L. Pong et al., "Liquid Metal Condensation in the Cavity of the HIBALL Heavy Ion Fusion Reactor," Nuclear Eng. & Design/Fusion 3, 47 (1985).

[2] R.R. Peterson et al., "Inertial Confinement Fusion Reactor Cavity Analysis: Progress Report for the Period 1 July 1986 to 30 June 1987," UWFDM-725 (1987).

[3] B. Badger et al., "HIBALL - A Conceptual Heavy Ion Beam Driven Fusion Reactor Study," University of Wisconsin Fusion Technology Institute Report UWFDM-450 (1981).

5. TARGET CHAMBER SIMULATIONS FOR THE LMF

We have used the improved versions of the CONRAD and IONMIX computer codes to simulate the behavior of target chamber gases in LMF designs suggested by personnel at LLNL. We have considered three target chamber designs; parameters for all three designs are given in Table 5.1. The three designs are 1) a graphite lined chamber where the target explodes in a vacuum, 2) a similar arrangement but with a lucite shell surrounding the target to stop the x-rays and ions, and 3) a graphite lined chamber filled with 1 torr argon to stop the x-rays and ions.

For these simulations, we have used target parameters provided by personnel at LLNL [1]. The target x-ray spectrum is shown in Fig. 5.1 and we assumed that the debris ions were only 500 keV Pb ions. The 1000 MJ of yield was assumed to be partitioned 200 MJ into ions, 200 MJ in x-rays and 600 MJ into neutrons.

The calculations were done with the CONRAD code, using IONMIX equations-of-state and opacities. We did not use the time-dependant debris ion charge state option, but did use the newly developed vaporization and condensation package in CONRAD. Since we used IONMIX results, we did take it into account that the target chamber gases might not be in collisional equilibrium.

5.1 Bare Target in a Vacuum

When a 1000 MJ target explosion occures in a 8 meter radius graphite lined target chamber with a very low density cavity gas, the roughly 200 MJ of target x-rays vaporize some of the graphite. Our simulations predict how much graphite is vaporized and the behavior of that vapor as it moves into the target chamber and interacts with the target generated ion debris. Numerical results of these simulations are given in Table 5.1.

Table 5.1. CONRAD Simulations for LMF Target Chamber Designs

	1	2	3
Target Yield (MJ)	1000	1000	1000
X-ray Energy (MJ)	200	200	200
Debris Ion Energy (MJ)	200	200	200
Target Chamber Radius (m)	8	8	8
First Wall Material	graphite	graphite	graphite
Gas Species	carbon	CH_2	argon
Gas Density (cm^{-3})	3.55×10^{11}	3.55×10^{11}	3.55×10^{16}
X-ray Energy Reaching Wall (MJ)	200	6.8	28
Debris Energy Reaching Wall (MJ)	0	0	0
Energy Radiated from Gas to Wall (MJ)	14	247	344
Maximum Mass Vaporized from Wall (gm)	2230	----	820
Maximum Radiant Heat Flux on Wall (MW/cm^2)	17.4	25.3	8.6
Total Impulse on Wall (Pa-s)	39.6	.17*	31.9

*This simulation does not reach the time when the remnants of the lucite shield hit the wall.

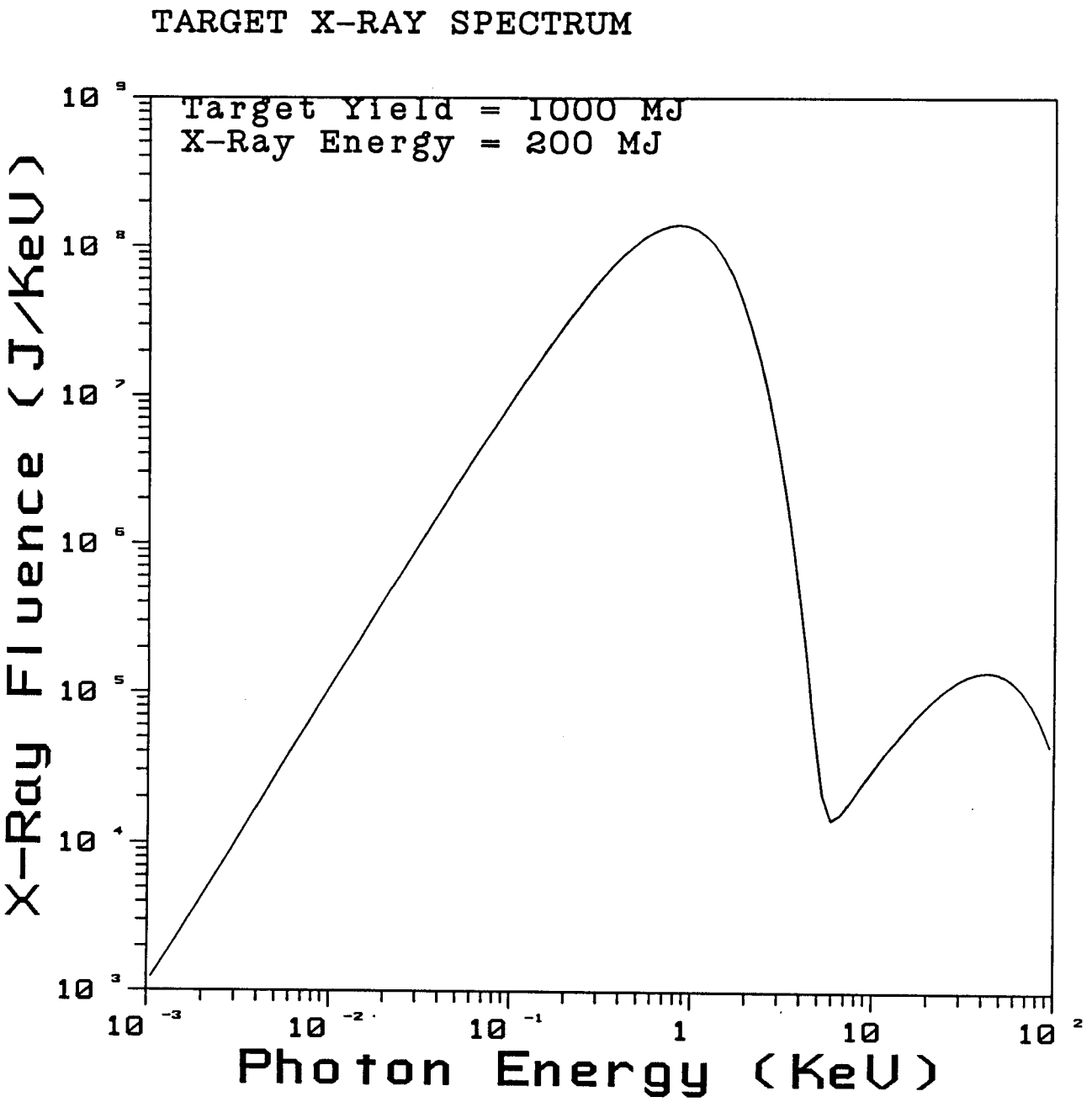

Figure 5.1. Target X-ray spectrum.

CONRAD simulations predict that 2.23 kg of graphite is vaporized by the target x-rays. The maximum possible vaporized mass, the x-ray energy divided by the latent heat of vaporization of graphite, is 3.35 kg. The calculated value is less than this, both because some energy is deposited in matter that does not vaporize and because some of the energy is deposited in matter that is raised to energy densities higher than that required to vaporize. We have estimated that the recoil impulse from this rapid vaporization is 2.8×10^3 dyne-s/cm^2.

The vapor created by the target x-rays moves into the target chamber and interacts with the target chamber gases. Figure 5.2, a plot of the positions of Lagrangian zone boundaries versus time, shows the vapor moving into the target chamber. One can see here that the momentum of the vapor carries the vapor into the center of the chamber and greatly compresses the original target chamber gas. The target debris ions are stopped in this vapor and, as we will discuss later, the resulting heating drives this inward motion.

One sees in Fig. 5.3 the temperature profiles in the vapor at various times. The ions heat the inner edge of the vapor, but the most noticeable feature of this plot is the compressional heating of the vapor as it reaches the center of the chamber. Since CONRAD is a one-dimensional code, multi-dimensional effects will probably reduce the maximum temperature reached during this compression to less than the 400 eV shown in Fig 5.3.

Figure 5.4 shows how the energy in the vapor is partitioned between internal, kinetic, and radiated components as a function of time. The vapor begins with about 10 MJ of internal energy and very little kinetic or radiated energy. The remaining 200 MJ, that the target x-rays had, is in latent heat of vaporization or was deposited in matter that did not vaporize. The ions deposit their energy at around 10^{-7} seconds, which can be seen in Fig. 5.4

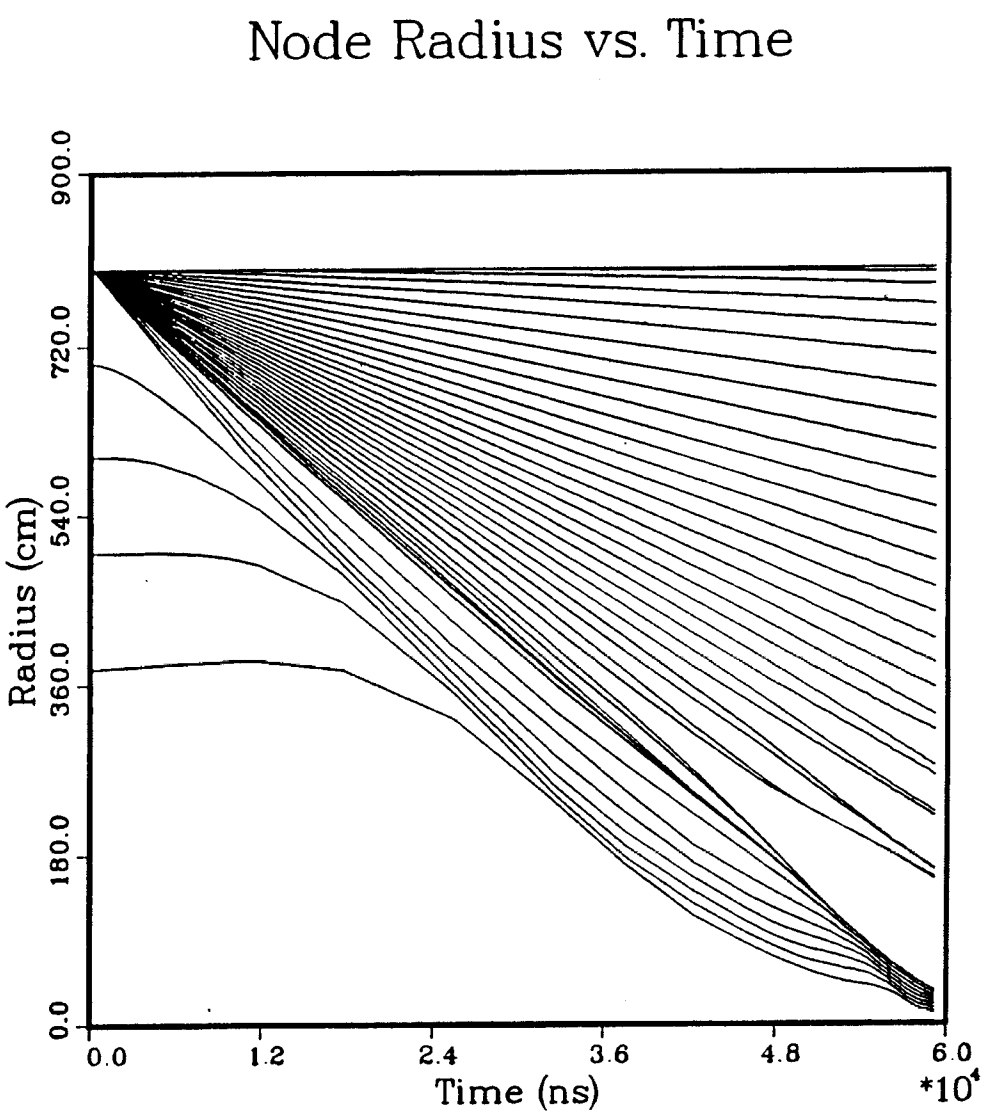

Figure 5.2. Positions of Lagrangian zone boundaries versus time for Option #1. The target explodes in a low density gas.

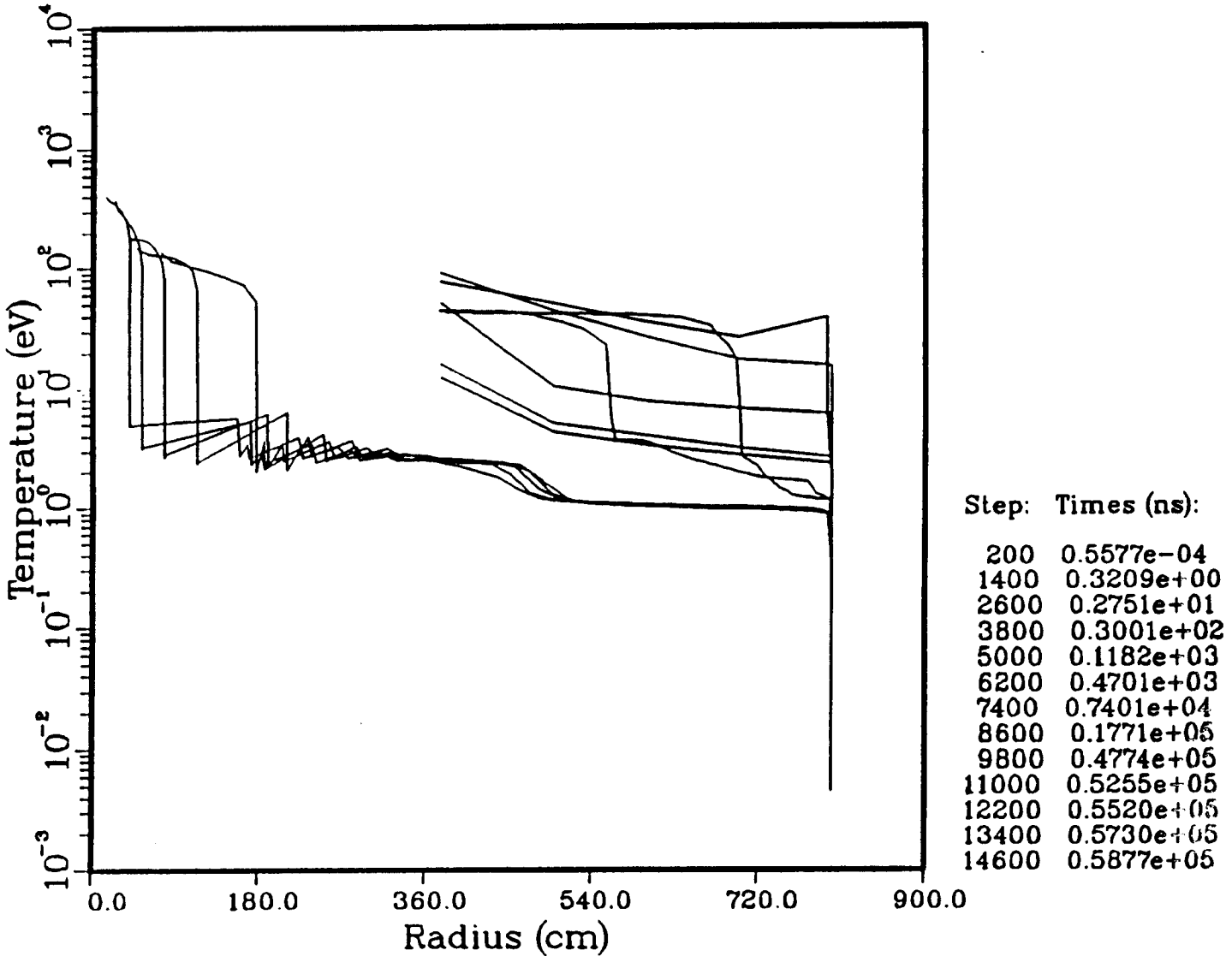

Figure 5.3. Temperature profiles in the vapor at various times for Option #1. The target explodes in a low density gas.

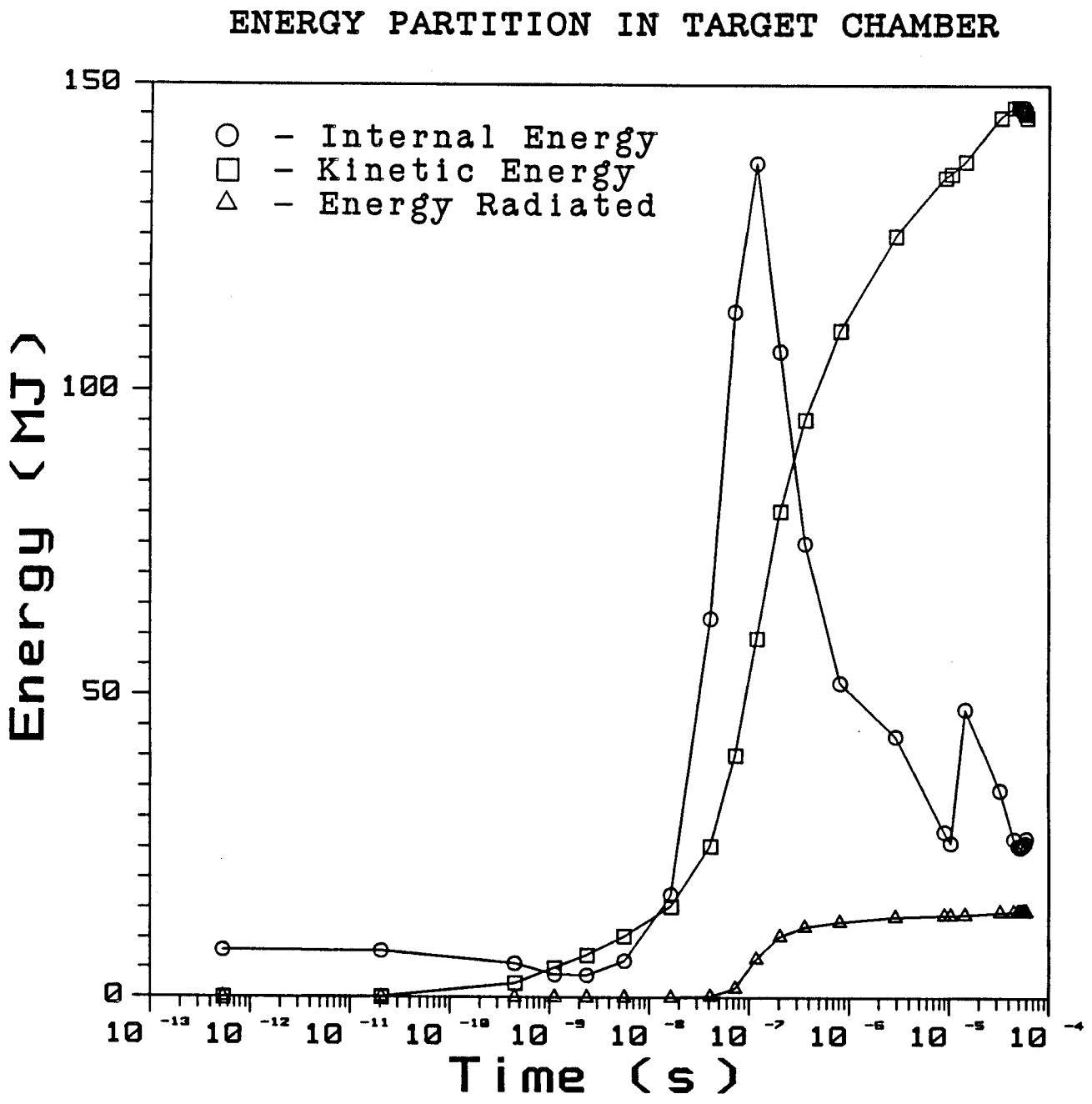

Figure 5.4. Energy partitioning in the target chamber gases between internal, kinetic, and radiated energy as a function of time for Option #1. The target explodes in a low density gas.

when the internal and kinetic energy make a combined increase of about 200 MJ. One sees here the internal energy being converted into kinetic energy as the high pressure of the debris heated vapor drives the inward moving motion. One also sees that the radiation only accounts for about 15 MJ by 5×10^{-5} seconds. At this time, 150 MJ are in inward moving kinetic energy which will ultimately be turned back into internal energy and more radiation. We beleive that the one-dimensional nature of CONRAD prevents the accurate simulation of this situation.

5.2 Target Surrounded by a Lucite Shell in a Vacuum

We have used the CONRAD computer code to study the behavior of the lucite x-ray shield proposed for the LLNL LMC studies. We have gone to considerable effort to optimize the Lagrangian zoning used in this problem. The first calculations had rather thick Lagrangian zones on the outer edge of the shell, which after some thought we realized was not the best zoning scheme. The final calculations had thin zones at the inner and outer edges of the shell, with the zones thickest at the center of the shell. The outermost zone in the shell is about 1×10^{-7} cm thick, which personnel at LLNL suggested. We have kept the mass ratio between any two adjacent zones to less than about 1.3. We have also placed about twenty zones to the region between the shell and the wall. We found that if we had but one zone in the low density region between the outer edge of the shell and the wall, a distance of 794 cm, causality was violated in the photon time-of-flight.

We tested the new zoning scheme by comparing results from the final zoning, which had 121 zones, with a calculation with 242 zones. In Fig. 5.5, the heat flux at the 8 meter wall is shown for the two zoning schemes. This is a log-log plot, so the evident agreement is overemphasized to some extent;

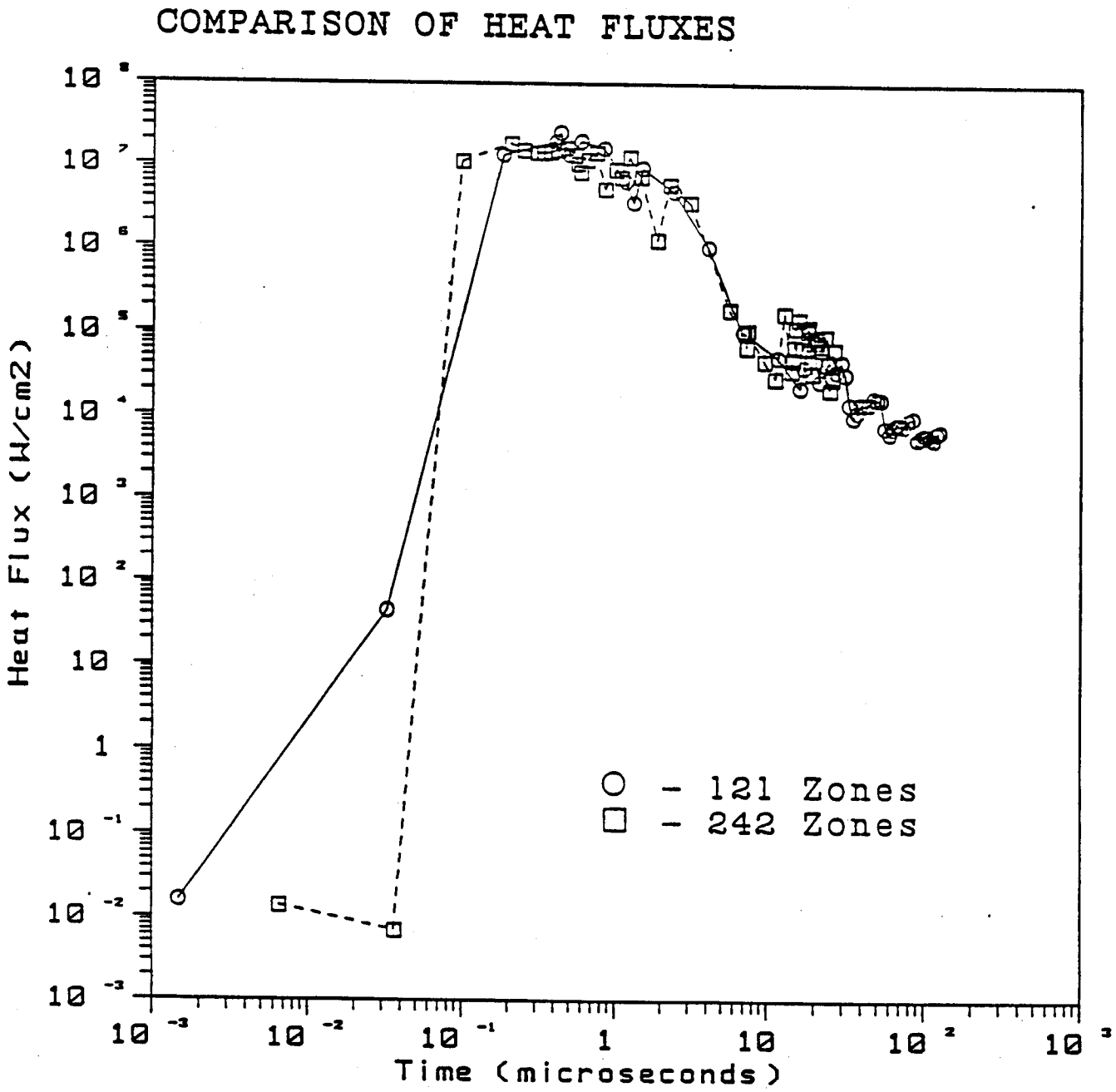

Figure 5.5. Heat flux at the 8 meter wall for the two zoning schemes for Option #2. The target explodes inside a 1 cm thick lucite shell in a low density gas.

though we do believe that the agreement between the 121 and 242 zone cases is adequate to let us proceed with the 121 zone scheme as the standard. In Fig. 5.6, the pressure on the wall is shown as a function of time for the calculations with 121 and 242 zones. Here one sees that times that pressures pulses reach the wall are the same for the two zonings, though the maximum peaks are different. The impulse on the walls is about the same. From this point on, we have used 121 zones for all calculations.

The hydromotion in the shell is shown in Fig. 5.7 and 5.8. In Fig. 5.7, every zone boundary is shown, while in Fig. 5.8 every third boundary is shown. Figure 5.8 better shows the shock moving through the shell. Initially, one sees material vaporizing off of the inside of the shell and off of the outside of the shell. The very strong vaporization on the inside is due to a combination of x-ray and ion heating from the target. One can see the shock moving through the shell and breaking material off of the shell at a time of about 5.5 microseconds. The temperature profiles during this process are shown in Fig. 5.9. The maximum temperature in the inner edge of the shell is about 40 keV.

Looking at the whole target chamber, the hydromotion is shown in Fig. 5.10 and Fig. 5.11. In Fig. 5.10 one can see a shock caused by the initial vaporization reaching the surface of the wall at 8 microseconds and a shock generated by the material spalled off the back of the shell reaching the wall at 16 microseconds. In Fig. 5.11, one sees the shell disintegrating where it looks as if the material from the main body of the shell would reach the wall at about 200 microseconds. The velocity profiles are shown in Fig. 5.12, where one can see velocities of 10^8 cm/s. In Fig. 5.13, one sees a radiation wave burning through the disintegrating shell.

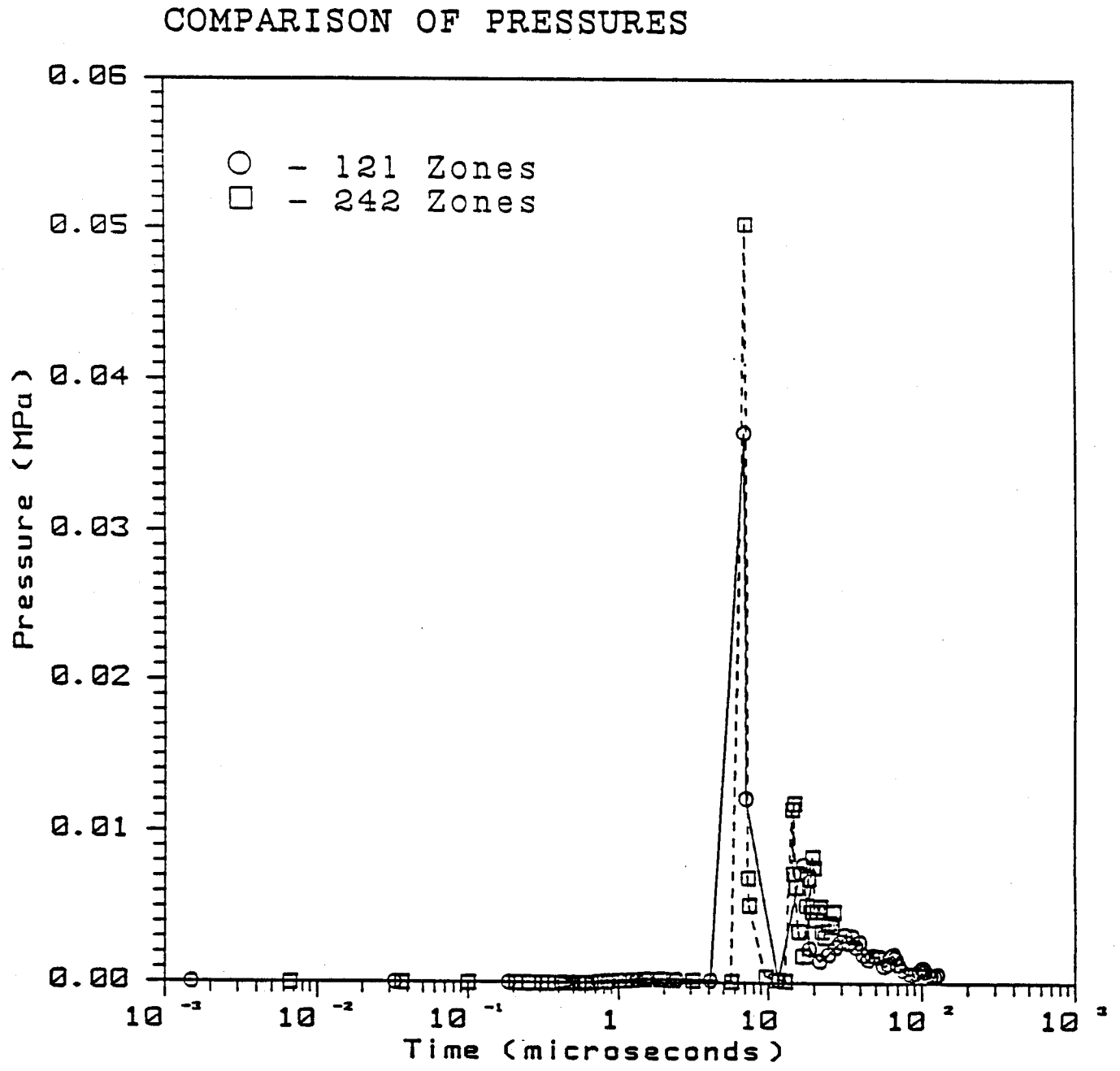

Figure 5.6. Pressure on the 8 meter wall for the two zoning schemes for Option #2. The target explodes inside a 1 cm thick lucite shell in a low density gas.

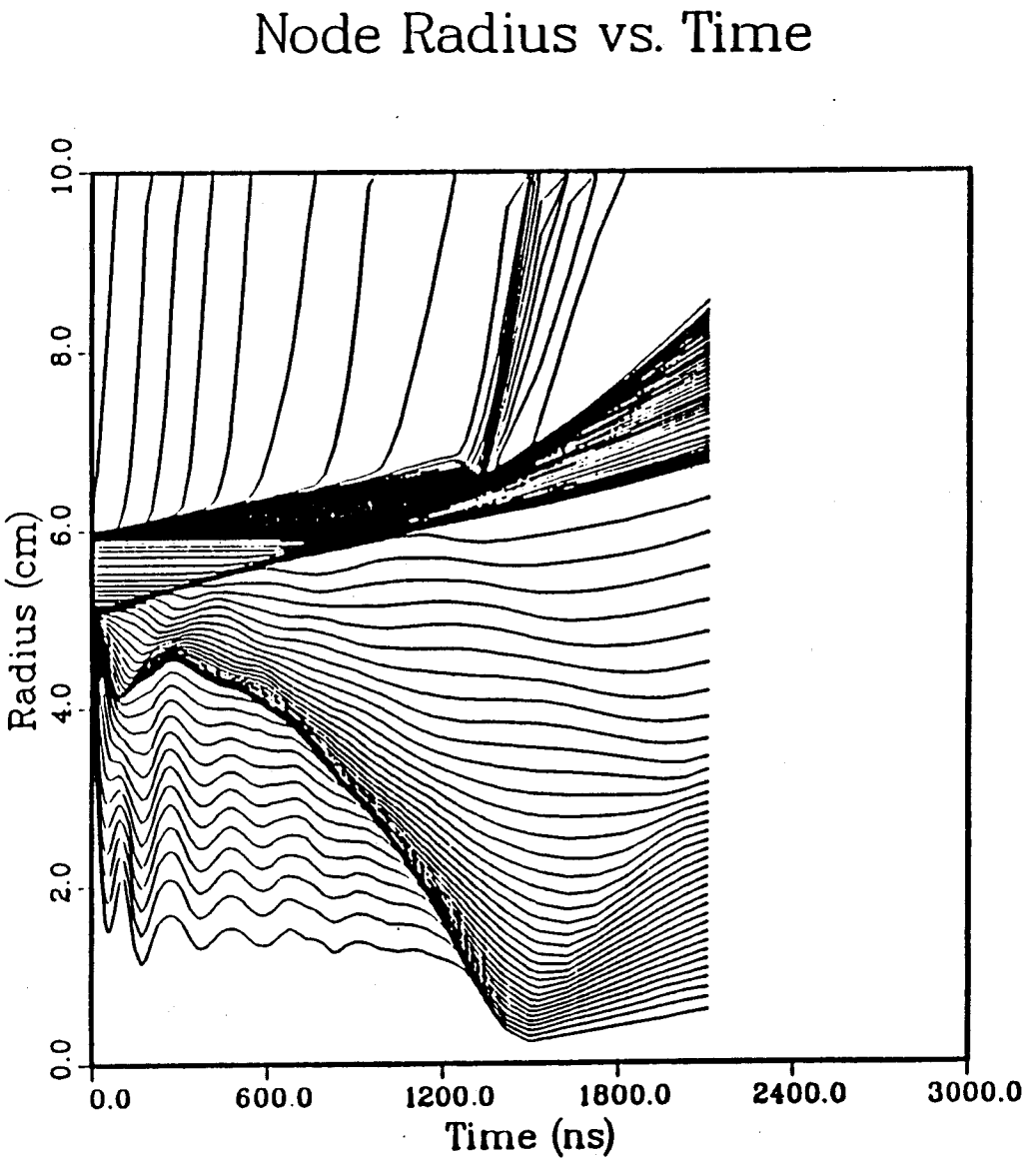

Figure 5.7. Positions of Lagrangian zone boundaries versus time for Option #2. The target explodes inside a 1 cm thick lucite shell in a low density gas.

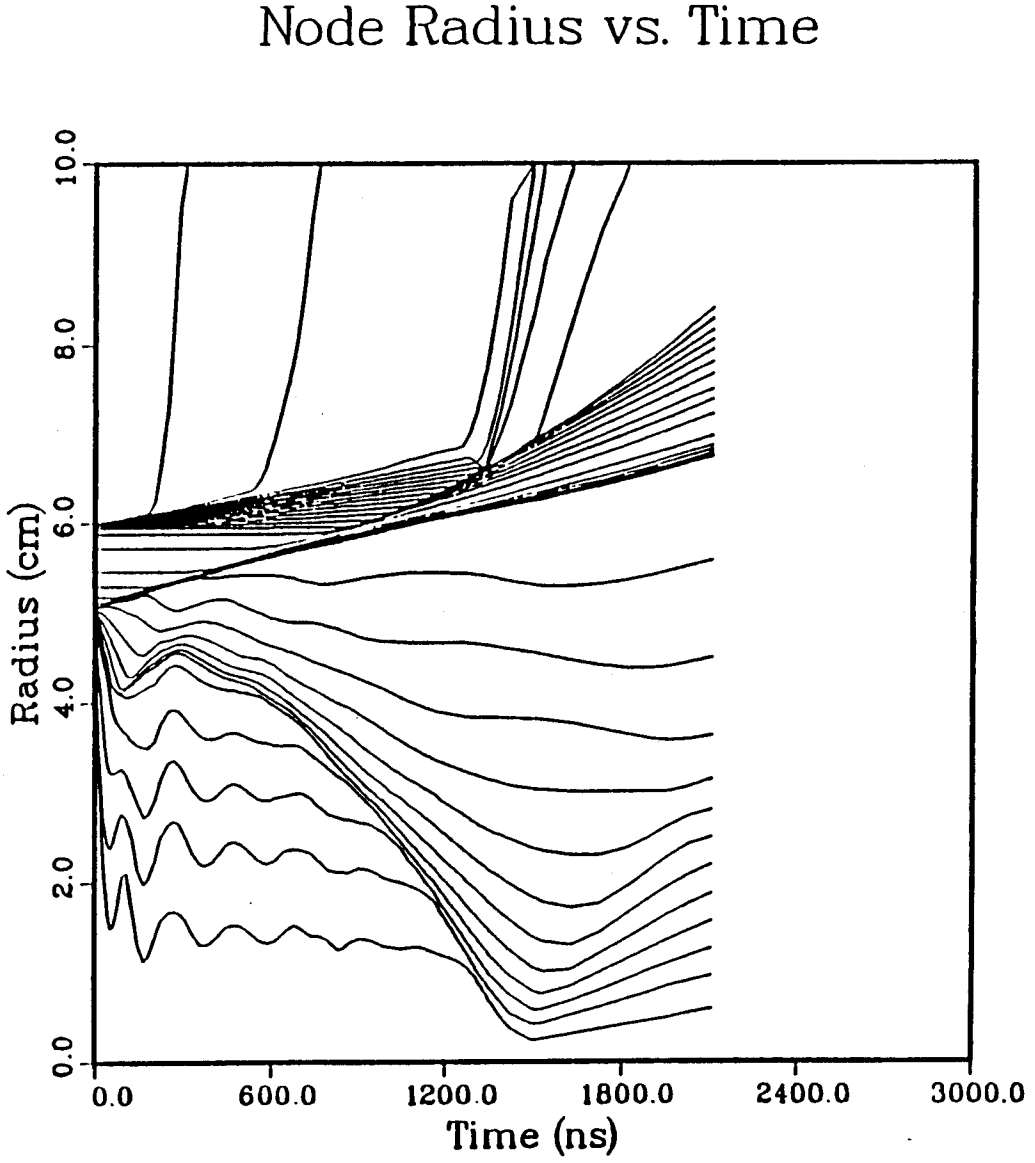

Figure 5.8. Positions of Lagrangian zone boundaries versus time for Option #2. The target explodes inside a 1 cm thick lucite shell in a low density gas.

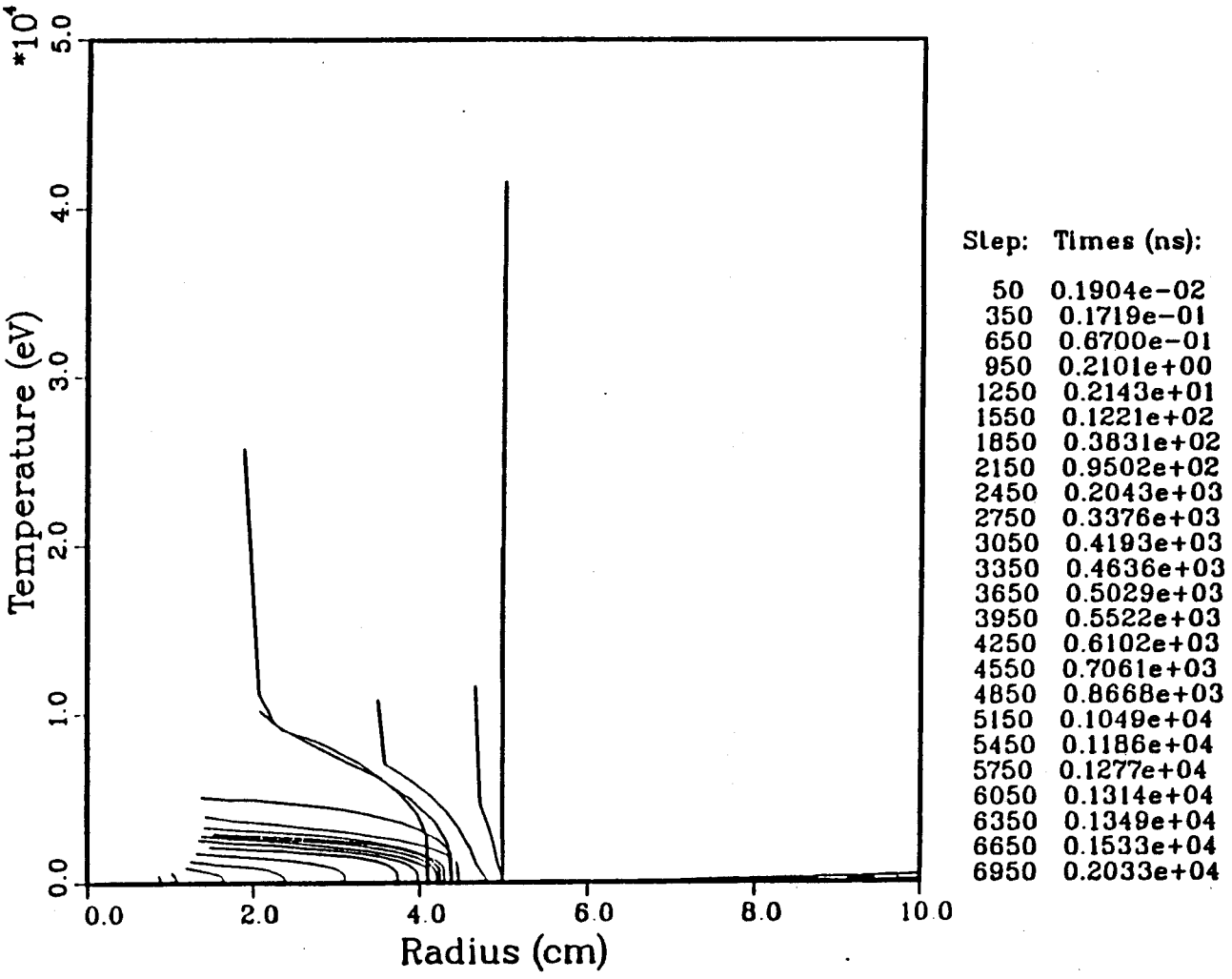

Figure 5.9. Temperature profiles in the target chamber for Option #2. The target explodes inside a 1 cm thick lucite shell in a low density gas.

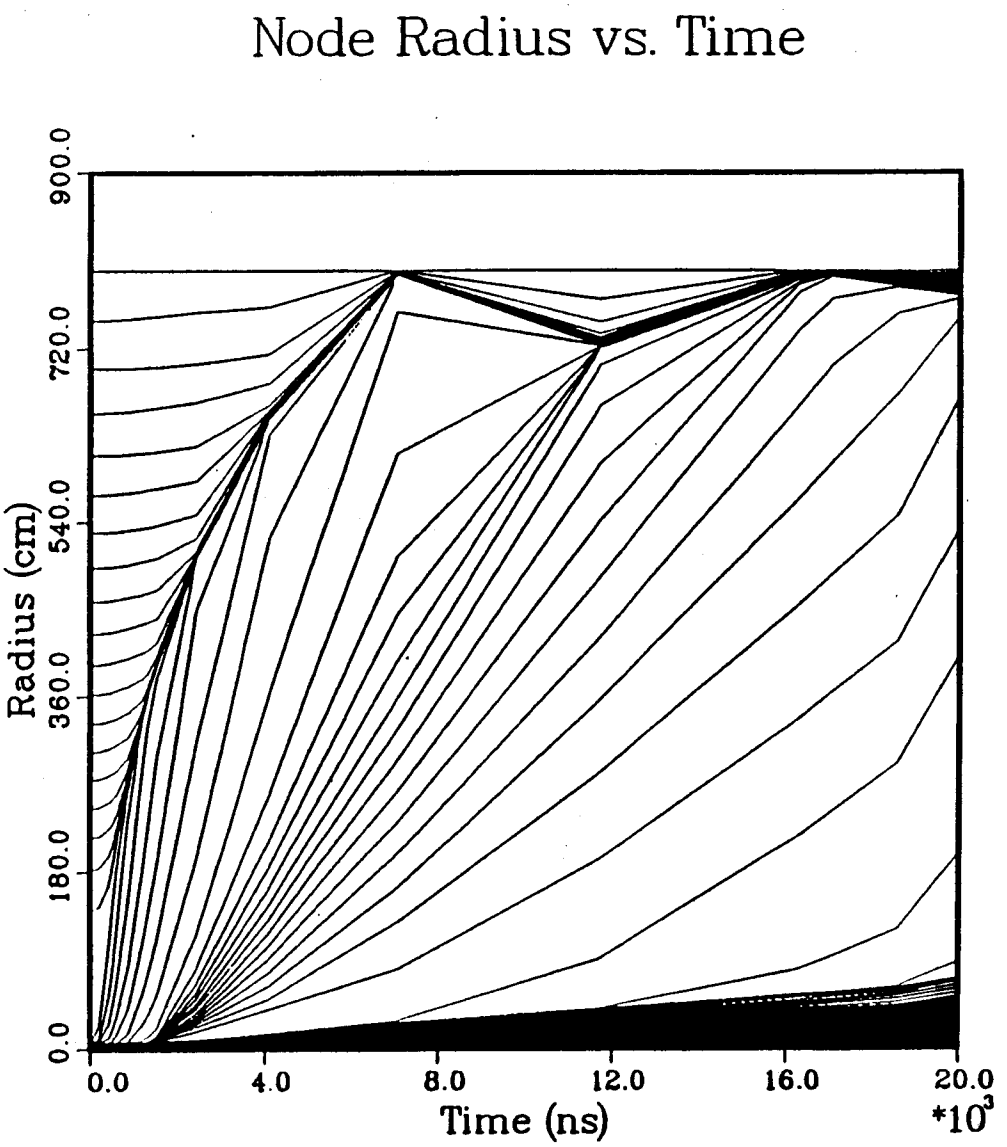

Figure 5.10. Positions of Lagrangian zone boundaries versus time for Option #2. The target explodes inside a 1 cm thick lucite shell in a low density gas.

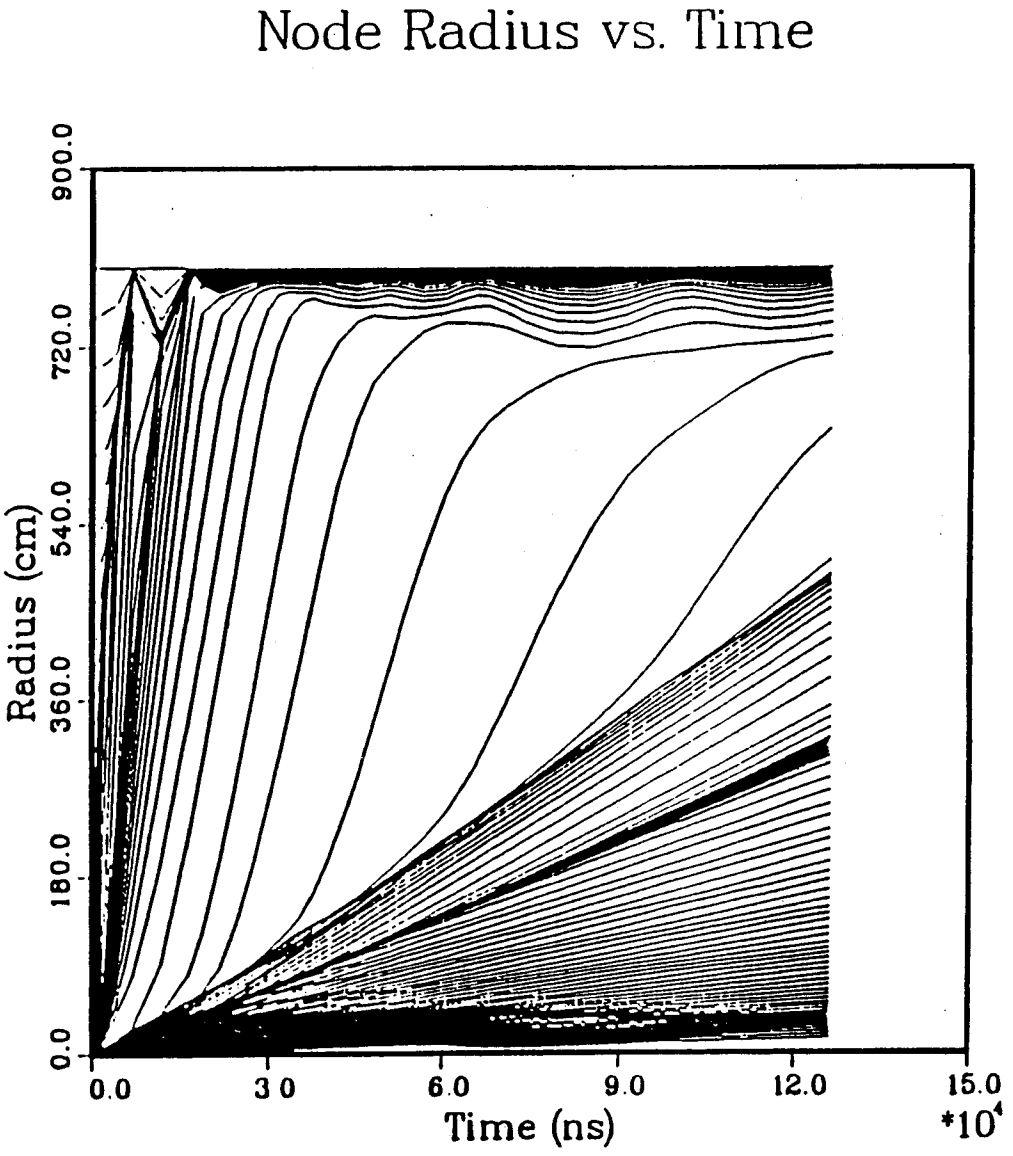

Figure 5.11. Positions of Lagrangian zone boundaries versus time for Option #2. The target explodes inside a 1 cm thick lucite shell in a low density gas.

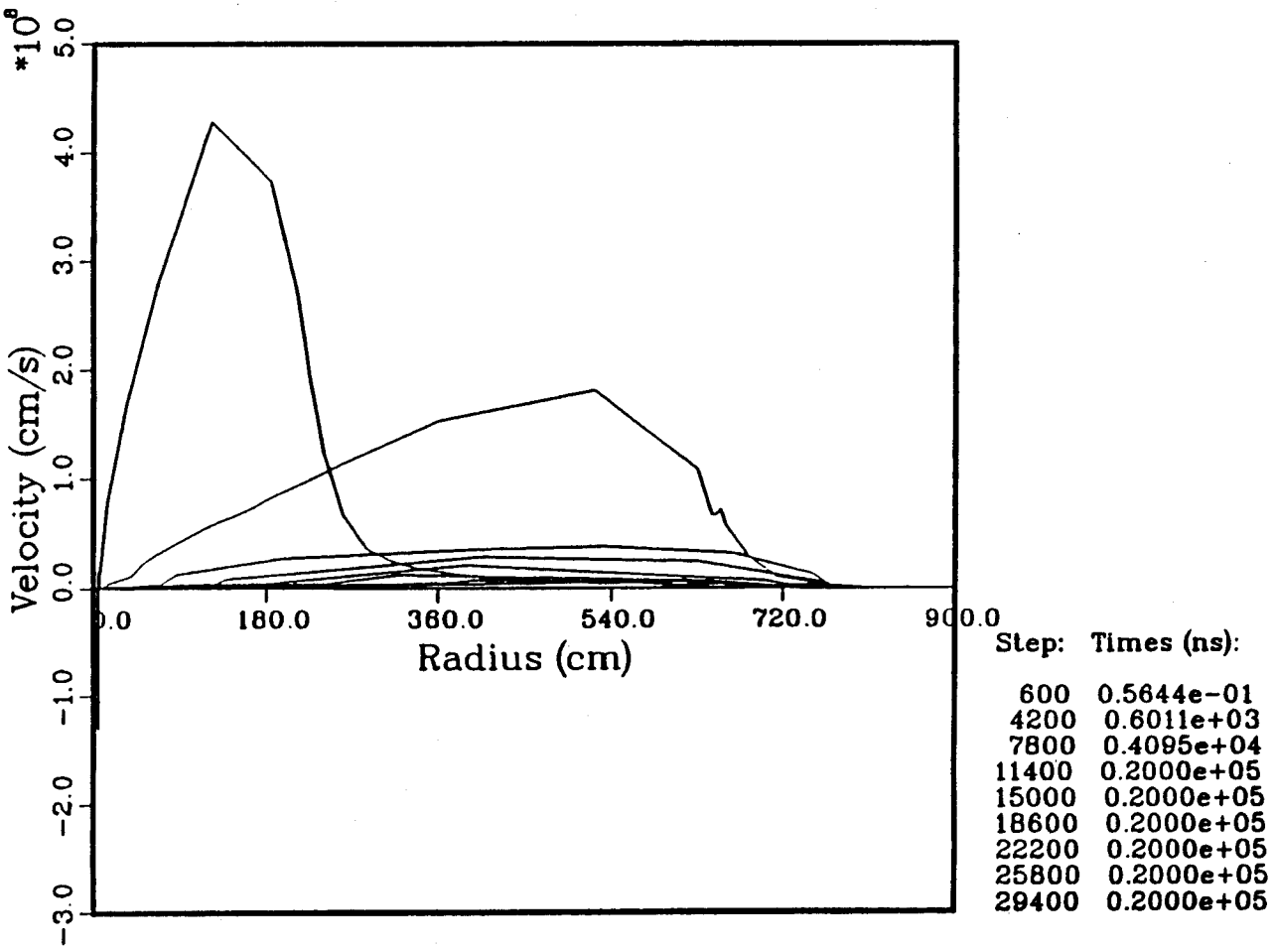

Figure 5.12 Velocity profiles in the target chamber for Option # 2. The target explodes inside a 1 cm thick lucite shell in a low density gas.

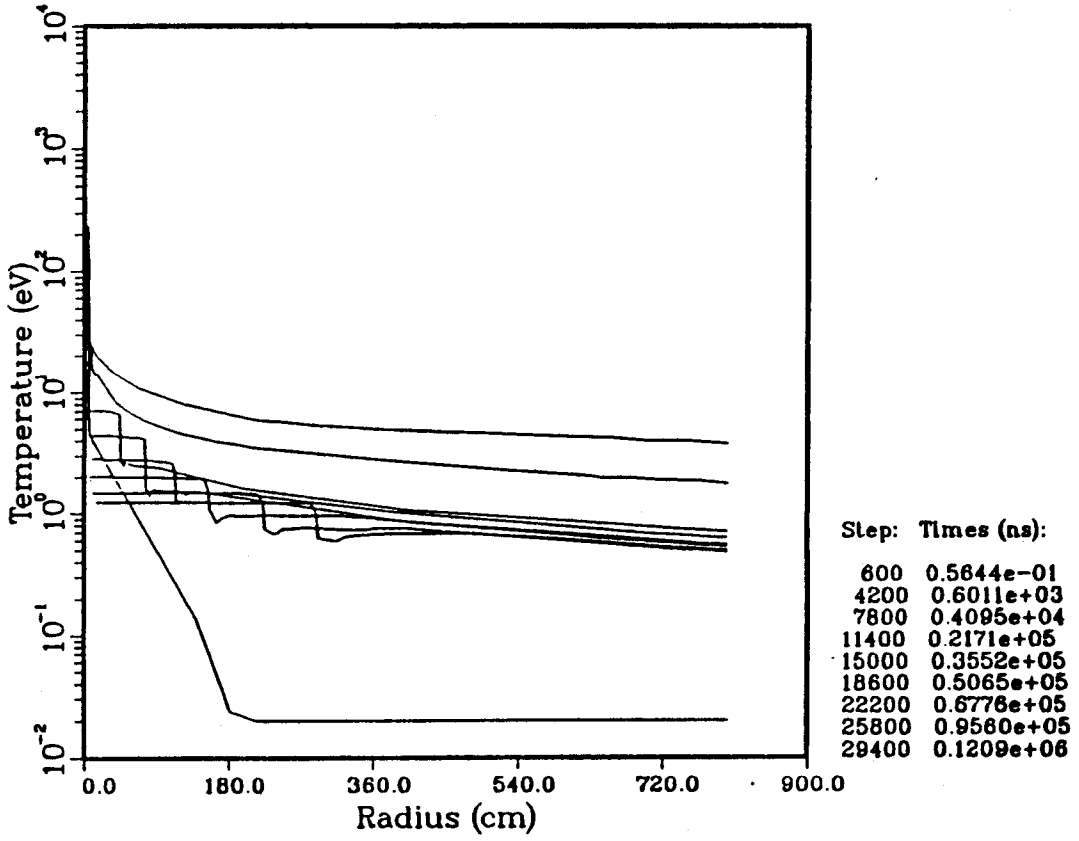

Figure 5.13. Radiation temperature profiles in the target chamber for Option #2. The target explodes inside a 1 cm thick lucite shell in a low density gas.

The energy partitioning within the lucite shell and in the target chamber is shown in Fig. 5.14. The ions deposit this energy by about 10^{-7} seconds and by that time the internal energy, mostly in the shell, goes up to 350 MJ. The shell begins to move and to radiate and by 10^{-4} seconds the radiated energy accounts for more than one half of the total x-ray and ion energy. This will probably lead to vaporization of the wall, but we have yet to consider this effect. By the end of the calculation more than one quarter of the energy is in kinetic energy of the shell, with internal energy being the minority.

This calculation was done without any vaporization of the first wall because we wanted to concentrate on what was happening to the shell. We may do a series of calculations with the vaporization physics in the wall taken into account during the next phase of our work.

5.3 Bare Target in Argon

We have completed some simulations of the target chamber gas behavior for an 8 meter radius chamber filled with argon, the third design. We have assumed that the first wall is made of graphite and that the number density of the argon is 3.55×10^{16} atoms/cm^3 (1 torr).

The results of these calculations are summarized in Table 5.1 and Figs. 5.15 through 5.18. The gas is thick enough that it protects the first wall from the direct effects of the target generated x-rays and ions so that there is no initial vaporization of the first wall. This means, however, that a great deal of energy is being deposited in the gas. Specifically, CONRAD predicts that 372 MJ will be deposited in the gas. The code predicts that a sphere of gas roughly 50 cm in radius will be raised to a temperature greater than 1 keV. This gas then radiates strongly. The heat flux from this radiation is shown in Fig. 5.15. There is structure in the plot that is due to

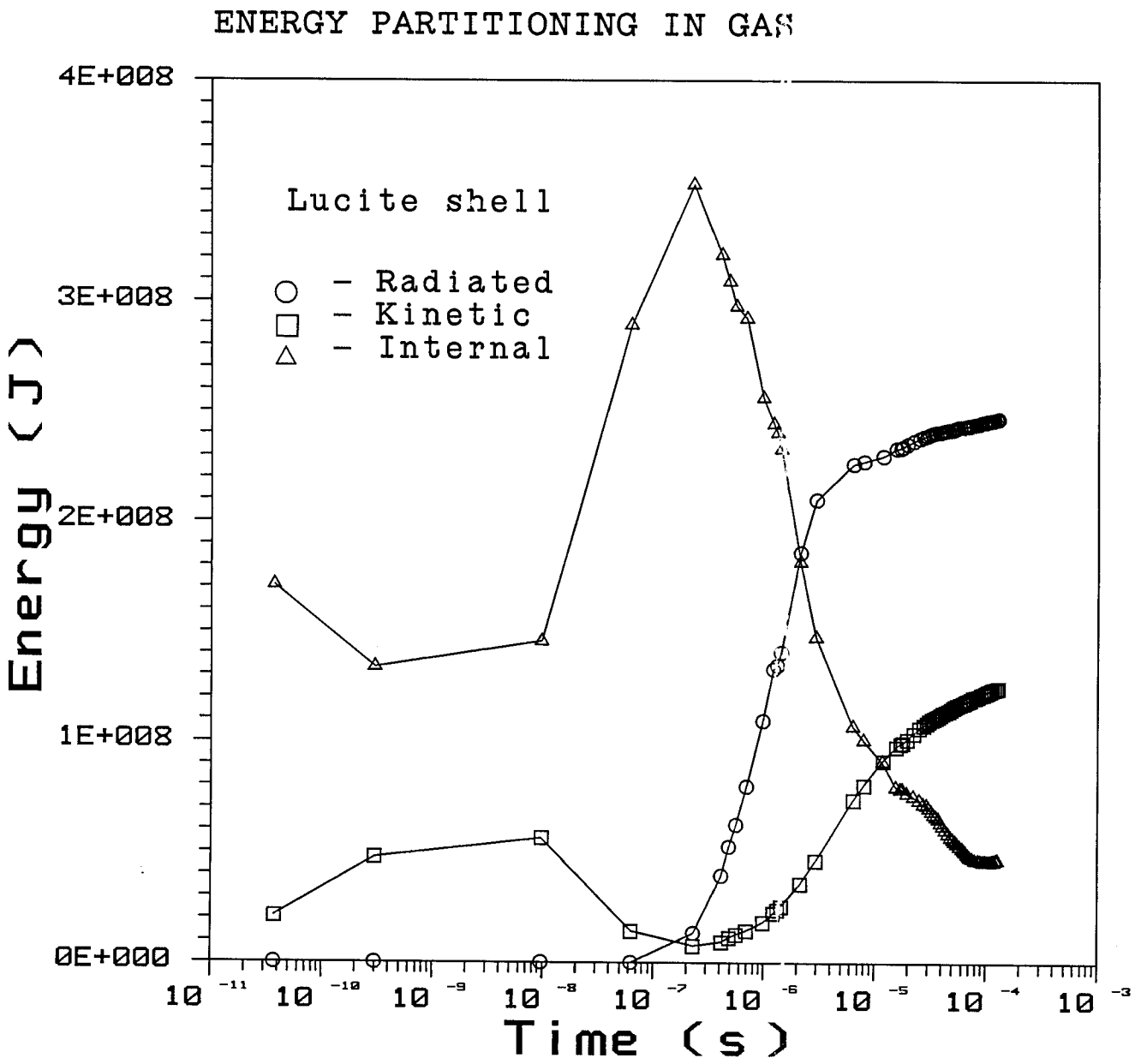

Figure 5.14. Energy partitioning in lucite shell.

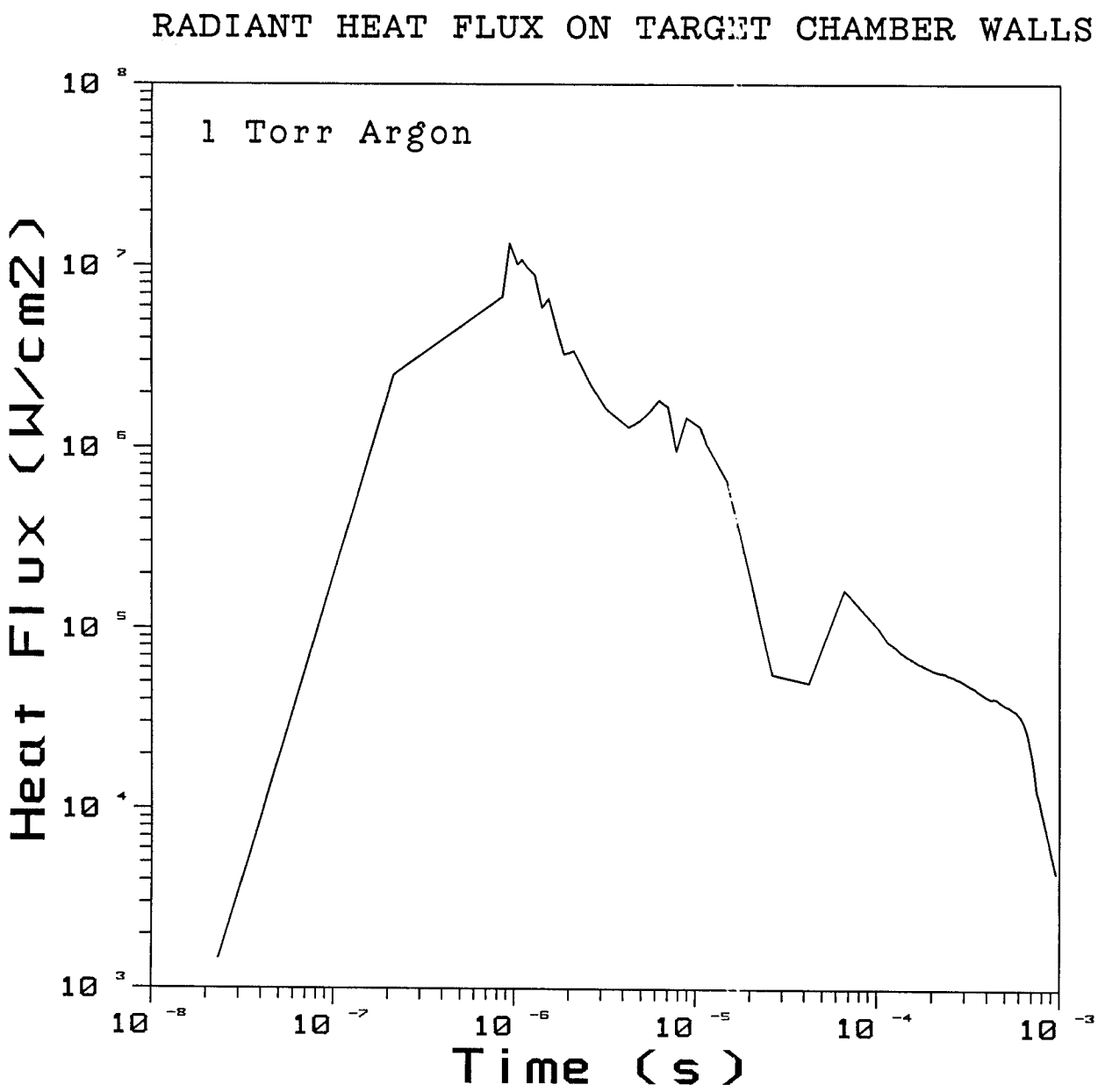

Figure 5.15. Radiant heat flux on the 8 meter radius walls of the target chamber versus time for Option #3. The target explodes in a moderate density argon gas.

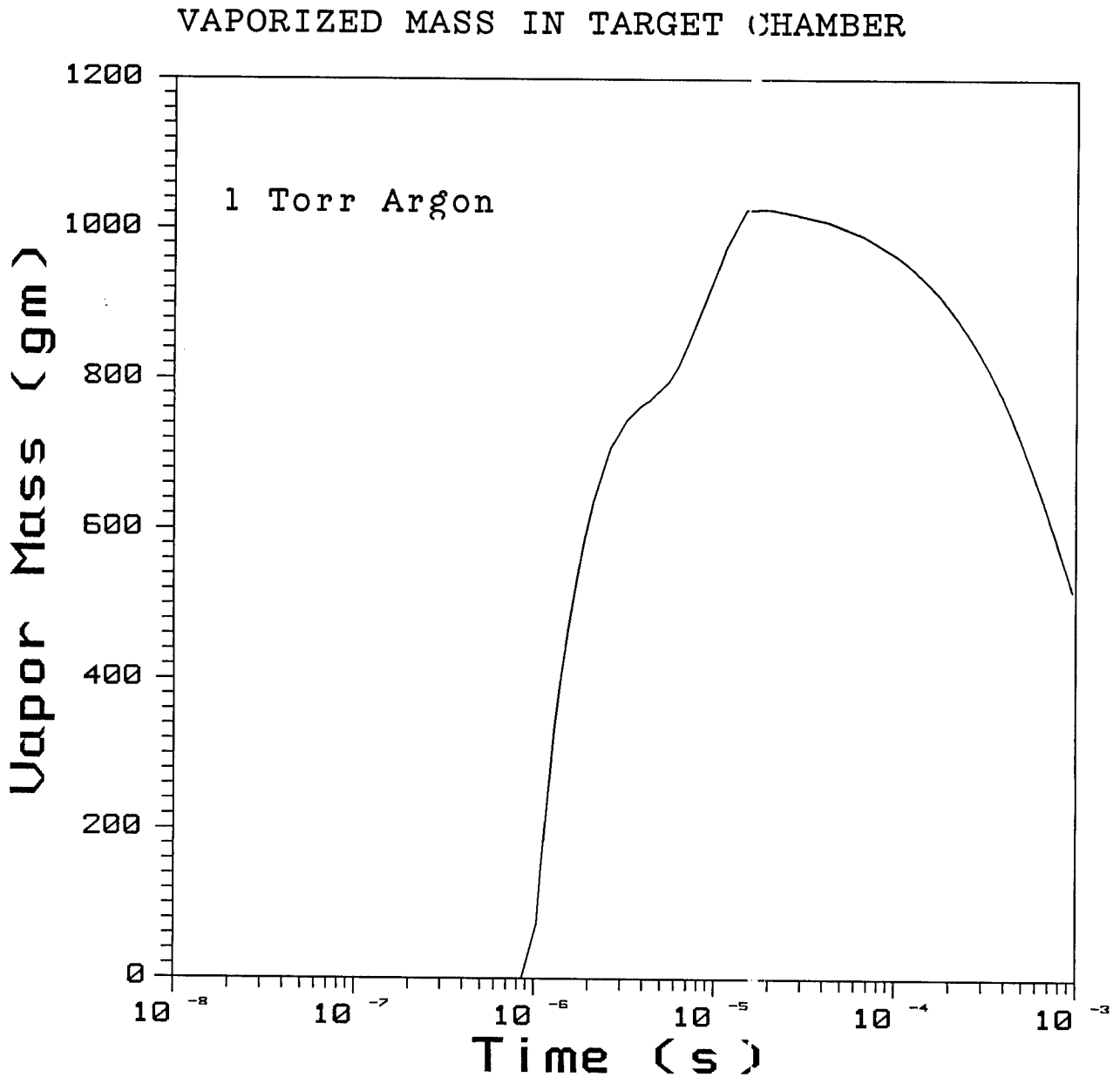

Figure 5.16. Net vaporized graphite in the target chamber versus time for Option #3. The target explodes in a moderate density argon gas.

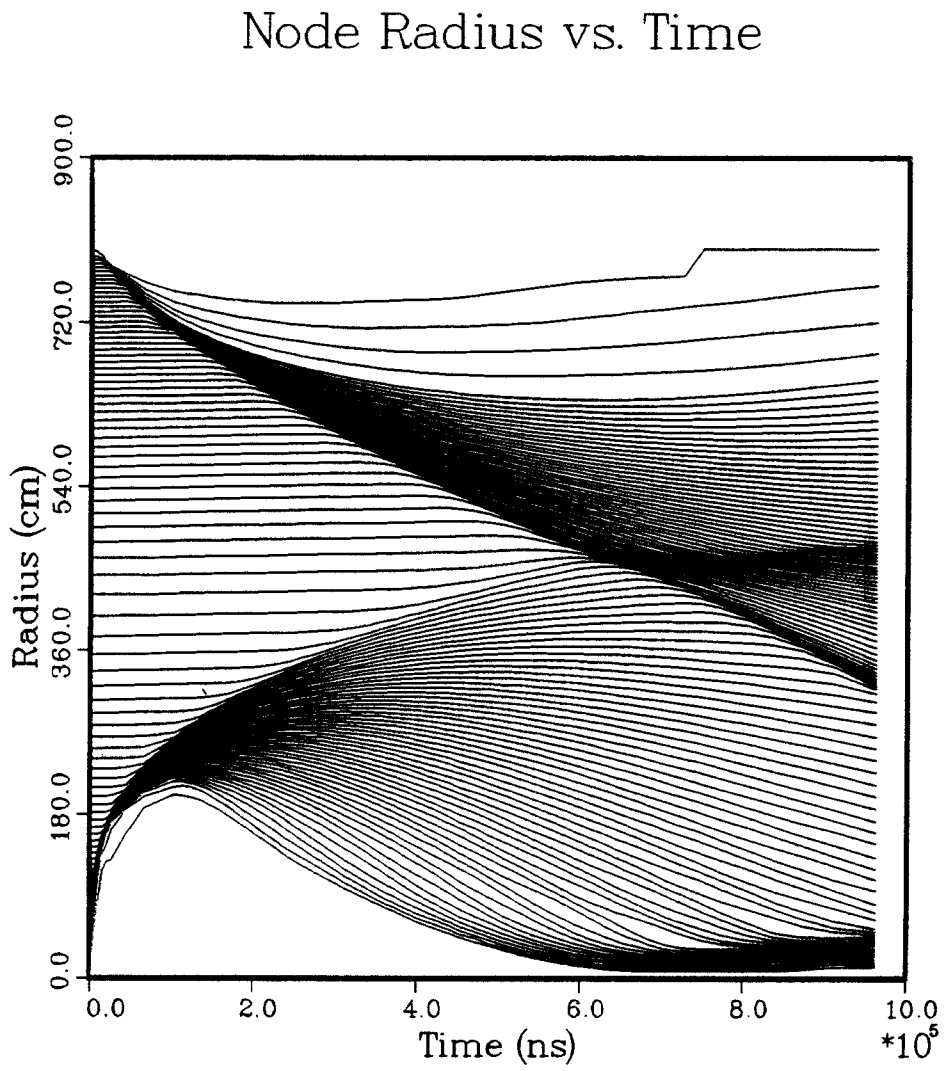

Figure 5.17. Positions of Lagrangian zone boundaries versus time for Option #3. The target explodes in a moderate density argon gas.

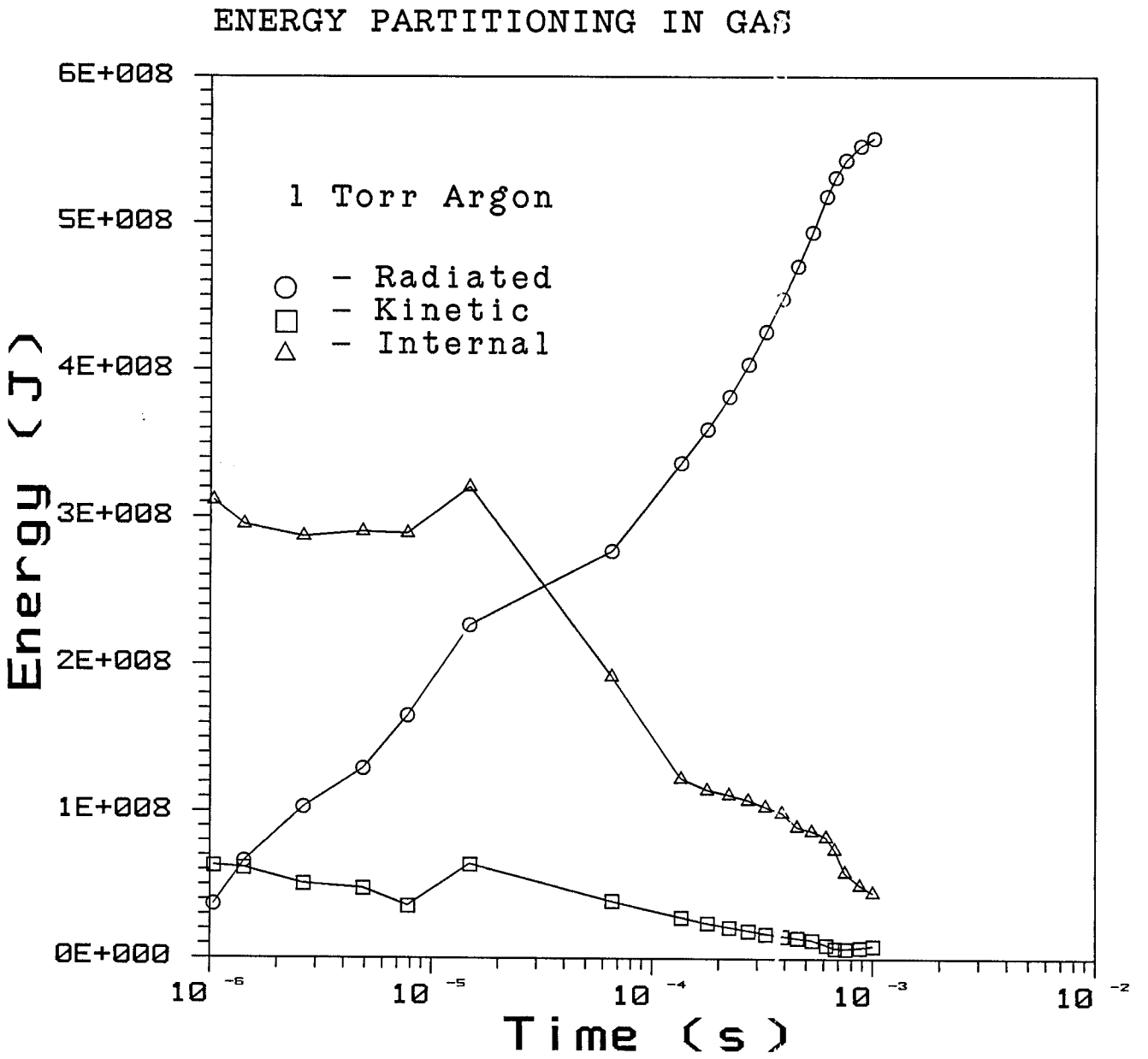

Figure 5.18 Energy partitioning 1 torr argon gas.

the time-dependent deposition of ion energy and the interaction of the radiation with vaporized wall material. During the 1.0 ms of the simulation shown here, there is 344 MJ radiated to the wall. This leads to vaporization of first wall material. The mass of the vaporized material is shown in Fig. 5.16. One sees that there is net vaporization occuring from about 1 microsecond to about 10 microseconds, and that the maximum vapor mass is 820 g. This corresponds to roughly .5 microns being vaporized off of the graphite wall. Past 10 microseconds the vapor is condensing, and by 1.0 ms the vapor mass has fallen to 506 g. The hydromotion is shown in Fig. 5.17, where the positions of Lagrangian zone boundaries are plotted versus time. One sees the outward moving target generated blast and the inward moving cloud of vapor. At about .6 ms, the blast front meets the inward moving vapor at a radius of about 400 cm. The vapor has more momentum than the blast, so it overwelms the blast wave and drives it inward. One notes that this collision generates shocks that move into the vapor and into the background gas. The shock moving into the vapor is almost stationary in the lab frame because of the high velocity of the vapor, and no shock will reach the wall for a long time.

The energy partitioning is shown in Fig. 5.18. Initially, most of the 400 MJ of x-rays and ions are in internal energy of the argon gas. As time progresses, radition becomes the dominant component, leaving very little energy in the internal and kinetic components.

References for Section 5

[1] C.D. Orth, "Improved Understanding of First-Wall Vaporization-Condensation in Inertial Confinement Fusion Reactors," Proceedings of the Seventh Topical Meeting on the Technology of Fusion Energy, June 15-19, 1986, Reno, Nevada.

6. SUMMARY AND FUTURE DIRECTIONS

We have reported our progress on improvements to the IONMIX and CONRAD computer codes, our construction, diagnaostics development, and initial experiments of the condensation experiment, and our simulations of target chamber gas behavior in LLNL LMF concepts. We believe that this work satisfies the tasks on the statement-of-work in Table 1.1. Our progress during this phase sets the stage for the next segment of our work with LLNL.

We have shown the non-LTE effects, as defined in Section 2, can have a marked impact on the radiative properites of target chamber gases. This has lead us to the development of the IONMIX computer code, which replaces the MIXERG computer code in the role of providing equation-of-state and opacity data for the CONRAD code.

We have modified the CONRAD code to do a better job of calculating the energy deposition from target ion debris, and vaporization and condensation of first wall material. The ion deposition can now account for the changing charge states of the ions as they move through the target chamber gas. We have found that the new ion deposition model is able to reproduce available experimental data quite well. The new vaporization and condensation methods have the advantages of better accuracy, the possibility of including the effects of noncondensable gases, and mass transfer that avoids changing the mass of a Lagrangian zone and the related numerical problems. As a result, the energy conservation and run times have been improved.

We have constructed the liquid metal condensation experiment and have developed diagnostics to measure the vapor density in the experimental chamber and the mass condensation rate as functions of time. An experimental chamber has been constructed of Pyrex with room temperature walls. We have used a capacitive discharge system to vaporize lead wires. We have constructed a

rotating disk deposition system using an old x-ray tube to measure the condensation rate as a function of time. We built a system that uses both transmission and Rayleigh scattering to measure the vapor density at a given point as a function of time.

We have used the improved IONMIX and CONRAD codes to consider the behavior of fill gases in three LMF target chamber designs. When a bare target of 1000 MJ explodes in a large chamber with a low density fill gas, more than 2 kg of graphite is vaporized from the walls. The debris ions are all stopped in this vapor and the resulting heating drives the vapor towards the center of the target chamber. The one-dimensional nature of CONRAD prevents accurate simulation past the point in time when the vapor is compressed in the target chamber center. We have studied the case when a lucite shell is positioned around the target for the same target chamber as in the previous case. We have concentrated on the behavior of the shell and have not yet considered wall vaporization for this design. We have found that the ion deposition raises the temperature of the inside edge of the shell to about 40 keV and vaporizes material there. This drives a shock through the shell that eventually spalls material off of the back of the shell. The final design we have considered is a bare target in a 1 torr argon fill gas. Here the gas absorbs most of the x-rays and all of the ions, but gas gets hot enough to radiate strongly to the first wall. This radiation vaporizes more than 800 g of graphite from the wall and the resulting vapor moves into the target chamber and collides with the target generated outward moving shock. In this way, the vapor shields the first wall from the target generated blast wave. It is not possible for us to state that any one of these designs is better than the others, but we can say that there are many trade-offs, and that complicated phenomena occur in all cases.

In the next phase of our work with LLNL we plan to continue the efforts presented in this report. We will operate the LMCE to provide a data base to compare against the condensation modelling in CONRAD and will make improvements to the code to enhance agreement with the experiments. We will continue to use CONRAD and IONMIX to study LMF concepts. We plan to modify the LMCE to allow heated chamber walls.

ACKNOWLEDGEMENT

Support for this work has been provided by Lawrence Livermore National Laboratory. Computing support has been provided by the National Science Foundation through the San Diego Supercomputer Center.